3D Space-Time Digital Filtering for Radio Astronomy

by

Najith Liyanage
BSc.Eng.(Hons), University of Moratuwa, Sri Lanka, 2005

A Thesis Submitted in Partial Fulfillment
of the Requirements for the Degree of

MASTER OF APPLIED SCIENCE

in the Department of Electrical and Computer Engineering

Supervisory Committee

3D Space-Time Digital Filtering for Radio Astronomy

by

Najith Liyanage
BSc.Eng.(Hons), University of Moratuwa, Sri Lanka, 2005

Supervisory Committee

Dr. Panajotis Agathoklis, Department of Electrical and Computer Engineering
Co-Supervisor

Dr. Leonard Bruton, Department of Electrical and Computer Engineering
Co-Supervisor

Dr. Kris Caputa, NRC Herzberg Institute of Astrophysics, Canada
Additional Member

Abstract

Supervisory Committee

Dr. Panajotis Agathoklis, Department of Electrical and Computer Engineering
Co-Supervisor

Dr. Leonard Bruton, Department of Electrical and Computer Engineering
Co-Supervisor

Dr. Kris Caputa, NRC Herzberg Institute of Astrophysics, Canada
Additional Member

The development of large dense arrays of smaller antennas and moderate-sized antennas equipped with multi-beam arrays in the next generation of radio telescopes, such as the square kilometre array (SKA), is making 3D space-time (ST) filtering increasingly relevant for applications in radio astronomy. The next generation of radio telescopes, such as the SKA, are expected to achieve unprecedented levels of sensitivity, resolution, survey speed and field of view (FOV). In this regard, the mitigation of radio frequency interference (RFI) and the suppression of mutually coupled (MC) signals on dense antenna arrays are being identified as most challenging. The main contribution of the work presented in this thesis is the proposal of a 3D ST filtering approach to enhance signals of interest (SOIs) by attenuating over-the-horizon RFIs and MC signals that exist on dense phased arrays. For this purpose, a novel 3D linear phase filter bank structure consisting of 1D FIR filters and 2D circularly symmetric FIR filters is proposed. The advantage of the proposed ST filtering approach is its inherent capability of broadband (BB) processing. The proposed 3D ST filtering approach is investigated on synthesised BB SOI, BB RFI and BB MC signals on dense aperture arrays (AAs) and focal plane arrays (FPAs). The results indicate successful mitigation of over-the-horizon BB RFIs and moderate suppression of BB MC signals, without significantly distorting the BB SOIs.

Table of Contents

List of Tables

List of Figures

List of Acronyms

1D	One-dimensional
2D	Two-dimensional
3D	Three-dimensional
AA	Aperture Array
ALMA	Atacama Large Millimetre Array
ASKAP	Australian Square Kilometre Array Pathfinder
ASTRON	Netherlands Institute for Radio Astronomy
BB	Broadband
BIBO	Bounded Input Bounded Output
CART	Composite Applications for Radio Telescopes
CSIRO	Commonwealth Scientific and Industrial Research Organization
DOA	Direction of Arrival
DRAO	Dominion Radio Astrophysical Observatory
DSP	Digital Signal Processing
EMBRACE	Electronic Multi-Beam Radio Astronomy ConcEpt
eMERLIN	enhanced Multi-Element Radio Linked Interferometer Network
EVLA	Enhanced Very Large Array (VLA)
FIR	Finite Impulse Response
FOV	Field of View
FPA	Focal Plane Array
GSM	Global System for Mobile
HPC	High-Performance Computing
IIR	Infinite Impulse Response
LNA	Low Noise Amplifier
LOFAR	LOw Frequency ARray
LT	Linear Trajectory
MC	Mutually Coupled
NRAO	National Radio Astronomy Observatory
PFLOPS	Peta Floating Point Operations per Second
PHAD	PHased Array Feed Demonstrator
PW	Plane Wave
RFI	Radio Frequency Interference
ROS	Region of Support
SIR	Signal-to-Interference Ratio
SKA	Square Kilometre Array
SNR	Signal-to-Noise Ratio
SOI	Signal of Interest
ST	Space Time/Spatio-Temporal
THEA	Thousand Element Array
UC-FPFC	University of Calgary Focal Plane Field Calculator
VNA	Vector Network Analyser

Acknowledgments

I wish to thank my co-supervisors, Dr. Len Bruton and Dr. Pan Agathoklis, for their advice with my research. And I'm grateful to Dr. Agathoklis for his kind support and encouragement during my depressive times in Victoria.

I would also like to thank Dr. Bruce Veidt and Dr. Rick Smegal for providing us with the necessary test data and references, and also to Gary Hovey, Donna Morgan and all other members of DRAO Canada for their support. I also wish to thank Arjuna Madanayake, Thushara Gunaratne and other members of MDSP Group, University of Calgary; Thushara, in particular, for providing us the necessary simulation data from UC FPFC.

Special thanks also to my colleagues Haytham Elmiligi and Sorrentino Diego for being very supportive throughout my stay at UVic, as well as to Lynne Palmer.

Finally, I wish to thank my family members and my wife, Imashi Opatha, for being very encouraging throughout my course of study: without them, I could not have regained the healthy perspective that allowed me to complete my studies at UVic.

Dedication:

to my wife, Imashi…

Chapter 1

Introduction

Three-dimensional (3D) space-time (ST) filters are applicable in many fields, such as wireless communications, video processing, radar, sonar, seismic signal processing [1] [2], etc. In such applications, the signals subjected to 3D ST filtering can be represented by three dimensions which include two spatial dimensions and one temporal dimension. For example in wireless communications, a two-dimensional (2D) antenna array placed at the origin in 3D space $(x, y, z) \in \mathrm{R}^3$ may receive a broadband (BB) signal over time $t \in \mathrm{R}$ which arrives from a distant source in the form of a ST plane wave (PW), resulting a 3D spatio-temporal $(x, y, t) \in \mathrm{R}^3$ signal at the array output; and in video processing an object in the spatial screen $(x, y) \in \mathrm{R}^2$ may move in a linear trajectory (LT) over time $t \in \mathrm{R}$ where it can also be represented as a spatio-temporal $(x, y, t) \in \mathrm{R}^3$ signal. Previous studies [3][4][5][6] [7][8] have shown that 3D ST filters are often preferred for applications in the above mentioned fields. They may enhance 3D ST PWs based on their direction of arrivals (DOAs) or 3D LT signals based on their trajectories and/or suppress undesirable signals such as noise, interference, multipath signals etc. Due to the recent developments in the field of radio astronomy a special interest is also emerging for employing 3D ST filtering on radio astronomical signals. The use of large dense arrays of smaller antennas, and moderate-sized antennas equipped with multi-beam arrays in radio telescopes are making 3D ST filtering increasingly relevant for applications in radio astronomy.

The major goal of the next generation radio astronomy is the extraction of information from the first stars/galaxies that formed after the Big Bang which have evolved from their first formation to the present state. This requires radio telescopes with unprecedented levels of sensitivity, resolution, and field of view (FOV) than is achieved with the current telescopes. The present generation of telescopes have reached limitations in this aspect [9][10]; therefore the radio astronomers and scientist focus on next generation telescope designs, such as the square kilometre array (SKA)[11]. The SKA is to be initiated by 2011 and the projected cost will be three billion Euros. In achieving the

science specifications of the SKA, two emerging applications of dense phased arrays (as in Fig.1-1) are being investigated to form the focal plane arrays (FPAs) of paraboloidal dishes and as rectangular aperture arrays (AAs) [10][11].

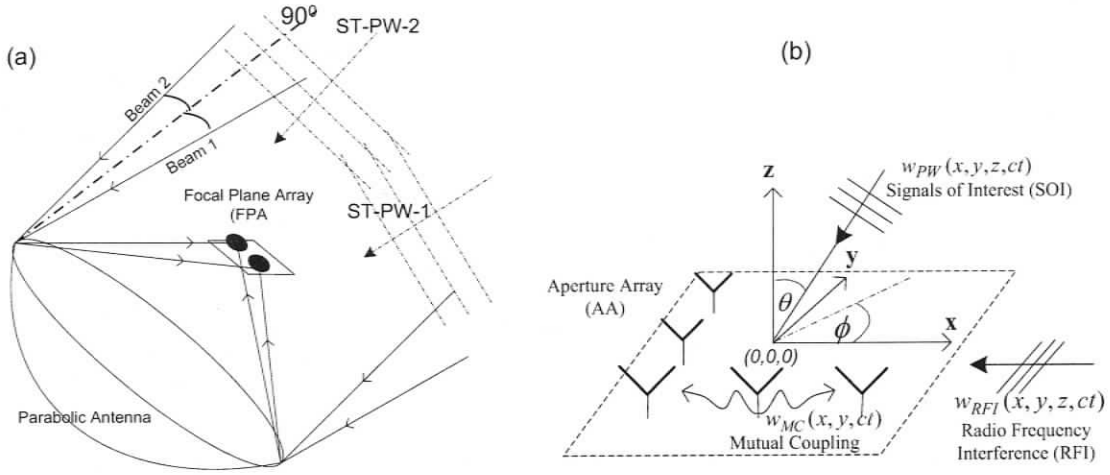

Figure 1-1. (a) A Focal Plane Array (FPA) configured on a parabolic reflector (b) an illustration of signal-of-interest (SOI), radio-frequency-interference (RFI) and mutual coupling on an Aperture Array (AA)

The signals-of-interest (SOIs) in the next generation radio telescopes, such as the SKA, may span many decades of temporal-frequency (broadband-BB). The requirement of unprecedented levels of sensitivity makes radio frequency interference (RFI) a major problem for the next generation of radio astronomy. Further, as illustrated in Fig.1-1(b), the close spacing of the antennas in the dense FPAs/AAs leads to undesirable electromagnetic mutual coupling between antennas. Previously reported work on the mitigation of RFI is based on temporal blanking techniques which are mostly suitable for intermittent RFI [12], on spatial filtering techniques which use subspace-projection methods [13][14] [15], on cancellation techniques which use a reference signal approach [16], and on post-correlation cancellation and anti-coincidence techniques [17]. They are mostly being investigated in the context of narrowband applications. Therefore, for broadband applications sub-band processing mechanisms comprised of such narrowband techniques are suggested. A universal technique that addresses broadband (BB) RFI mitigation in radio astronomical applications has not yet been reported. Previously

reported methods for the suppression of mutually coupled (MC) signals are mostly based on principles of radiation pattern multiplication [18], on active element reflection coefficient and scattering parameter analysis [19], on sensitivity analysis of large phased arrays using method-of-moments simulations [20], and on the network theory framework [21]. They are also mostly suitable for narrowband applications. For these reasons, the next generation radio of telescopes seek a suitable BB approach which is capable of suppressing of BB RFI and BB MC signals without significantly distorting SOIs.

1.1 Contributions of the Thesis

The main contribution of the work presented in this thesis is the proposal of a 3D ST filtering approach to enhance BB SOIs by attenuating over-the-horizon BB RFI and BB MC signals on dense phased arrays. For this purpose, a novel 3D linear phase filter bank structure consisting of 1D FIR filters and 2D circularly symmetric FIR filters is proposed. The phased arrays may include FPAs and AAs that are emerging for next generation radio astronomical applications. The main advantage of the proposed ST filtering approach is its inherent capability of BB processing.

The BB RFI signals $w_{RFI}(x, y, ct)$, such as over-the-horizon signals, are modeled using BB ST-PW signals that propagate at, or close to, light speed c with 3D spatial DOAs that are on (or sufficiently close to) the plane of the phased array. Such ST-PW signals have 3D space-time line spectra in $(\omega_x, \omega_y, \omega_{ct}) \in \mathrm{R}^3$ having ROSs that are on, or close, to the surface of the 3D spectral light cone $(\omega_x^2 + \omega_y^2 = \omega_{ct}^2)$ [2]. The BB MC signals $w_{MC}(x, y, ct)$ are modeled using an exponentially decaying circularly-symmetric propagating signal function. It is shown that the spectrum of such a wave has support around the spectral light cone, with smearing in spatial frequencies caused by the spatial attenuation along the array. The synthesised BB ST models indicate that both BB RFI and BB MC signals can be attenuated by a suitable 3D ST cone filter encompassing ROS of the BB SOI in its passband, and the spectral light cone in its stopband.

The subsequent beamforming/correlation operations demand that the ST filtering preserve the phase information of the SOI. Further, it requires that SOIs undergo minimal distortion by the cone filter while providing maximum immunity to RFI and MC signals.

Thus, the 3D cone filter must have a linear phase transfer function and a circular cross section to enclose the ROSs of the SOIs in FPAs/AAs. Previously reported analytic cone filters [4][5] [7][22] fall short in these aspects. Therefore, a novel analytic 3D linear phase filter bank structure consisting of 1-D FIR filters and 2-D circularly symmetric FIR filters is proposed.

1.2 Organisation of the Thesis

This thesis comprises of seven chapters followed by the bibliography and an Appendix. It investigates the applicability of 3D ST filtering on the signals of next generation radio telescopes. Chapter-2 sets forth the related background on technological advancement of radio telescopes. The motivation behind a broadband technique for suppression of BB RFI and BB MC signals, and its impact on the next generation radio telescope designs are brought in to consideration.

In Chapter-3, the BB RFI and BB SOI incident on dense AAs and FPAs are discussed. In order to model BB SOI on FPAs, the functional form of the field distribution on the FPA is reviewed. The ROSs of BB RFIs and BB SOIs are illustrated using synthesised BB ST signals and their ROSs of the spectra in the 3D frequency domain are analysed.

In Chapter-4 a novel ST propagation model is proposed and investigated to represent mutual coupling that exists on dense BB antenna arrays. The scattering parameter data measured from a Vivaldi antenna array is examined to investigate the validity of the theoretical model. A theoretical study of the spectral characteristics of BB MC signals is presented followed by a numerical simulation analysis, in 3D space-time and spatio-temporal frequency domains. In this analysis, two possible MC signals namely, photonically reflected incident waves and internally generated LNA noise waves are considered.

In Chapter-5, a novel ST digital filter is proposed to approximate the required cone shaped passband to filter ST BB signals discussed in Chapter-3 and 4. Two previously reported analytic FIR and IIR 3D ST cone filters are analysed and simulated to investigate their properties. The proposed filter is employed on synthetic BB ST signals

to demonstrate its superior performance in comparison to the other two analytic FIR and IIR techniques.

In Chapter-6, the proposed cone filter bank is used on synthesised BB RFI, BB SOI and BB MC signals to investigate the proposed ST filtering approach. First, the mitigation of BB RFI and the suppression of BB MC signals are numerically analysed by employing the proposed ST cone filter bank. Then, the proposed cone filter bank is employed on simulated (synthesised) composite signals received by AAs and FPAs to investigate its performance.

Finally, Chapter-7 discusses the important conclusions of the work presented in the preceding chapters and provides several suggestions for future work.

Chapter 2

Background

This Chapter sets forth the related background on the technological advancement of radio telescopes. First, the next generation of radio telescopes such as the largest ever radio telescope design in progress, the Square Kilometre Array (SKA), is discussed. Next, the novel use of phased arrays as aperture arrays (AAs) and focal plane arrays (FPAs) for the next generation radio telescopes is discussed. Lastly, the motivation behind a broadband technique for suppressing radio frequency interference (RFI) and mutually coupled (MC) signals, and its impact on the next generation radio telescope designs are brought in to consideration.

2.1 The Next Generation of Radio Astronomy

During the past few decades radio astronomers have made enormous efforts to investigate cosmic background radiation which contains information about the early state of the Universe. The retrieval of such information is considered a pathway to understanding the *Big Bang*, the origin of the Universe. In the course of such investigations, radio astronomers have shown interest in observing millimetre (very short) radio wavelengths, and longer wavelengths emanating from extremely distant galaxies, which are red-shifted versions of infrared, sub-millimetre and/or millimetre waves. The ALMA (Atacama Large Millimetre Array), a giant millimetre-wave array with 66 dishes on the Atacama plateau in Chile, the EVLA (Enhanced VLA-Very Large Array) in the USA and eMERLIN (enhanced MERLIN) in the UK are some examples of emerging developments in the present generation of radio telescopes [10].

As a further step forward scientists are working towards developing a telescope that can achieve several orders of magnitude increase in sensitivity over existing facilities at metre to millimetre wavelengths. In this respect, technological factors such as receiver designs (including dishes, feeds and aperture arrays), signal transport, signal processing, software engineering and algorithm development, high performance computing as well as

data storage and power requirements are considered to be critical. As a consequence of extensive discussions among the science drivers and evolving technical advancements in the areas of receiver design, array synthesis, high-performance computing (HPC) and programmable digital signal processing (DSP), a next generation large radio telescope concept called the Square Kilometre Array (SKA) is being introduced [10] [11].

2.1.1 The Square Kilometre Array (SKA)

The SKA is an interferometric array of individual antennas and groups of antennas (stations) synthesizing an aperture of one million square metres with a diameter of up to several thousand kilometres [11]. A site for the SKA will be chosen by 2011-12, and the construction of phase one is scheduled for 2013-2020 [11]. An artist's impression of the proposed array structure for the SKA is shown in Fig.2-1. The total cost of the telescope is expected to be about three billion Euros shared among the seventeen partnership countries including Canada.

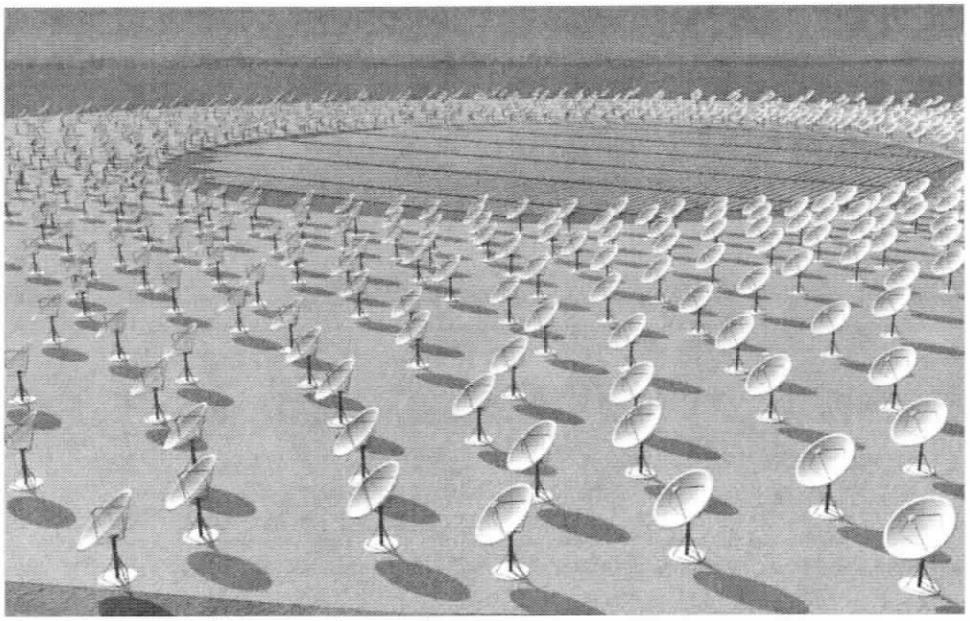

Figure 2-1. An artist's impression of the proposed array structure for the Square Kilometre Array (The SKA Brochure, [11])

The key science drivers of the SKA are categorised as investigation of origins (the cosmology/galaxy evolution, probing the dark ages and cradle of life); study of fundamental forces (strong-field tests of general relativity and origin and evolution of

cosmic magnetism); and exploration of unknowns. Such groundbreaking science drivers, would require the proposed radio telescope to encompass unprecedented characteristics in comparison to the present generation of radio telescopes. To detect and image hydrogen in the early universe the collecting area of the SKA is required to be one square kilometre. As a result, it may achieve sensitivity at least fifty times higher than that of ELVA or LOFAR (LOw Frequency ARray) [10]. A very large field of view (FOV) is required to attain a fast survey speed over the whole sky, which will be one million times faster than ELVA. The signals of interest (SOIs) may span decades of radio frequencies; therefore, an operational bandwidth of at least 100 MHz - 25 GHz is expected. In addition, the array will have a large physical extent up to 3000+ kilometres in order to achieve the capability of detailed imaging of compact objects, and astrometry with thousandth arc second angular resolution. A brief summary of the SKA science requirements is shown in Table 2-1.

Table 2-1. SKA Science Requirements ([11], memo-100)

Configuration	20% collecting area < 1 km diameter, 50% of collecting area < 5 km diameter, 75% of collecting area < 150 km diameter
Frequency range	100 MHz - 25 GHz Goal: 60 MHz - 35 GHz
Sensitivity at 45 degrees elevation (A/T)	5000 at 200 MHz, 20000 between 0.5 and 5 GHz, 15000 at 15 GHz, and 10000 at 25 GHz
Contiguous imaging field of view (FoV)	1 sq. degree within half power points at 1.4 GHz, scaling as $\lambda 2$, 200 sq. deg. within half power points at 0.7 GHz, scaling as $\lambda 2$ between 0.5-1.0 GHz
Number of separated fields of view	1 with full sensitivity Goal: 4 with full sensitivity 10 simultaneous sub-arrays
Beamformer capability	50 simultaneous summed (phased array) beams within FoV, inner 5 km diameter of array. No time averaging, 8 bits/sample
Survey speed	$FoV \times (A/T)^2 \times BW = 3 \times 10^{17}$ deg^2 m^4 K^{-2} Hz^{-1} at 1.5 GHz $FoV \times (A/T)^2 \times BW = 1.5 \times 10^{19}$ deg^2 m^4 K^{-2} Hz^{-1} at 0.7 GHz

The design of the individual antennas/stations for the SKA has not yet been finalised. Proposals have ranged from dishes with single-pixel feeds, dishes with multi-pixel

phased array feeds such as Focal Plane Arrays (FPAs) and Aperture Arrays (AAs) [9]. The technical capability of such a single instrument is inadequate to meet all SKA science requirements, and so hybrid concepts are being investigated [10].

The novel use of phased arrays such as FPAs and AAs are potential configurations for next generation radio telescope designs, such as the SKA. Therefore, the work presented in this thesis is based on AA/FPA applications of next generation radio astronomy.

2.2 Focal Plane Arrays (FPAs) and Aperture Arrays (AAs)

A Focal Plane Array (FPA) is a dense phased array that acts as a feed in the focal plane of a reflector antenna as shown in Fig.2-2. A digital beamformer is combined with the outputs of the FPA for beamsteering over a continuous region of the sky. Such a configuration has the potential to provide several benefits over single feed reflectors, such as increased FOV, increased survey speed, interference cancellation and increased sensitivity. Further, the use of phased arrays is preferred over horn-clusters for several reasons ([11], memo-71) such as the capability of fully sampling the focal plane of a reflector and allowing flexibility to designers to use noisier receivers. At present, four research teams are working on the FPA development. They are the National Radio Astronomy Observatory (NRAO) in collaboration with Brigham Young University which has built a 19-element array of sinuous antennas as an early demonstration of an FPA [23]; the Australian Commonwealth Scientific and Industrial Research Organization (CSIRO) which is developing an FPA for use in the Australian Square Kilometre Array Pathfinder (ASKAP) [24][25]; the Netherlands Institute for Radio Astronomy (ASTRON) which has made promising progress on a wideband, dual polarized array of Vivaldi antennas called 'DIGESTIF' [26]; and the Canadian National Research Council which has also developed an 84-element Vivaldi array called the PHased Array Feed Demonstrator (PHAD) at Dominion Radio Astrophysical Observatory (DRAO) [27][28]. The classical beamforming method is being used for beamforming of the PHAD at DRAO (Appendix A).

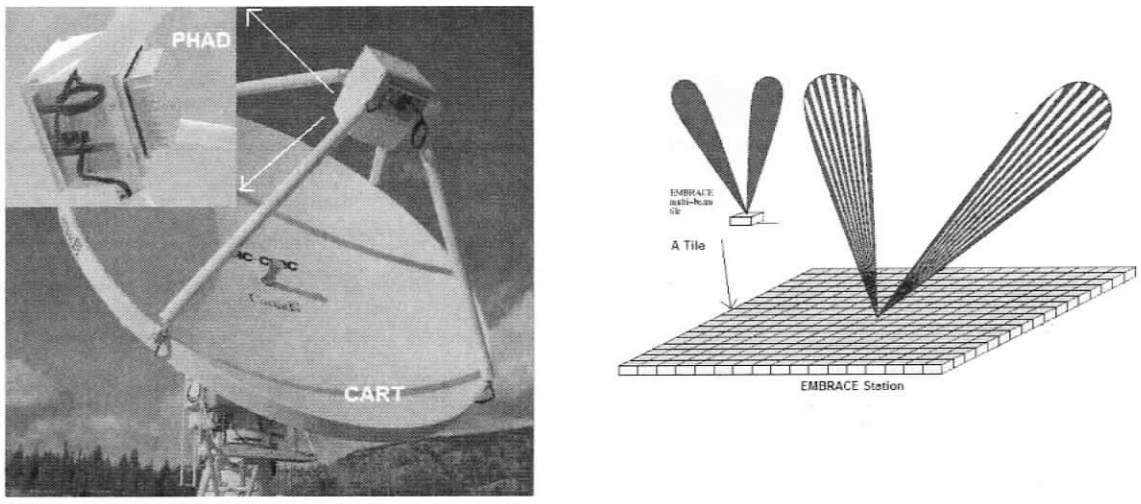

(a) (b)

Figure 2-2. Examples of FPA and AA configurations (a) FPA:- PHAD on 10m Composite Applications for Radio Telescopes (CART) at DRAO [27] (b) AA:- EMBRACE of Astron showing the formation of independent multiple FOVs at both the tile and station level [29]

Another innovative concept of next generation radio telescopes that emerged with the SKA telescope design is the use of flat phased arrays called Aperture Arrays (AAs). In the SKA design, two types of AA array configurations are proposed: the sparse AA and the dense AA [11]. This thesis focuses only on dense AA configurations containing elements spaced satisfying the spatial Nyquist condition (see section 3.4.1). Therefore, in what follows, the term AA, unless otherwise defined refers to dense AAs. By employing a digital beamformer, the AAs are capable of increasing the FOV and the survey speed while providing immunity to radio frequency interference [10]. The AA technology is prototyped by ASTRON, Netherlands in the THEA (Thousand Element Array) project, which consists of tiles of 64 element broadband phased arrays. The project had promising results [30] which lead to a more ambitious demonstrator called EMBRACE-`Electronic Multi-Beam Radio Astronomy ConcEpt' with an area of about 300 square metres with multiple large independent FOV capabilities [10][29].

The majority of the signal processing in the next generation telescopes will be in digital form. For a synthesis telescope on the scale of the SKA, a cost-effective approach is to perform cross-correlation of FPA/AA stations involves the 'FX' architecture where the frequency transformation 'F' (usually done with FFT) precedes the cross multiply operations 'X' [31][10]. This architecture also efficiently supports the digital

beamforming operations performed at station/element level of FPAs/AAs. An overview of the classical beamforming method is given in Appendix-A. Both digital beamforming and the correlation processes are highly sensitive to the phase information. Therefore it is mandatory that any pre-processing techniques introduced at FPA/AA level preserve the phase information of observation data. This requirement will be considered in Chapter-5.

2.3 Motivation

The primary advantages of the use of FPAs/AAs in next generation radio telescopes are their capability of achieving higher FOV, sky resolution and survey speed, while sustaining greater immunity to RFI. Such immunity is difficult to maintain if the FPAs/AAs are expected to achieve their maximum possible sensitivity, since at higher sensitivity they become more vulnerable to RFI. The radio-quiet zones are proposed [32] [33] for radio observatories, but avoiding RFIs including the noise emanating from surrounding terrain is practically impossible. Furthermore, recent studies have shown that mutually coupled (MC) signals will also decrease system sensitivity since noise generated from one LNA is propagated towards the surrounding LNAs, increasing overall noise temperature [19]. The correlated nature of MC LNA noise makes it impossible to suppress at the correlation process. Mutual coupling of photonically reflected incident waves [34] may have minor effects on radio astronomical observations compared to LNA noise coupling, but may lead to beam deformations at digital beamforming.

The above mentioned signals may lead to considerable reduction of the overall system sensitivity of next generation telescopes, such as the SKA. For this reason, the recent research studies on the development of FPAs/AAs are focused towards finding suitable techniques to suppress RFI and MC signals.

2.3.1 The Effect of Broadband (BB) Radio Frequency Interference (RFI) and BB Mutual Coupled (MC) Signals on System Sensitivity

System sensitivity is a generic system performance metric used for FPA/AA applications in radio astronomy, which is defined by,

$$S_{sys} = \frac{A_e}{T_{sys}} \tag{2.1}$$

where A_e is the effective area of the array and T_{sys} is the equivalent system temperature. The SOIs in radio astronomy are low in power and are detected as small changes in the output noise power baseline; therefore, they are measured in the scale of micro-Janskys where Jansky is $10^{-26} W/(m^2 Hz)$. For this reason, powers of external and internal disturbances ($P_{disturbance}$) are discussed using an equivalent temperature analogous to a noise power of a resistor being transferred to a matched load, given by,

$$T_{disturbance} = \frac{P_{disturbance}}{k_b B_n} \tag{2.2}$$

where $k_b = 1.308 \times 10^{-23} J/K$ is the Boltzman's constant, B_n is the equivalent bandwidth of noise and $T_{disturbance}$ is temperature in Kelvin. Dominant sources of such disturbances in radio-astronomical applications can be categorised as [9]; sky noise (T_{sky}) due to the cosmic microwave background, noise from our galaxy, and atmospheric loss, external interferences (T_{RFI}) due to externally originated RFI/ground scattering arriving in the spill-over angle, receiver noise (T_{rec}) which contain additive LNA noise and thermal noise caused by the ohmic resistance of the antennas/propagation path, and mutual coupling (T_{MC}) of LNA noise and photonically reflected incident waves. The combination of all these noise sources is represented by an equivalent system temperature (T_{sys}) over a load at the output of the receiver system as,

$$T_{sys} = T_{sky} + T_{RFI} + T_{rec} + T_{MC} \tag{2.3}$$

An example of a typical noise budget from BYU/NRAO L-Band Phased Array Feed is illustrated in Table 2-2.

Table 2-2. An example of a noise budget (source: BYU/NRAO L-Band Phased Array Feed [25])

	Measured (K)	Modeled (K)
T_{sky}	3	3
T_{RFI}	5	5
T_{rec}	38	38
T_{MC}	20	23
T_{sys}	66	69

The measured temperatures show good correspondence to modeled temperatures. Based on the measured/modeled temperature composition, it can be assumed that the BB RFI and BB MC signal contribution to the overall system temperature is approximately 35%. This is significant for telescopes on the scale of the SKA.

2.3.2 *The SNR and the System Sensitivity*

The Signal-to-Noise Ratio (SNR) is a widely used metric to investigate the performance of a signal processing application. It represents how well a certain signal processing technique manage to enhance SOIs by attenuating noise (where 35% of noise power includes RFIs and MC signals). For a radio astronomical receiver system the SNR can be represented as[35],

$$SNR = \frac{P_{SOI}}{P_{interference}} = \frac{A_e S^{SOI}}{k_b T_{sys} B_n} \tag{2.4}$$

where $A_e(m^2)$ is the effective area of the antenna aperture and $S^{SOI}(W/m^2)$ is the SOI flux density. The ratio A_e/T_{sys} is the sensitivity of a radio astronomical receiver system, and the relationship between SNR and sensitivity can be re-written as,

$$S_{sys} = \frac{A_e}{T_{sys}} = \frac{k_b B_n}{S^{SOI}} SNR \tag{2.5}$$

Therefore it is clear that the SNR(being inversely proportional to system temperature T_{sys}) is proportional to sensitivity S_{sys}.

2.3.3 *The Impact of BB RFI Mitigation and BB MC Signals Suppression on Designing the Next Generation of Radio Telescopes*

The mitigation of BB RFI and the suppression of BB MC signals improve the SNR. According to (2.5), given that the SOIs are not distorted significantly, the SNR improvement will reflect on to an improvement in the sensitivity, and therefore will impact on the telescope design. To observe this, assume that a suitable BB technique is employed for the mitigation of RFI and the suppression of MC signals at each dish with an FPA, in the SKA telescope. Based on (2.5), an improvement of SNR by 0.5dB will equivalently increase the system sensitivity by 12.2%. This will result in a saving of approximately 360 dishes if the initial design of the SKA telescope is to install 3000 dishes. Given that the cost of the employed broadband technique is comparatively smaller

than the cost of a dish, the cost effectiveness can be considerably improved. A similar advantage can also be achieved with AAs as well.

Further, the suppression of BB RFI and BB MC signals may also contribute to a reasonable reduction in the data processing overhead of the SKA designs. High-performance computing technologies (HPC) and/or programmable DSP engines are expected to be used for the post-processing of observation data collected by the massive SKA telescope. The data transmission is therefore expected to be in the range of TBytes/s whereas the data storage is expected to be in the order of thousands of TBytes. For such an enormous data capacity, the corresponding data processing rates will also be in a similar magnitude. The correlation and signal processing operations may require a working rate of order 10^{18} floating point operations per second (approx. 200PFLOPS), whereas the incorporated radio-imaging techniques may require as high as 10^{15} floating point operations per second (approx. 20PFLOPS) [11]. Therefore, employing a suitable pre-processing technique on the mitigation of RFI and the suppression of mutual coupling at each FPA/AA may considerably reduce complex post-processing required to remove needless information. This should lead to a considerable increase in processing efficiency and cost-effectiveness of a telescope in the scale of the SKA.

Chapter 3

Broadband (BB) Radio Frequency Interference (RFI) and Signal of Interest (SOI)

In this chapter the broadband (BB) radio frequency interference (RFI) and signal of interest (SOI) on dense aperture arrays (AA) and focal plane arrays (FPAs) are reviewed and discussed. In the first part, the RFI on AAs/FPAs and SOI on AAs are modeled as ST PWs followed by an analysis in the 3D spatio-temporal frequency domain. The ROSs of such signals are illustrated using synthesised BB ST-PWs. In the second part, the functional form of the field distribution on FPAs is reviewed in order to approximate the ROS of BB SOI on FPAs in the 3D frequency domain.

3.1 Introduction

The next generation of radio telescopes, such as Square Kilometre Array (SKA), are intended to be at least two orders of magnitude more sensitive than the current generation of telescopes. Such demanding requirements as increased sensitivity and increased bandwidth make next generation telescopes more vulnerable to radio frequency interference (RFI), even if the proposed locations are expected to be highly radio-quiet zones [32][33]. This motivates the development of receiver systems such as dense Aperture Arrays (AAs) and Focal Plane Arrays (FPAs) that incorporate RFI mitigation techniques to maintain the integrity of signals of interest (SOI) in the presence of RFI. In this chapter, a ST modeling of broadband (BB) RFI and BB SOI incident on AAs and FPAs is discussed in order to investigate their ROS of the spectrum in 3D spatio-temporal frequency domain.

3.2 Modelling of ST BB RFI

Terrestrial over-the-horizon man made RFIs such as signals from TV transmitters, FM transmitters, GSM downlinks, beacons and mobile communication etc., and other far-field noise signals are often scattered by intervening terrain, and arrive at the antenna array over a significant angular range. Such type of RFIs can be modeled as BB ST-PWs

arriving at the antenna array from a direction of arrival (DOA) that does not fall in to the DOAs of SOIs. An ideal 4D continuous domain BB ST RFI can be modeled in the form of a 4D ST-PW [2] as illustrated in Fig.3-1,

$$w_{C\_RFI\_4D}(x,y,z,ct) = w_{PW}(d_x x + d_y y + d_z z + ct) \tag{3.1}$$

where $\mathbf{d} = (d_x, d_y, d_z)$ is the unit vector defining the DOA in 3D space $(x,y,z) \in \mathbf{R}^3$, c is the constant group velocity and $w_{PW}(l)/\forall l = d_x x + d_y y + d_z z + ct$ is the 1D intensity function propagating along the DOA, and $t \in \mathbf{R}^1$ is time. The polarization of the signal is not considered here, and the following analysis is for non-polarised waves.

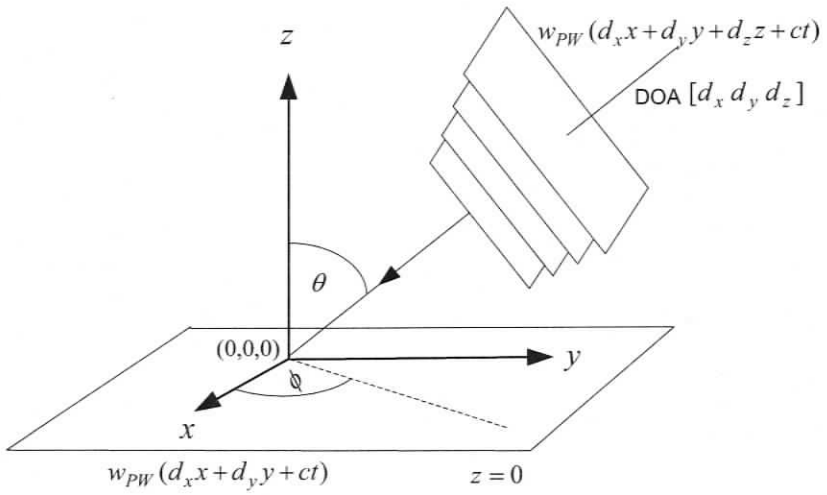

Figure 3-1. A 4D spatio-temporal plane wave $w_{PW}(d_x x + d_y y + d_z z + ct)$ represented in 3D space $(x,y,z) \in \mathbf{R}^3$ over time $t \in \mathbf{R}$, being received by a 2D infinite extent sensor array at $z = 0$, resulting $w_{PW}(d_x x + d_y y + ct)$

By defining the DOA vector in polar coordinates such that,

$$[d_x, d_y, d_z] \equiv [\sin\theta_{PW}\cos\phi_{PW}, \sin\theta_{PW}\sin\phi_{PW}, \cos\theta_{PW}] \tag{3.2}$$

where (θ_{PW}, ϕ_{PW}) are the elevation and azimuth angles respectively, a given ST-PW of spatial DOA of (θ_{PW}, ϕ_{PW}) is required to satisfy the condition,

$$90^0 \geq \theta_{PW} > \max\{\theta_{AA/FPA\_SOI}\}, \forall \phi_{PW} \tag{3.3}$$

in order to be considered as RFI. The $\max\{\theta_{AA/FPA\_SOI}\}$ is the maximum azimuth angle corresponding to the span of possible SOIs received by AAs/FPAs.

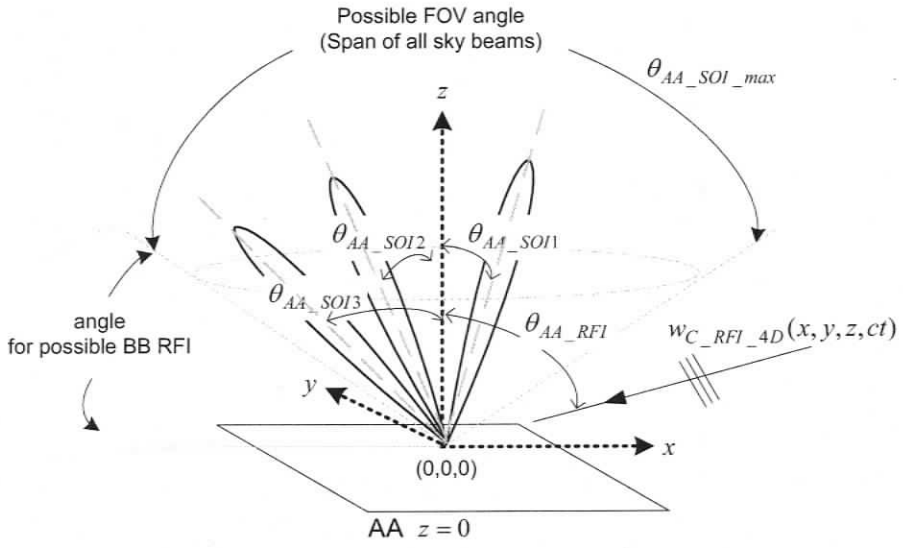

Figure 3-2. ST PWs as SOI and RFI signals on Aperture Arrays (AAs) distinguished by their spatial Direction of Arrival (DOA) in $(x, y, z) \in \mathbf{R}^3$

Figs 3-2 and 3-3, illustrate possible DOAs of RFI in 3D-space $(x, y, z) \in \mathbf{R}^3$ for AAs and FPAs respectively. For AAs, it is clear that RFI may arrive at an angle between the horizon ($z = 0$) and an angle,

$$\theta_{AA\_SOI\_\max} = \max\{\theta_{AA\_SOI}\} \tag{3.4}$$

where $\max\{\theta_{SOI\_AA}\}$ is the maximum SOI angle pre-defined in the beamforming operations of the array corresponding to all expected sky beams, as illustrated in Fig. 3-2. In the case of FPAs, the angle subjected to possible RFI intrusion may correspond to an angle between the focal plane and the physical spill over angle, θ_{spill} as illustrated in Fig.3-3. The spill over angle θ_{spill} is the angle from the center of the FPA subtended to the outer rim of the paraboloidal dish. Due to the diffraction of SOI in the outer-rim of the paraboloidal dish caused by non-zero taper at the edge of the outer-rim and the considerable size of the FPA, $\max\{\theta_{FPA\_SOI}\}$ on the FPA could exceed θ_{spill}.

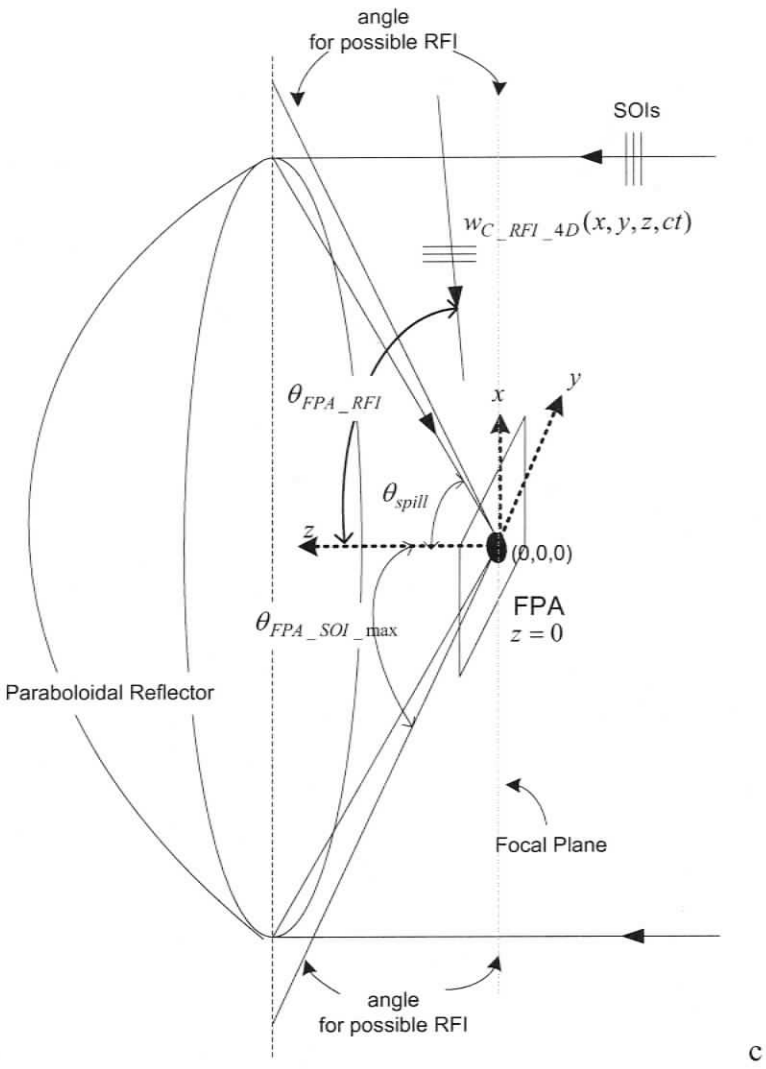

Figure 3-3. Illustration of SOI which are not approximated as PWs and RFI signals as ST PWs incident on Focal Plane Arrays (FPAs)

The derivation of $\max\{\theta_{FPA\_SOI}\}$ in the case of FPAs is further discussed in section 3.6. For simplicity, let us define,

$$\theta_{FPA\_SOI\_\max} = \max\{\theta_{FPA\_SOI}\} \text{ where } \max\{\theta_{FPA\_SOI}\} > \theta_{spill} \tag{3.5}$$

Therefore, the corresponding RFI being modeled as an arbitrary BB ST PW arriving on AAs and FPAs may have their respective DOAs given by,

$90^0 \geq \theta_{PW} > \theta_{AA\_SOI\_\max}, \forall \phi_{PW}$ and

$90^0 \geq \theta_{PW} > \theta_{FPA\_SOI\_\max}, \forall \phi_{PW}$ respectively. (3.6)

3.3 BB ST SOI on AAs

In the case of AAs, any BB ST-PW arriving at the array that has a DOA corresponding to a sky beam pre-defined in the subsequent beamforming operations in the array is considered to be a BB ST SOI, as illustrated in Fig.3-2. Thus any BB ST-PW with a DOA of (θ_{PW}, ϕ_{PW}) in polar coordinates satisfying the condition,

$$0^0 \le \theta_{PW} \le \theta_{AA\_SOI\_\max}, \forall \phi_{PW} \tag{3.7}$$

is considered as a BB SOI on AAs.

3.4 A Review of BB ST PWs in 3D Spatio-Temporal Frequency Domain

It is clear that BB ST RFI on FPAs/AAs and BB ST SOIs on AAs can be represented as ST-PWs distinguished by their DOAs. Therefore, the analysis of BB ST-PWs in the spatio-temporal frequency domain [2] will lead us to the spectral properties of BB ST RFI on FAPs/AAs and BB ST SOI on AAs. Consider an ideal 4D continuous domain BB ST-PW $w_{C\_4D}(x, y, z, ct)$ received by a planar 2D sensor array located at $z = 0$. Then the received signal can be represented in the 3D space-time $(x, y, t) \in \mathbf{R}^3$ domain as,

$$w_{C\_3D}(x, y, ct) \equiv w_{C\_4D}(x, y, z, ct)\big|z = 0 \tag{3.8}$$

At this point the 2D array is assumed to be of infinite extent. The corresponding continuous domain 3D spatio-temporal frequency representation of (3.8) can be obtained by the 3D Fourier transform derived as,

$$W_{C\_3D}(\Omega_x, \Omega_y, \Omega_{ct}) \equiv \int_{-\infty}^{\infty}\int_{-\infty}^{\infty}\int_{-\infty}^{-\infty} w_{C\_3D}(x, y, ct) e^{-j(x\Omega_x + y\Omega_x + ct\Omega_{ct})} dxdydct \tag{3.9}$$

For a BB ST PW with arbitrary DOA vector of, $[d_x, d_y, d_z] \equiv [\sin\theta\cos\phi, \sin\theta\sin\phi, \cos\theta]$, with an intensity function of $w_{PW}(d_x x + d_y y + d_z z + ct)$, (3.9) can be rewritten as,

$$\begin{aligned}
&W_{C_3D}(\Omega_x, \Omega_y, \Omega_{ct}) \\
&= \int_{-\infty}^{\infty}\int_{-\infty}^{\infty}\int_{-\infty}^{-\infty} w_{PW}(d_x x + d_y y + ct) e^{-j(\Omega_x x + \Omega_y y + ct\Omega_{ct})} dctdxdy \\
&= \int_{-\infty}^{\infty}\int_{-\infty}^{\infty} e^{-j(x\Omega_x + y\Omega_x - (d_x x + d_y y)\Omega_{ct})} \underbrace{\int_{-\infty}^{-\infty} w_{PW}(d_x x + d_y y + ct) e^{-j(d_x x + d_y y + ct)\Omega_{ct}} dctdxdy}_{W_{PW}(\Omega_{ct})}
\end{aligned}$$

$$= \int_{-\infty}^{\infty} e^{-j(\Omega_x - d_x\Omega_{ct})x} dx \int_{-\infty}^{\infty} e^{-j(\Omega_y - d_x\Omega_{ct})y} dy W_{PW}(\Omega_{ct})$$

$$= \delta(\Omega_x - d_x\Omega_{ct})\delta(\Omega_y - d_y\Omega_{ct})W_{PW}(\Omega_{ct}) \quad (3.10)$$

where $(\Omega_x, \Omega_y, \Omega_{ct}) \in \mathbf{R}^3, \Omega_{ct} = \Omega_t / c$ and $\Omega_t \in \mathbf{R}^1$ is the continuous domain temporal frequency of the BB ST intensity function $w_{PW}(ct)$ where its Fourier transform is $W_{PW}(\Omega_{ct})$. By closely examining $W_{C\_3D}(\Omega_x, \Omega_y, \Omega_{ct})$, it can be easily observed that the ROS of (3.10) is equivalently the ROS of the spectrum of $W_{PW}(\Omega_{ct})$ that lies on a straight line given by the intersection of two planes,

$$\delta(\Omega_x - d_x\Omega_{ct}) = 1 \Leftrightarrow \Omega_x - d_x\Omega_{ct} = 0 \text{ and}$$

$$\delta(\Omega_y - d_y\Omega_{ct}) = 1 \Leftrightarrow \Omega_y - d_y\Omega_{ct} = 0 \quad (3.11)$$

through the origin, where $d_x = \sin\theta\cos\phi$ and $d_y = \sin\theta\sin\phi$, as illustrated in Fig.3-4.

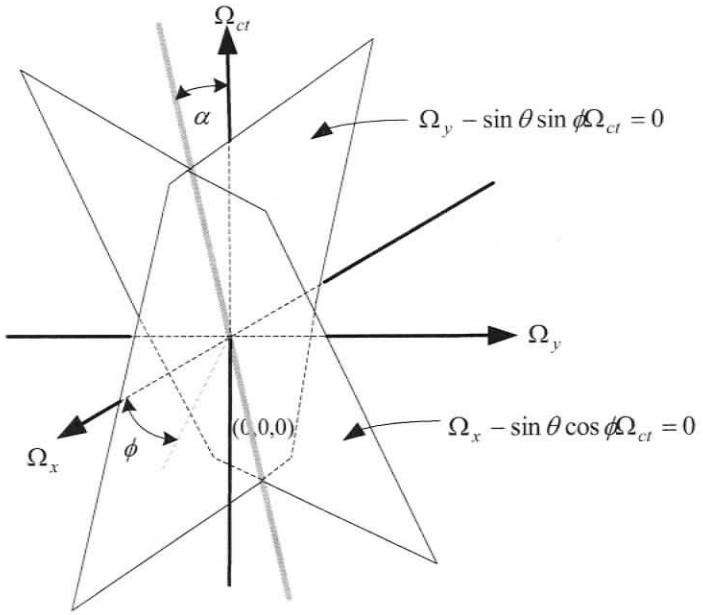

Figure 3-4. Intersection of planes as in (3.11) illustrating the ROS of a BB ST-PW as a line through the origin with an orientation given by the space-time DOA

Using (3.11) the angle α which defines the orientation of the line spectrum (the spatio-temporal DOA of the PW) in Fig.3-4, can be derived as,

$$\tan\alpha = \frac{\sqrt{\Omega_x^2 + \Omega_y^2}}{\Omega_{ct}}$$

$$= \frac{\sqrt{(\sin\theta\cos\phi\Omega_{ct})^2 + (\sin\theta\sin\phi\Omega_{ct})^2}}{\Omega_{ct}}$$

$$= \sin\theta$$

$$\alpha = \tan^{-1}(\sin\theta) \tag{3.12}$$

A BB ST-PW arriving at a planar array with a spatial DOA of (θ,ϕ), therefore, has its ROS in the 3D spatio-temporal frequency domain in a straight line through the origin with an orientation of $(\tan^{-1}(\sin\theta),\phi)$ as shown in Fig.3-5. The term $(\tan^{-1}(\sin\theta),\phi)$ is considered as the spatio-temporal DOA corresponding to the spatial DOA (θ,ϕ). For all possible BB ST-PWs with $(0 \le \theta \le 90, \forall\phi)$, the respective ROSs are confined to a cone $\Omega_x^2 + \Omega_y^2 = \Omega_{ct}^2$, $(45^0, \forall\phi)$, which is the well known spectral light cone as illustrated in Fig.3-5.

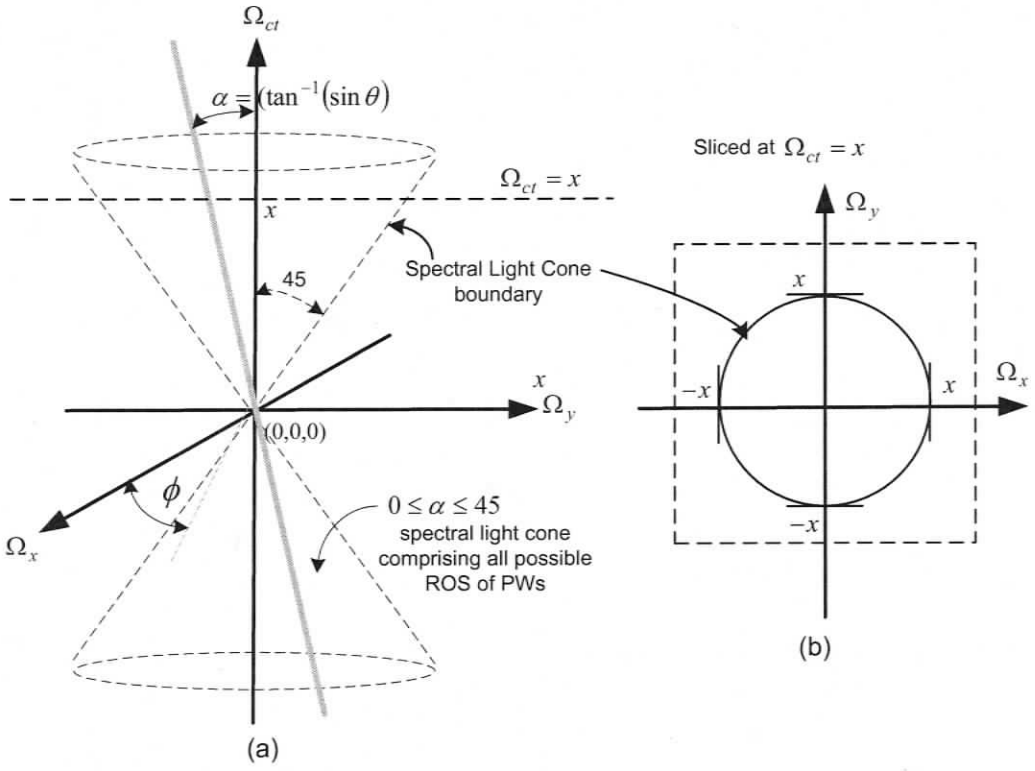

Figure 3-5. (a) All possible BB ST-PWs with $(0 \le \theta \le 90, \forall\phi)$, the respective ROSs confine to a cone $\Omega_x^2 + \Omega_y^2 = \Omega_{ct}^2$, $(45^0, \forall\phi)$ (b) a contour slice taken at $\Omega_{ct} = x$ illustrating the spectral light cone boundary in spatial frequency domain.

3.4.1 Spatial and Temporal Aliasing

If $w_{C\_3D}(x,y,ct)$, (3.8) is being received by uniformly-weighted rectangularly-sampled infinite-extent spatial antenna array at $z=0$, the resultant mixed domain signal can be expressed in the form of,

$$w_{M\_3D}(n_x,n_y,ct)=w(d_x n_x T_x+d_y n_y T_y+ct) \tag{3.13}$$

where $T_{x,y}\in\mathbf{R}^1$ are the spatial sampling intervals and $n_{x,y}\in\mathbf{Z}^1$. Assuming that the signal in (3.13) is ideally sampled in the temporal dimension with infinite extent, (3.13) can be expressed in the discrete space-time domain as,

$$w_{D\_3D}(n_x,n_y,n_{ct})=w(d_x n_x T_x+d_y n_y T_y+n_{ct}T_{ct}) \tag{3.14}$$

where $T_{ct}\in\mathbf{R}^1$ is the temporal sampling interval and $n_{ct}\in\mathbf{Z}^1$. Further, we may assume that $w_{C\_3D}(x,y,ct)$, (3.8) is a temporally band-limited signal; then, there exist f_s such that $\frac{f_s}{2}\geq\max\{f_x,f_y,f_{ct}\}$ where $f_{x,y}$ and f_{ct} are the spatial and temporal frequencies respectively. Hence, it is possible to find the required spatio-temporal sampling periods that satisfy the Nyquist condition given by,

$$T_{x,y,ct}\leq\min\left(\frac{1}{2f_x},\frac{1}{2f_y},\frac{1}{2f_{ct}}\right) \tag{3.15}$$

which yields,

$$W_{D\_3D}(\omega_x,\omega_y,\omega_{ct})=\frac{1}{T_xT_yT_{ct}}W_{C\_3D}\left(\frac{\omega_x}{T_x},\frac{\omega_y}{T_y},\frac{\omega_{ct}}{T_{ct}}\right)\ \text{for}\ |\omega_{x,y,ct}|\leq\pi \tag{3.16}$$

where $W_{D\_3D}(e^{j\omega_x},e^{j\omega_y},e^{j\omega_{ct}})\underset{DFT}{\overset{IDFT}{\Leftrightarrow}}w_{D\_3D}(n_x,n_y,n_{ct})$ and $W_{C\_3D}(\frac{\omega_x}{T_x},\frac{\omega_y}{T_y},\frac{\omega_{ct}}{T_{ct}})\underset{FT}{\overset{IFT}{\Leftrightarrow}}w_{C\_3D}(x,y,ct)$.

The relationship in (3.16) confirms that the ROS of the continuous ST-PW in the 3D frequency domain conserves its ROS inside the fundamental Nyquist box $|\omega_{x,y,ct}|\leq\pi$ for the discrete domain ST-PW after rectangular space-time sampling according to (3.15). The choice of spatial and temporal sampling intervals that violate the condition in (3.15) will result in an expansion of the spectrum of a given Nyquist box to subsequent Nyquist boxes creating spatial and temporal aliasing.

3.4.2 The Finite Aperture Effect due to 2D Finite Extent Antenna Arrays

For all phased arrays employed on AA/FPA applications, the spatial samples are of finite extent whereas temporal samples can be approximated to be of infinite extent. The effect of limited spatial array size on the corresponding ROS of the received signal in its frequency domain is referred to as 'the finite aperture effect'. For a 2D-spatial antenna array comprised of $(2N_x+1)\times(2N_y+1)$ antennas, the resultant discrete ST-PW received by the array can be modelled as being rectangularly windowed discrete domain ST-PW as,

$$w_{RD\_3D}(n_x,n_y,n_{ct}) = w_{D\_3D}(n_x,n_y,n_{ct})\times rec_{D\_3D}(n_x,n_y) \tag{3.17}$$

where,

$$rec_{D\_3D}(n_x,n_y) = \begin{cases} 1 & |n_x| \le N_x, |n_y| \le N_y \\ 0 & elesewhere \end{cases} \tag{3.18}$$

The 3D frequency domain representation of (3.17) can be derived as,

$$W_{RD\_3D}(\omega_x,\omega_y,\omega_{ct}) = W_{D\_3D}(\omega_x,\omega_y,\omega_{ct}) *** REC_{D\_3D}(\omega_x,\omega_y)\delta(\omega_{ct}) \tag{3.19}$$

where, $W_{RD\_3D}(\omega_x,\omega_y,\omega_{ct}) \underset{DFT}{\overset{IDFT}{\Leftrightarrow}} w_{RD\_3D}(n_x,n_y,n_{ct})$ and $REC_{D\_3D}(\omega_x,\omega_y) \underset{DFT}{\overset{IDFT}{\Leftrightarrow}} rec_{D\_3D}(n_x,n_y)$ is given by,

$$REC_{D\_3D}(\omega_x,\omega_y) = \frac{\sin\left(\omega_x \frac{(N_x+1)}{2}\right)\sin\left(\omega_y \frac{(N_y+1)}{2}\right)}{\sin\left(\frac{\omega_x}{2}\right)\sin\left(\frac{\omega_y}{2}\right)} \tag{3.20}$$

It is known that $W_{D\_3D}(\omega_x,\omega_y,\omega_{ct})$ has a ROS on a line through the origin given by its space-time DOA in $(\omega_x,\omega_y,\omega_{ct}) \in \mathbf{R}^3$; thus, the convolution of $W_{D\_3D}(\omega_x,\omega_y,\omega_{ct})$ with (3.20) as expressed in (3.19) would result in a spatial smearing of the original ROS along every plane $\left(|\omega_x,\omega_y| \in \mathbf{R}^2\right) \le \pi$ across $|\omega_{ct}| \le \pi$.

Fig.3-6 is an illustration of the magnitude of $REC_{D\_3D}(\omega_x,\omega_y)$ within $|\omega_x,\omega_y| \le \pi$ for $N_y = N_x = 5$. The main lobe covers an area, $|\omega_x,\omega_x| \le \left(\frac{2\pi}{(2N_x+1)},\frac{2\pi}{(2N_y+1)}\right)$ whereas $(2N_x-1)$ and $(2N_y-1)$ side lobes are dominant along the ω_x and ω_y axes respectively. In other words, the width of the main lobe is inversely proportional to the size of the array, and the number of dominant side lobes is proportional to the size of the array. Therefore,

as the size of the 2D spatial array is increased to $N_x = N_y = 30$ the main lobe is narrowed and the number of dominant side lobes is increased. Magnitude of $REC_{D\_3D}(\omega_x, \omega_y)$ at $N_x = N_y = 30$ is illustrated in Fig.3-7.

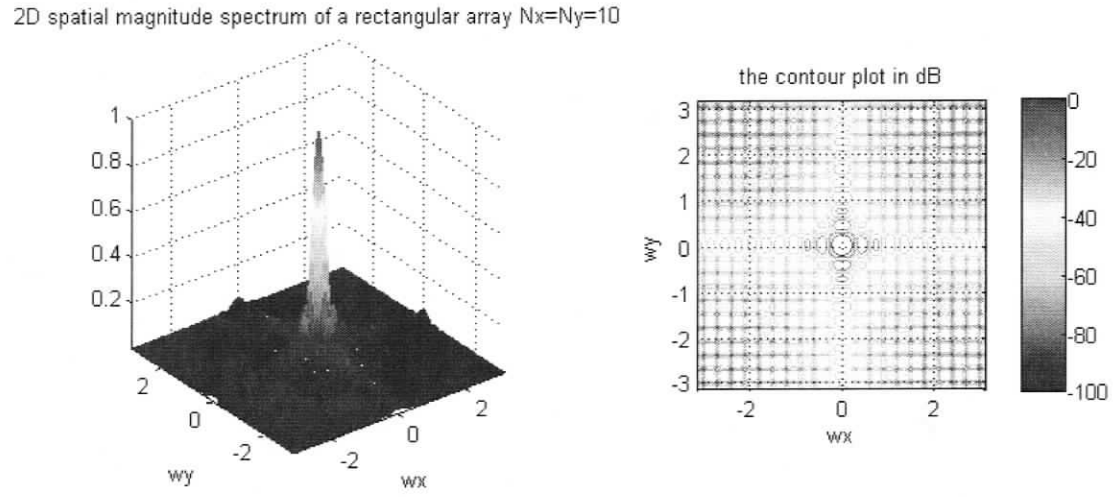

(a) (b)

Figure 3-6. (a) The magnitude frequency response of a 2-D uniformly-weighted rectangular array of $(2N_x+1)\times(2N_y+1)=(21\times21)$ (b) contour plot scaled in dB

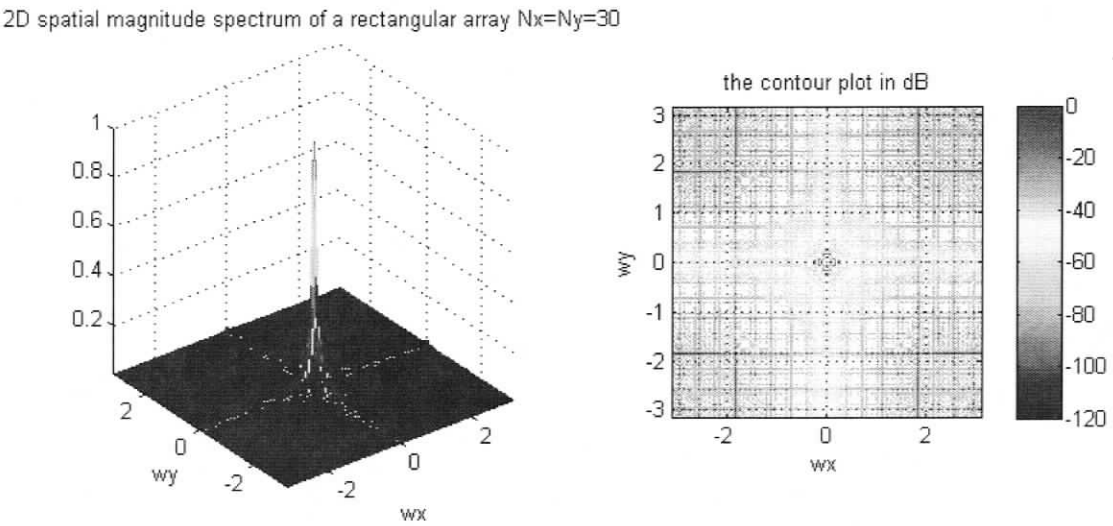

(a) (b)

Figure 3-7. (a) The magnitude frequency response of a 2-D uniformly-weighted rectangular array of $(2N_x+1)\times(2N_y+1)=(61\times61)$ (b) contour plot scaled in dB

Therefore, the convolution of $W_{D\_3D}(\omega_x,\omega_y,\omega_{ct})$ with $REC_{D\_3D}(\omega_x,\omega_y)$ as expressed in (3.19) leads to spatial smearing introduced by $REC_{D\_3D}(\omega_x,\omega_y)$. This results in spectral broadening and leakage of the original ROS of $W_{D\_3D}(\omega_x,\omega_y,\omega_{ct})$. The broadening of the ROS of $W_{D\_3D}(\omega_x,\omega_y,\omega_{ct})$ is due to the broadening of the main lobe of $REC_{D\_3D}(\omega_x,\omega_y)$ whereas the leakage is due to the side lobes of $REC_{D\_3D}(\omega_x,\omega_y)$. Broadening and leakage are governed by the size of the spatial array size $(2N_x+1)\times(2N_y+1)$.

3.5 Numerical Simulation Analysis in the 3D Spatio-Temporal frequency Domain of BB ST RFI Incident on FPAs/AAs and BB ST SOI on AAs

To illustrate the ROS of BB ST-PW, a ST-PW is synthesised by superimposing monochromatic equi-amplitude cosine functions in the form,

$$w_{PW}(n_x,n_y,n_{ct}) = \sum_{k=1}^{k_{MAX}} \cos(2\pi f_k q) \quad ..\mathbf{f} = [f_1, f_2 .... f_{k_{MAX}}] \tag{3.21}$$

where $q \equiv [\sin\theta\cos\phi n_x T_x + \sin\theta\sin\phi n_y T_y + n_{ct} T_{ct}]$, $T_{x,y,ct} \in \mathrm{R}^1$ are the spatial sampling intervals , $n_{x,y,ct} \in \mathrm{Z}^1$ and (θ,ϕ) are the elevation and azimuth angles of the spatial DOA respectively.

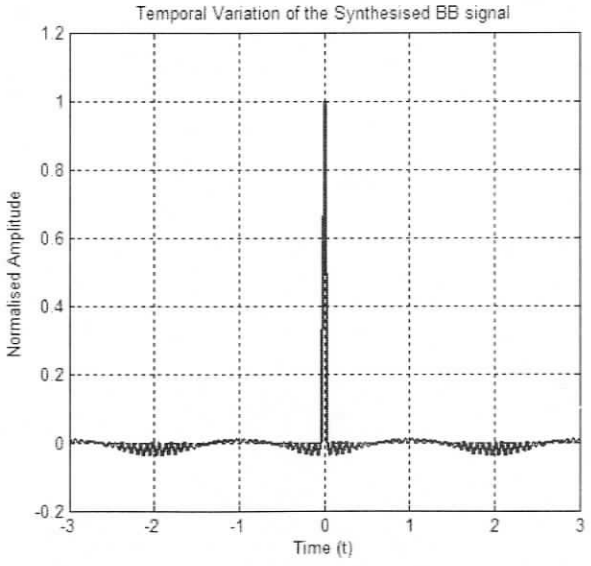

Figure 3-8. The temporally BB signal synthesised by superimposing equi-amplitude cosine functions of frequencies $\mathbf{f} = [0.05, 0.1, 0.15 .... 4]GHz$ as in (3.21).

The temporal variation of the synthesised BB signal in (3.21) is shown in Fig.3-8. Such a synthesised signal is used to illustrate the properties of a BB ST-PW and $f_{k_{MAX}} = 4GHz$ is chosen with $\mathbf{f} = [0.05,0.1,0.15...4]GHz$ to emphasise on wide-band analysis. Assuming that the speed of light is $c = 0.3Gm/s$ the corresponding slightly over-sampled spatio-temporal sampling distances are chosen to be, $T_{x,y,ct} = T_s = \frac{1}{f_s} == 0.0366m$ such that $\frac{f_s}{2} = \frac{4.1GHz}{3Gm/s}$. It should be noted that this is an example of a BB ST-PW and does not represent a generalised model for all BB RFI/SOI signals.

Consider three plane waves, PW-1($\theta = 0, \phi = 90$), PW-2 ($\theta = 85, \phi = 0$) and PW-3 ($\theta = 80, \phi = 45$). Without loss of generality we may assume that PW-1 satisfies the condition in (3.7); therefore it can be considered as a SOI received by the AA, whereas PW-2 and PW-3 satisfy the condition in (3.6); hence they are BB ST RFI signals received by FPA or AA. 3D ST representation of the BB ST PW signals, PW-1($\theta = 0, \phi = 90$), PW-2 ($\theta = 85, \phi = 0$) and PW-3 ($\theta = 80, \phi = 45$) as in (3.17) for $|n_{x,y,ct}| \leq 40$ is illustrated in Fig.3-9. The corresponding 3D spatio-temporal frequency domain representation of the signals in the fundamental Nyquist box $|\omega_{x,y,ct}| \leq \pi$ is illustrated in Fig.3-10. In these simulations the size of the array is set to $N_x = N_y = 40$.

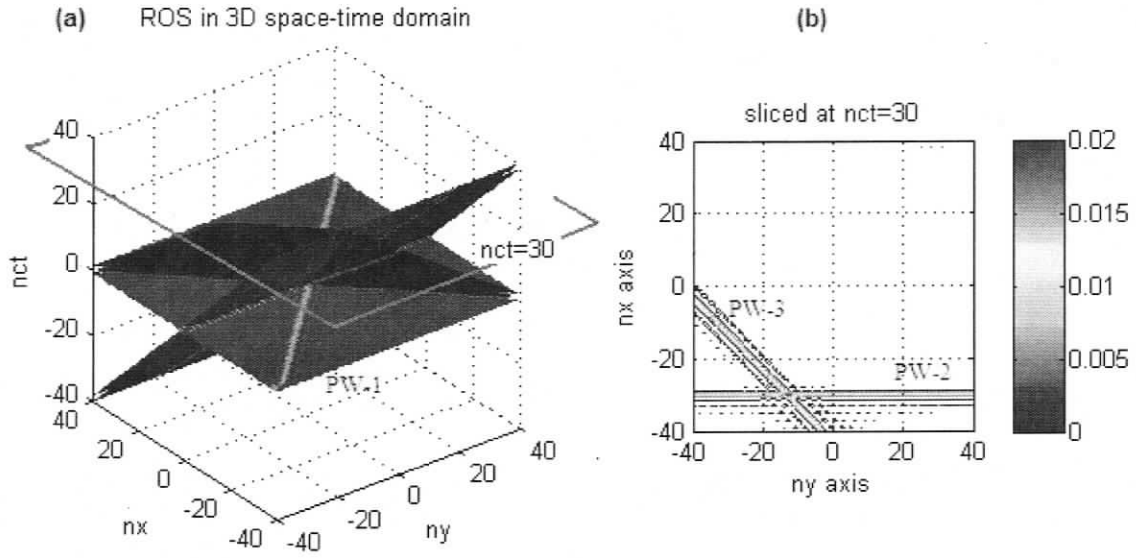

Figure 3-9 3D ST representation of the BB ST PW signals, PW-1($\theta=0,\phi=90$), PW-2 ($\theta=85,\phi=0$) and PW-3 ($\theta=80,\phi=45$) as in (3.17) for $|n_{x,yct}|\le 40$ (a) ROS containing 90.39% energy (b) contour plot at slice $n_{ct}=30$

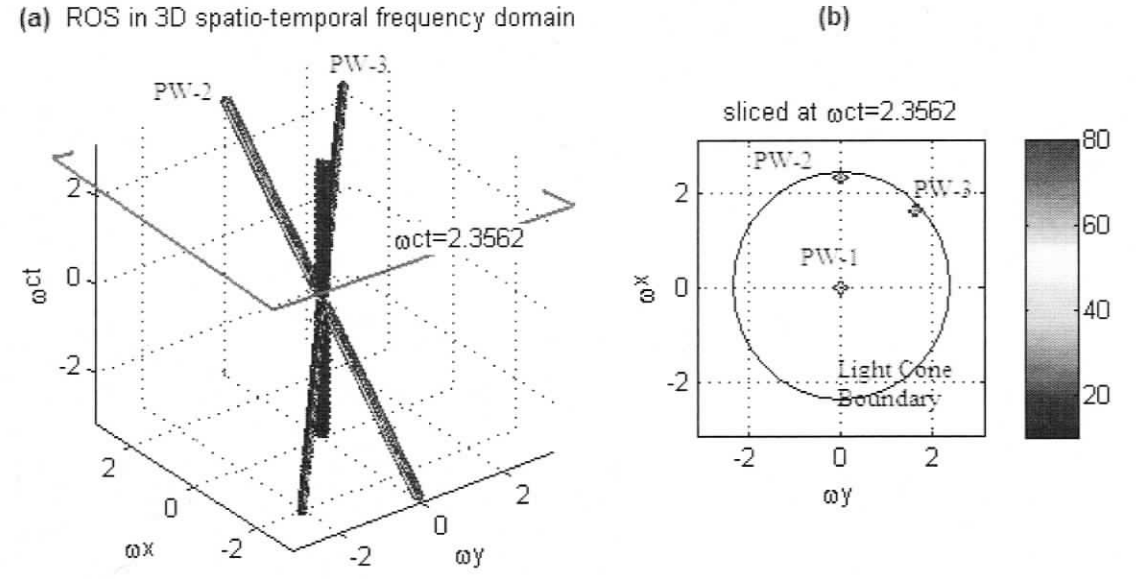

Figure 3-10. 3D spatio-temporal frequency domain representation of the BB ST PW signals, PW-1($\theta=0,\phi=90$), PW-2 ($\theta=85,\phi=0$) and PW-3 ($\theta=80,\phi=45$) as in (3.19) in the fundamental Nyquist box $|\omega_{x,y,ct}|\le\pi$ (a) ROS containing 88.23% energy (b) contour plot at slice $\omega_{ct}=2.3562$

Fig. 3-11(a) illustrates the case of aperture size of $N_x = N_y = 30$, and 3-11(b) illustrates the aperture size of $N_x = N_y = 10$. As can be observed from 3-11(b) in comparison to 3-11(a), lowering the size of the aperture increases the smearing of the initial ROS of the spectrum along (ω_x, ω_y) space. It is clearly evident when the contour slice at $\omega_{ct} = 2.3562$ of Fig.3-11(b) is compared to Fig.3-11(a), that the spectral broadening has smeared the ROS to the exterior of the spectral light cone as well.

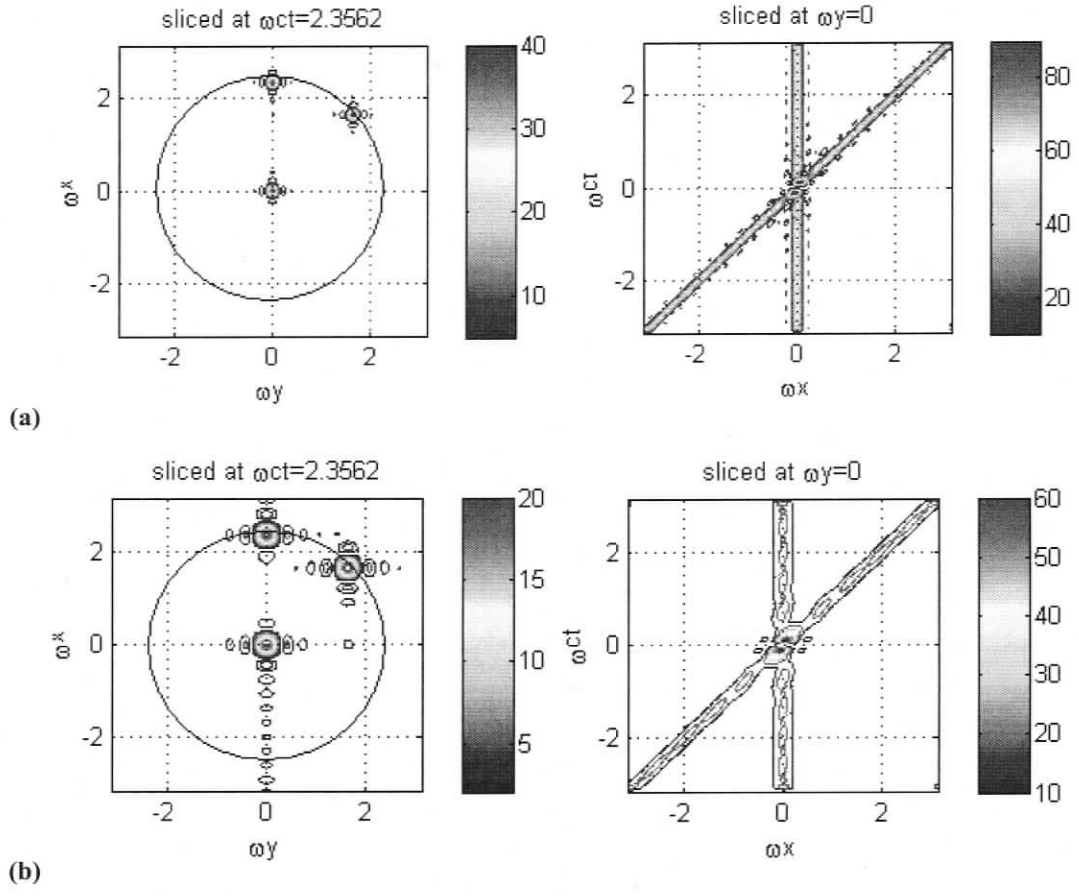

Figure 3-11. 3D spatio-temporal magnitude spectrum of BB ST PW signals, pw-1($\theta = 0, \phi = 90$), pw-2 ($\theta = 85, \phi = 0$) and pw-2 ($\theta = 80, \phi = 45$) as received by uniformly-weighted rectangularly-sampled array size of (a) $N_x = N_y = 30$ (b) $N_x = N_y = 10$.

Therefore, it can be concluded that, BB ST-PWs have ROSs in the 3D spatio-temporal domain $\left\{(\omega_x, \omega_y, \omega_{ct}) \middle| \in \mathbf{R}^3\right\} \leq \pi$ as line spectra through the origin with an orientation given by

their ST DOAs. These ROSs undergo spectral broadening and leakage from the original ROS due to the finite aperture effect of the array. Consequently, BB ST-PWs with a DOA along or close to the array, this effect results in a smearing exterior to the spectral light cone $\omega_{ct}^2 > \omega_x^2 + \omega_y^2$.

3.6 A Review of Broadband ST SOI on FPAs

A ST-PW impinging on the parabolic reflector, induces surface currents which radiate "Huygens Waves" towards the FPA. The vectorial addition of such waves over the aperture may form a FPA field distribution which will create a focal spot on the FPA. Therefore the analysis of SOIs on the FPA is complex in comparison to AAs. In [34][36][37], various methods for calculating the field distribution on the FPA are suggested. Calculating the exact field distribution on a practical FPA setup is a complex electromagnetic (EM) field analysis; therefore, numerical software tools such as GRASP [38], are being widely used. In this section, however, we will review the functional form of the FPA field distribution on the FPA for a non-polarised PW using the far-field distribution of a parabolic reflector [36].

3.6.1 The Far-field Distribution of a Parabolic Reflector

The far-field distribution in polar-coordinates (θ,ϕ) at wavelength λ_i is typically derived by assuming that the focal point transmits spherical waves of monochromatic waves of wavelength λ_i towards the parabolic reflector where such wave fronts are being diffracted to create a new outgoing spherical wave-front of a certain distribution. Using the Kirchhoff-Helmholtz diffraction and aperture integration (page-42,[36]), the far-field distribution is therefore derived by,

$$E_{far-field}(\theta,\phi,\lambda_k) = \frac{D^2}{4}\frac{e^{(jkR)}}{R}\int_0^1\int_0^{2\pi} F(a,\chi)e^{\left[-j\frac{kDa}{2}\sin(\theta)\cos(\chi-\phi)\right]} a\,da\,d\chi \tag{3.22}$$

where $k = \frac{2\pi}{\lambda_i}$, D is the diameter, R is the radial distance, $a = \frac{2F\tan(\psi_d/2)}{r}$, $0 \le a < 1$ and χ as illustrated in Fig.3-12. $F(a,\chi)$ is the illumination function of the parabolic reflector given by,

$$F(a,\chi) = A(a,\chi)e^{[j\Phi(a,\chi)]} \tag{3.23}$$

where $A(a,\chi)$ is the amplitude and $\Phi(a,\chi)$ is the phase variation of the illumination function respectively. The amplitude function $A(a,\chi)$ contains both the edge taper (equivalent to feed pattern) and the free-space taper whereas the phase variation $\Phi(a,\chi)$ is dependent on the aberrations of the parabolic reflector. Assuming that the parabolic reflector with no aberrations is illuminated by a uniform feed, the rotational symmetry of the parabolic shape leads to a constant phase variation $\Phi(a,\chi) = constant$, whereas the amplitude function becomes independent of χ, thus $A(a,\chi) \equiv A(a)$. Types of widely used amplitude functions of Gaussian and quadratic distributions are given by,

$$A(a) = e^{(-\eta a^2)},\ \eta = (T_e/20)\ln 10 \text{ and}$$
$$A(a) = 1-(1-\eta)a^2,\ \eta = 10^{T_e/20} \tag{3.24}$$

respectively, where T_e is the edge and free-space taper in dB.

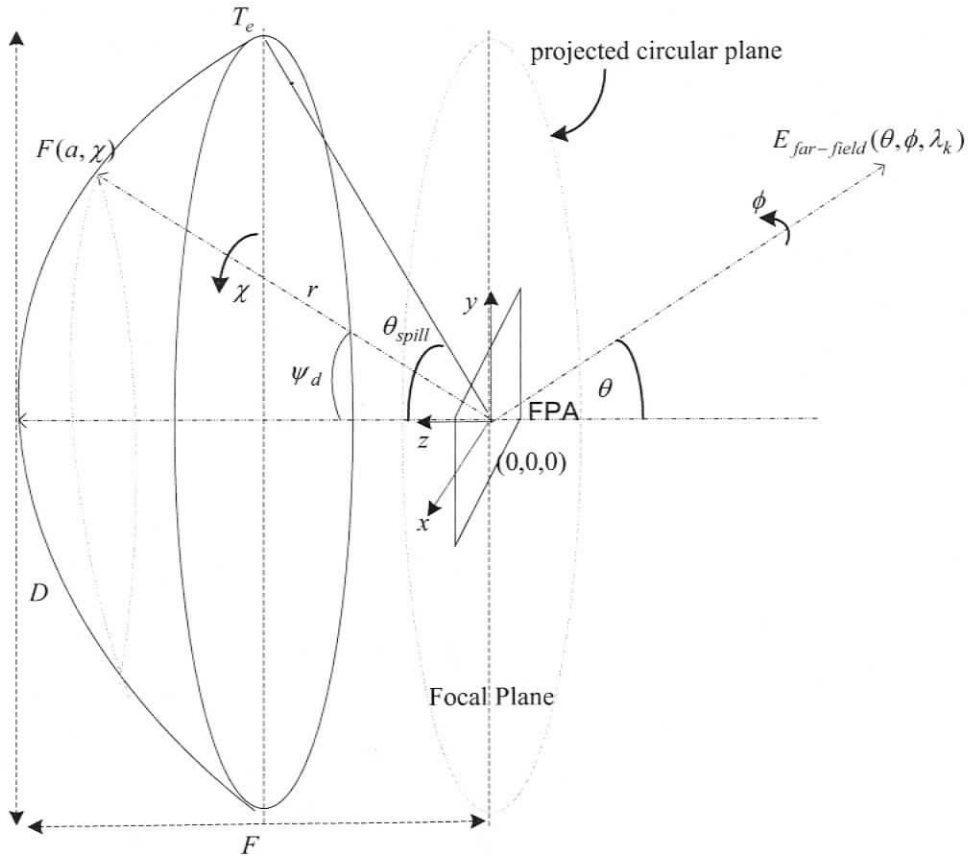

Figure 3-12. Physical structure of a parabolic reflector with an FPA in its phase center

In what follows, we assume the $T_e = 0$ and without aberrations (constant illumination $F(a,\chi)$) on the parabolic reflector; therefore, (3.22) can be simplified to yield [36],

$$E_{far-field}(\theta,\phi,\lambda_i) = \frac{D^2}{4} C \int_0^1 \int_0^{2\pi} e^{[-jua\cos(\chi-\phi)]} a\, da\, d\chi \tag{3.25}$$

where $C = \frac{e^{(jkR)}}{R}$ and $u = \frac{k_i D}{2}\sin(\theta)$ for $k_i = \frac{2\pi}{\lambda}$. The functional form of (3.25) is similar to the Hankel transformation [see Chapter-5 derivation of (5.23)] applied on a circular aperture plane of the parabolic reflector projected on to the focal plane illustrated in Fig.3-12. This also implies that the functional form of the far-field distribution of a parabolic reflector can also be derived by the Fourier transformation applied to the circular aperture plane of the parabolic reflector.

3.6.2 Field Distribution on the FPA

According to [36], due to the general principle of reciprocity, the functional form of the field distribution on the FPA is equivalent to the far-field (Fraunhofer region) distribution of the parabolic reflector. The integration over χ of (3.25) yields the Bessel function $J_0(.)$ of first kind of order zero (see Chapter-4 Section 4.4) and therefore (3.25) can further be simplified to,

$$\begin{aligned} E_{far-field}(\theta,\phi,\lambda_i) &= \frac{D^2}{4} C \int_0^1 J_0(ua)\, a\, da \\ &= C\frac{\pi D^2}{2u} J_1(u) \end{aligned} \tag{3.26}$$

where $J_1(.)$ is the Bessel function of first kind and order one (see Figs. 3-14 and 3-15). The square of the function (3.26) (the power pattern) is usually known as the 'Airy pattern'. In order to achieve a numerically accurate field distribution on the FPA for a given reflector configuration, (3.26) requires a scaling factor d_{scale} [39] to transform from polar-coordinates (θ,ϕ) to rectangular-coordinates (x,y) on the FPA, given by $\theta = \tan^{-1}\left(\sqrt{(x^2+y^2)}/d_{scale}\right) \forall\phi$. In the following simulations the scaling d_{scale} is adjusted using the field distribution simulation results of UC-FPFC [40].

Accordingly, for a broadside (DOA along z) ST PW of frequency f_i (or equivalently $\lambda_i = c/f_i$) impinging on a perfect parabolic reflector that has no aberrations (constant illumination $F(a,\chi)$) may result to a spatial field distribution on the FPA which can be represented as,

$$f_{FPA}(x,y,f_i) = \frac{\pi D^2}{2u} J_1(u) \tag{3.27}$$

where $u = \frac{k_i D}{2}\sin(\theta)$ and $\theta = \tan^{-1}\left(\sqrt{(x^2+y^2)/d_{scale}}\right) \forall \phi$.

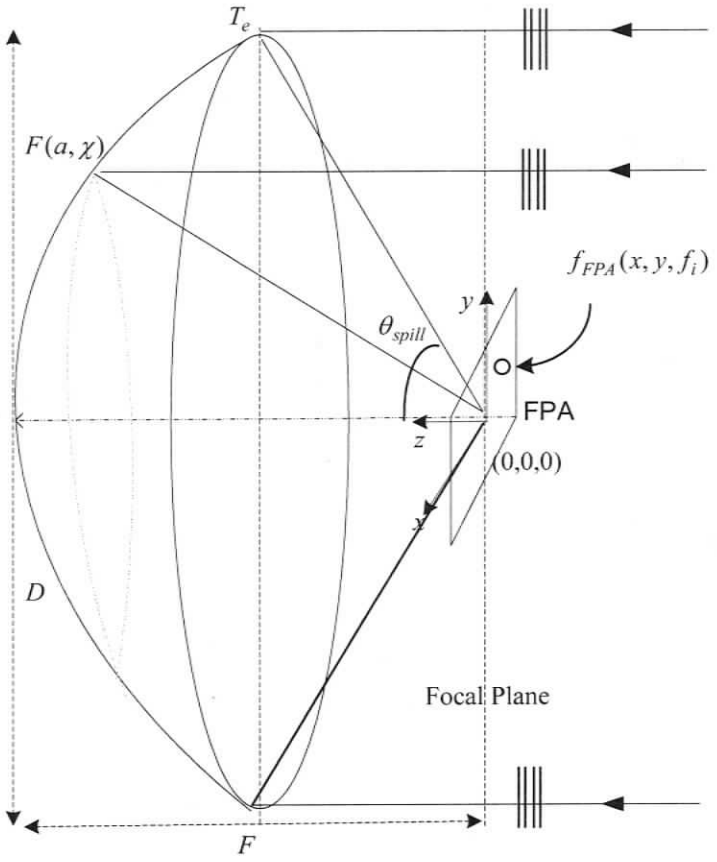

Figure 3-13. Broadside BB SOI (ST-PW) impinging on the parabolic reflector and being focused on to the FPA

The ST PWs with an incident angle other than the broadside angle, creates a non-zero phase function leading to axial and lateral defocusing effects (coma effect) in the focal field distribution. Further, the radiation blockage by the FPA, support legs, and structural deformations may also introduce aberrations. In the following work, such

effects are assumed to be negligible. Further, to the extent that a broadside ST-PW uniformly illuminates the parabolic reflector, its spectral characteristics will be sufficient to model those of a general BB SOIs on FPAs.

3.6.3 A Numerical Simulation of the Field Distribution on FPAs

In order to numerically calculate the field distribution as derived in (3.27), consider a $(2N_x+1)\times(2N_y+1)=81\times81$ element rectangularly-sampled uniformly-weighted FPA with inter-element distance of 0.036m ($\lambda/2$ corresponding to 4.1GHz). The size of the array is chosen to be higher such that it may reduce the finite aperture effect. To avoid the blockage, this large array is assumed to have setup on a large parabolic reflector configuration (as in Fig.3-13) of diameter D=64m and focal ratio F/D=0.41 (similar to Parkes radio telescope, Australia).

The physical spill-over angle of the reflector is $\theta_{spill}=62.75$ (the corresponding space-time angle is 41.63). Based on the analysis of the field distribution simulation results of UC-FPFC[1] [40] for the same FPA configuration, the scaling factor d_{scale} is adjusted to $d_{scale}=41.9013$ with a 3% tolerance. A comparison of field distributions on the FPA that are obtained using UC-FPFC and also from the far-field radiation pattern method with adjusted scaling factor as explained in (3.27), is illustrated in Fig.3-14 for 1GHz and in Fig.3-15 for 4GHz.

From the spatial frequency spectra observed in Figs 3-14 & 3-15, and also at 4.1GHz (not illustrated here), the ROS of a BB ST SOI on the FPA can be approximated as a cone shown in Fig.3-16. According to Fig.3-16, it is evident that the ROS of a broadside BB SOI in the 3D spatio-temporal frequency domain can be approximated by a solid cone.

---

[1] The contribution of the authors of UC-FPFC, Thushara Gunaratne and Dr. Len Bruton of University of Calgary is greatly acknowledged here for performing necessary numerical analysis and providing us with the required field distribution data for a FPA configuration of diameter D=64m and focal ratio F/D =0.41 at 1GHz, 4GHz and 4.1GHz frequencies.

(a)

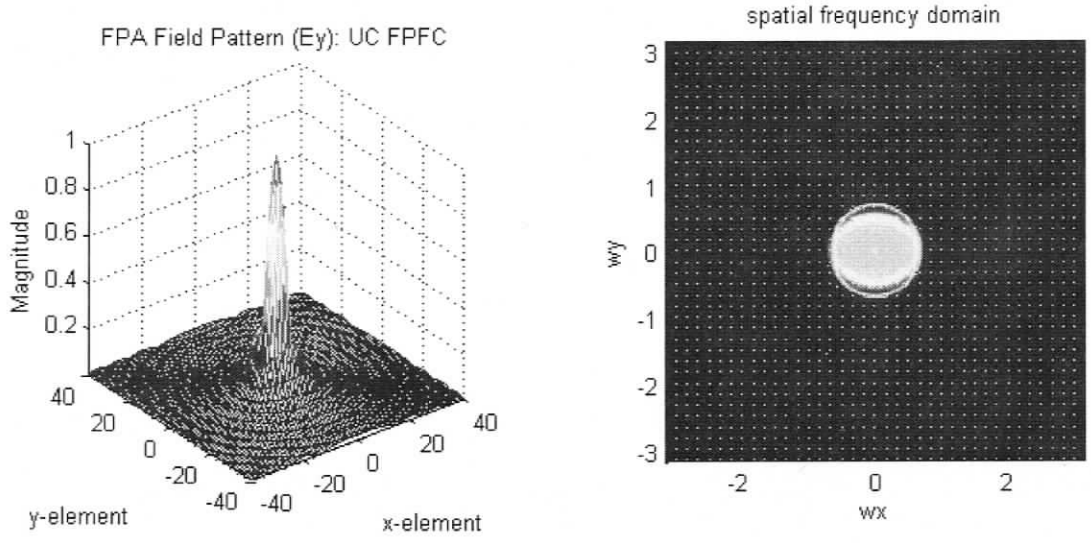

(b)

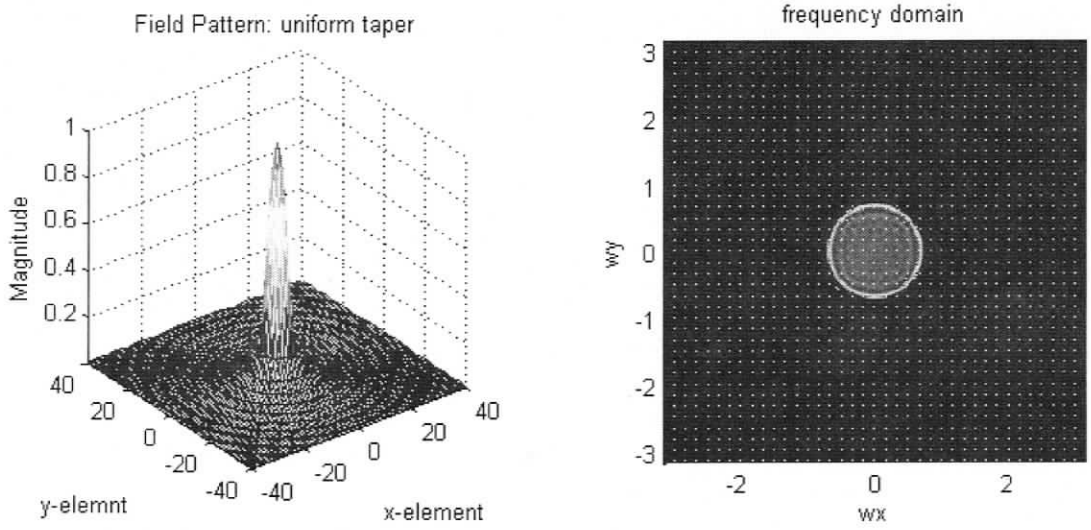

Figure 3-14. $f_k = 1GHz$: Comparison of Focal Field Patterns (left) and the ROS of the spatial spectrum(right); (a) obtained by UC-FPFC, (b) using far-field functional form of (3.27) in a FPA set-up as in Fig.3-13 of diameter D=64m and focal ratio F/D=0.41

(a)

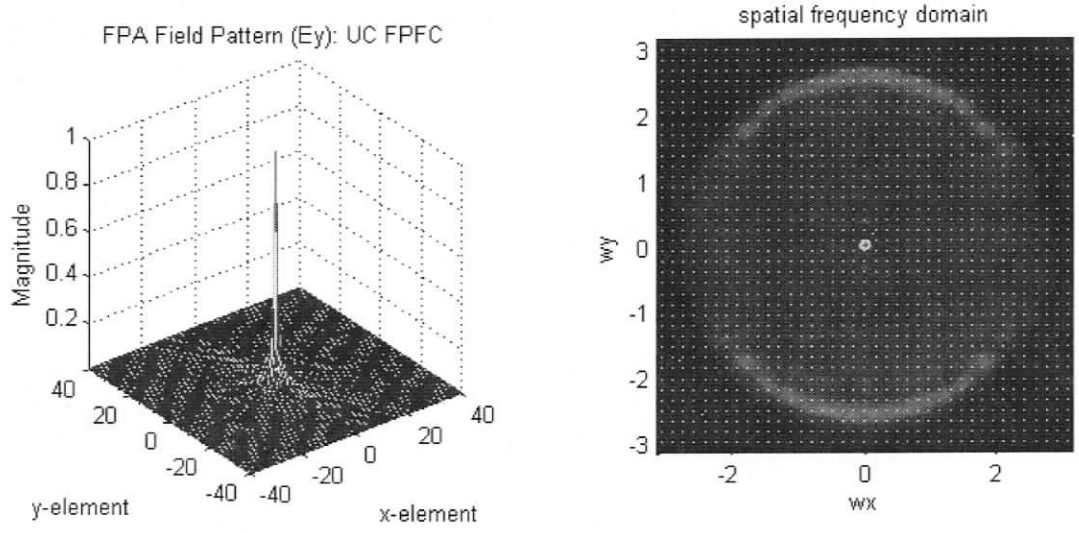

(b)

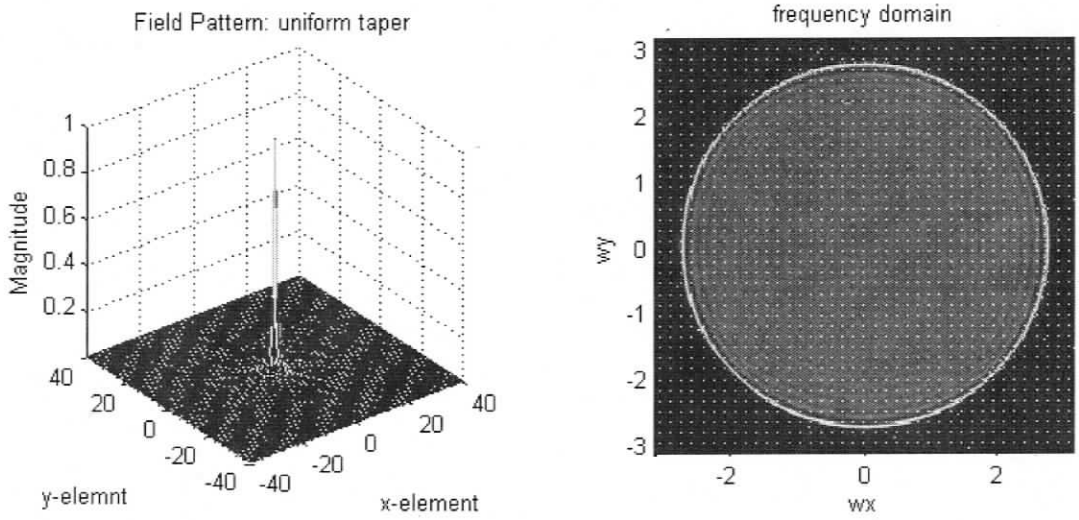

Figure 3-15. $f_k = 4GHz$: Comparison of Focal Field Pattern (left) and the ROS of the spatial spectrum (right); (a) obtained by UC-FPFC, (b) using far-field functional form of (3.27) in a FPA set-up as in Fig.3-13 of diameter D=64m and focal ratio F/D=0.41

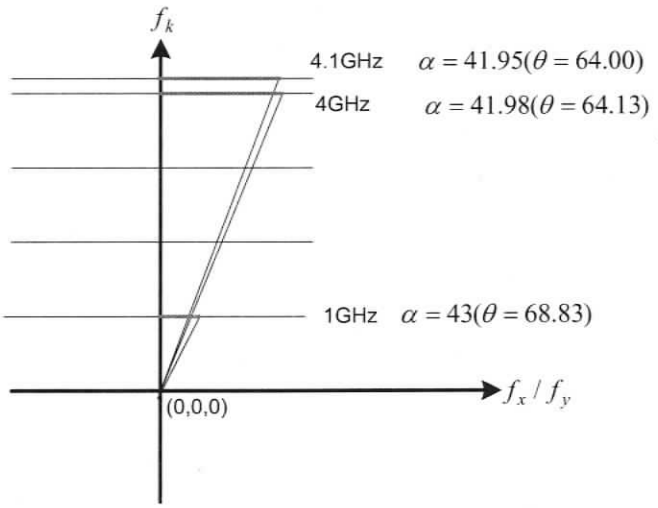

Figure 3-16. An approximation of the ROS of broadside BB SOI in the 3D spatio-temporal frequency domain for an FPA setup with diameter D=64m and focal ratio F/D=0.41

3.6.4 A Numerical Simulation of the BB SOI on FPAs and its ROS in the 3D Spatio-Temporal Frequency Domain

A continuous space-time domain $(x, y, ct) \in \mathbf{R}^3$ broadside BB non-polarised ST-PW incident on the parabolic reflector may undergo spatial amplitude distribution at each frequency f_i resulting the $w_{C\_SOI\_FPA}(x, y, ct)$ on the FPA. In order to investigate the 3D ROS of a BB SOI signal received by the FPA, consider a broadside BB ST-PW composed of monochromatic equi-amplitude cosines series of a certain bandwidth being incident on the parabolic reflector. Such a synthesised signal is expected to be useful to observe the BB properties of the SOI received by the FPA in the spatio-temporal frequency domain. Therefore, consider BB field distribution on the FPA represented as,

$$w_{C\_B\_FPA}(x, y, ct) = \sum_{k=1}^{k_{MAX}} f_{FPA}(x, y, f_k)\cos(2\pi f_k q) \tag{3.28}$$

where $\mathbf{f} = [f_1, f_2 .... f_{k_{MAX}}]$, $q = ct$ and $f_{FPA}(x, y, f_k)$ is the field distribution on the FPA as in (3.27). Using the continuous Fourier transform, the 3D frequency domain $(\Omega_x, \Omega_y, \Omega_{ct}) \in \mathbf{R}^3$ representation of (3.28) can be derived as,

$$W_{C\_B\_FPA}(\Omega_x, \Omega_y, \Omega_{ct})$$
$$= \sum_{k=1}^{k_{MAX}} \left[F_{FPA}(\Omega_x, \Omega_y, f_k)\delta(\Omega_{ct})\right] *** \left[\delta(\Omega_x)\delta(\Omega_y)\left(\frac{\delta(\Omega_{ct} + 2\pi f_k) + \delta(\Omega_{ct} - 2\pi f_k)}{2}\right)\right]$$

$$= \sum_{k=1}^{k_{MAX}} F_{FPA}(\Omega_x, \Omega_y, f_k) \left(\frac{\delta(\Omega_{ct} + 2\pi f_k) + \delta(\Omega_{ct} - 2\pi f_k)}{2} \right) \tag{3.29}$$

where $F_{FPA}(\Omega_x, \Omega_y, f_k) \overset{IFT}{\underset{FT}{\Leftrightarrow}} f_{FPA}(x, y, f_k)$ and $\left(\frac{\delta(\Omega_{ct} + 2\pi f_k) + \delta(\Omega_{ct} - 2\pi f_k)}{2} \right) \overset{IFT}{\underset{FT}{\Leftrightarrow}} \cos(2\pi f_k ct)$. This implies that a broadside BB PW received at the FPA as given in (3.28) may not confine to a line spectrum in the 3D frequency domain, in contrast to (3.10), due to the term $F_{FPA}(\Omega_x, \Omega_y, f_k)$, which has a circular cross-section with a diameter defined by f_k (the Fourier transform of (3.27)). It is therefore clear, that, in contrast to a line spectrum observed along ω_{ct} for a broadside BB ST-PW for AAs as illustrated in Fig.3-10, a broadside BB ST PW impinging on the parabolic reflector being received at the FPA, will have a smeared ROS in the 3D frequency domain in the form of a solid cone.

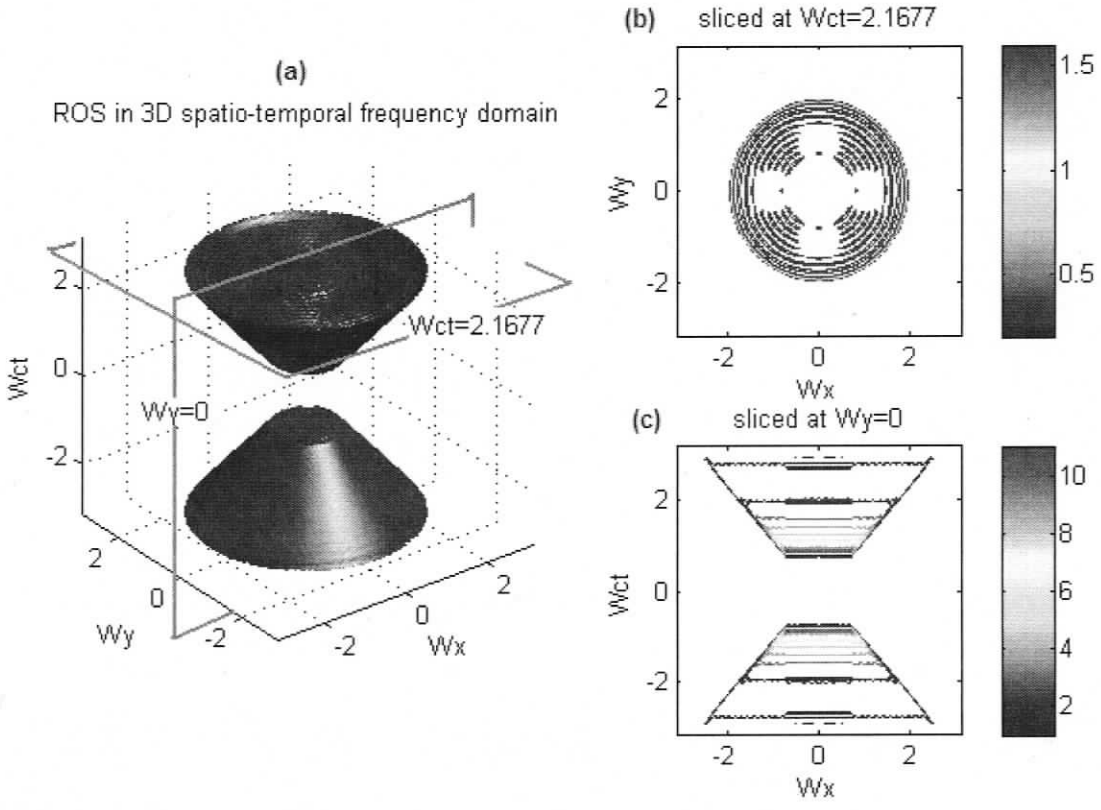

Figure 3-17. The magnitude spectrum of SOI on the FPA due to a broadside broadband (1GHz-4GHz) ST-PW incident on a paraboloidal reflector of diameter D=64m and focal-ratio f/D =0.41; (a) 3D ROS containing 92% energy, (b) a slice at ωct=2.17 and (c) a slice at ωy=0

Fig.3-17. Illustrates the 3D ROS of the magnitude spectrum of a synthesised discrete domain BB SOI due to a broadside BB (1GHz-4GHz) ST-PW focused at the FPA after impinging on a parabolic reflector of diameter D=64m and focal-ratio f/D =0.41. It is observed that the angle of spreading of the ROS of BB SOI is 43^0 at 1GHz and approximately 41.95^0 at 4.1GHz. Therefore, on the given FPA configuration, at uniform illuminations and with no aberrations, the ROS of BB SOI can be approximated by a solid cone[2] with an angle approximated within the range of 41.95^0-43^0 (space-space angles 64.00^0-68.83^0).

3.7 Summary

In this chapter the broadband (BB) radio frequency interference (RFI) and signal of interest (SOI) on aperture arrays (AAs) and focal plane arrays (FPAs) are discussed. The RFI signals incident on AAs are modeled as ST PWs that have DOAs close to the over-the-horizon which may not fall in to the DOAs of SOIs. The analysis of the ROS of BB RFI and BB SOI signals incident on AAs in the spatio-temporal frequency domain indicated that their ROSs (spectral lines) are separable based on the DOAs.

The ST model used for the RFI signals incident on FPAs is similar to that of SOIs and RFIS on AAs. However, the modeling of SOIs on the FPAs is not straightforward where it requires the calculation of the field distribution on the FPA. The functional form of the field distribution on the FPA has been derived using the far-field distribution of the parabolic reflector. To accurately approximate the field distribution on the FPA, the far-field functional form is adjusted using field distribution data obtained from UC-FPFC. Consequently, the ROS of a synthesised broadside BB SOI incident on a FPA in the 3D frequency domain is analysed. The analysis concluded that the ROS of BB SOI on FPAs in the 3D frequency domain may form a solid cone in contrast to a line spectrum in the case of AAs. In order to observe this, the ROS of a synthesised broadside BB SOI in the frequency domain for a given FPA configuration is simulated. Based on the simulation results, it is evident that ROS of a BB SOIs on the FPA would confine to a solid cone.

---

[2] Directions of Dr. Len Bruton as private communication is greatly acknowledged here in reviewing the hypothesis that the ROS of BB SOIs on FPAs can be approximated by a solid cone in 3D frequency domain

Therefore, it is understood that BB RFI signals that have ROSs residing outside this solid cone can be suppressed by employing a suitable ST filter which will enclose BB SOI in its passband.

In conclusion, it is shown that for AA and FPA applications there exist over-the-horizon BB RFI signals that have ROSs outside the ROS of the SOIs in the 3D frequency domain. These BB RFIs have a DOA which is on or close to the horizon and their ROSs in the 3D frequency domain lie mostly on or within the spectral light cone. The separability of these signals may be affected due to the violation of the Nyquist sampling condition, and/or the finite aperture effect of the array. Assuming that the Nyquist condition is satisfied and a sufficiently large aperture size is chosen, an ST filter that completely encloses the ROS of the SOI in its passband and the spectral light cone in its stopband can be employed to mitigate over-the-horizon BB RFI signals.

Chapter 4

3D Space-Time (ST) Modeling and Spectral Analysis of Mutually Coupled (MC) Broadband (BB) signals

In this chapter a novel ST propagation model is investigated to represent mutually coupled (MC) signals that exist on dense broadband (BB) antenna arrays. A theoretical ST model is derived and examined using the scattering parameter data measured from a Vivaldi antenna array to investigate the validity of the proposed theoretical ST model. Then, a theoretical study of the spectral characteristics of BB MC signals is presented, followed by a numerical simulation analysis in 3D space-time and spatio-temporal frequency domains. In this study, two possible MC signal categories are being considered, namely photonically reflected incident waves and internally generated LNA noise waves.

4.1 Introduction

Broadband (BB) antennas are emerging as radiating elements in most modern array configurations. The minimal inter-antenna separation and the geometry of the BB antennas induce currents on to the neighbouring antennas. Such effects are known as mutual coupling [34]. In radio astronomical applications the Low Noise Amplifiers (LNAs) associated with each antenna element in the array generate noise waves that are also mutually coupled to surrounding elements [19]. Previously reported approaches to the synthesis of mutually coupled (MC) signals are based on analytical approaches; therefore, they are suitable for narrowband applications [18] [20] [21] [41] [42]. In this chapter a 3D space-time propagation model is investigated to approximate the behaviour of BB MC signals that are propagating along the surface of a BB antenna array. The MC signals considered in the model may contain both re-scattered (photonically reflected) BB SOIs and/or RFI signals at the antenna [34], as well as the internally-generated disturbances mainly produced at the driving points of LNAs associated with each antenna

[19]. Photonically reflected BB SOIs and/or RFIs affect the radiated array field distribution causing deformations in the final beam pattern, and the MC LNA noise increases the total system noise temperature (T_{sys}). The correlated nature of MC LNA noise has recently been identified as challenging for radio astronomical applications [19].

4.2 3D Space-Time Propagation Model for MC Signals in Antenna Arrays

According to [34] [43], an isotropic wave propagating outward from a point source satisfies the wave equation given by,

$$\nabla^2\psi(.)=\frac{1}{c^2}\frac{\partial^2\psi(.)}{\partial t^2} \tag{4.1}$$

where $\psi(.)$ corresponds to the spatio-temporal variation of the emanating electric field and c is the group velocity of the wave. However, in the 3D space of spherical co-ordinates (r,θ,ϕ), (4.1) exhibit spherical symmetry thus have no dependence on θ or ϕ. Therefore the expansion of the Laplacian operator ∇^2 on spherical coordinates of $\psi(.)$ in (4.1) yields,

$$\frac{\partial^2\psi(.)}{\partial r^2}+\frac{2}{r}\frac{\partial\psi(.)}{\partial r}=\frac{1}{c^2}\frac{\partial^2\psi(.)}{\partial t^2} \tag{4.2}$$

where (4.2) can be further simplified to,

$$\frac{\partial^2(\psi(.)r)}{\partial r^2}=\frac{1}{c^2}\frac{\partial^2\psi(.)}{\partial t^2} \tag{4.3}$$

Equation (4.3) is now in the form of well known homogenous wave equation propagating in a non-conducting medium, thus has two independent solutions. If the source is placed at the origin and the radiation is propagated outward from the source in the radial direction, the corresponding spatio-temporal solution can be chosen to be in the form of,

$$\psi(r,t)=\frac{A}{r}\overline{w}(-r+ct) \tag{4.4}$$

where A is a scalar constant and $\overline{w}$ is the temporal functional form of the emanating BB signal with $-r$ to denote outward propagation. The other solution represents inward propagation; hence it is not considered here. It is, therefore, possible to model the propagation of MC BB signals by (4.4) assuming that it originates from a point like antenna element, where the antenna plane is non-dissipative or non-conductive. However,

most broadband antenna arrays investigated for AAs /FPAs are arrays of tapered slot antennas and their phase centres may be assumed as a point source; however the plane of propagation is conductive and hence does not act as a non-dissipative medium. According to [43] [44], a wave propagating in a dissipative medium embraces complex spatial frequency; therefore, it is subjected to exponential damping of the wave along spatial dimensions. Investigating a general definition for the relationships between the conductivity, the amount of spatial damping and the spatial frequencies, especially in the case of broadband antenna arrays is a complex analysis. To the extent that the spatial damping is independent of spatial frequencies, a simple but realistic model which will approximate the space-time propagation of MC signals on BB antenna arrays is proposed in the form of,

$$w_{MC}(r,ct) = Ae^{-ar}\overline{w}(-r+ct), \qquad r=\sqrt{x^2+y^2} \tag{4.5}$$

where a is an attenuation constant that models the damping of the wave in the radial direction on the antenna plane $(x,y) \in \mathbf{R}^2$. For a spatial attenuation of σ (dB) between two points separated by a distance r_0, the corresponding attenuation constant a can be calculated as,

$$20\log_{10}\left(\frac{e^{-ar}}{e^{-a(r+r_0)}}\right) = \sigma$$

$$a = \frac{1}{r_0}\log_e\left(10^{\sigma/20}\right) \tag{4.6}$$

Approximations to the value of a can be obtained by investigating the previously reported experimental results of transmission coefficients of dense antenna arrays [19] [45]. Furthermore, the reported results in [19] [45] support the ST representation of MC signals as in (4.5). In the next section, the ST propagation model is further justified based on transmission coefficient measurements[3] of a 180-element dense Vivaldi array: DRAO, Canada.

---

[3] Collaboration with Dr.Rick Smeagal is acknowledged here for providing us necessary S-parameter data and for useful discussions with him.

4.3 Experimental Justification of the Space-Time Propagation Model for BB MC Signals Using Transmission Coefficient Measurements of a 180-element Dense Vivaldi Array: DRAO

A 4-port Vector Network Analyser (VNA) has been used to measure S-parameters (transmission and reflection coefficients) of a BB dual-polarised 10x11x2 element dense Vivaldi antenna array. The operational frequency of measurements varies from 900 to 2200 MHz with a resolution of 1MHz (1301 bands) [46] [47]. The symmetry of the array is assumed to display similar characteristics for both vertically and horizontally polarised elements. Hence, in what follows, we only analyse the horizontal element array. The S-parameters are measured for groups each containing four horizontal elements. The structure of the array and some groups which will be used later are illustrated in Fig.4-1.

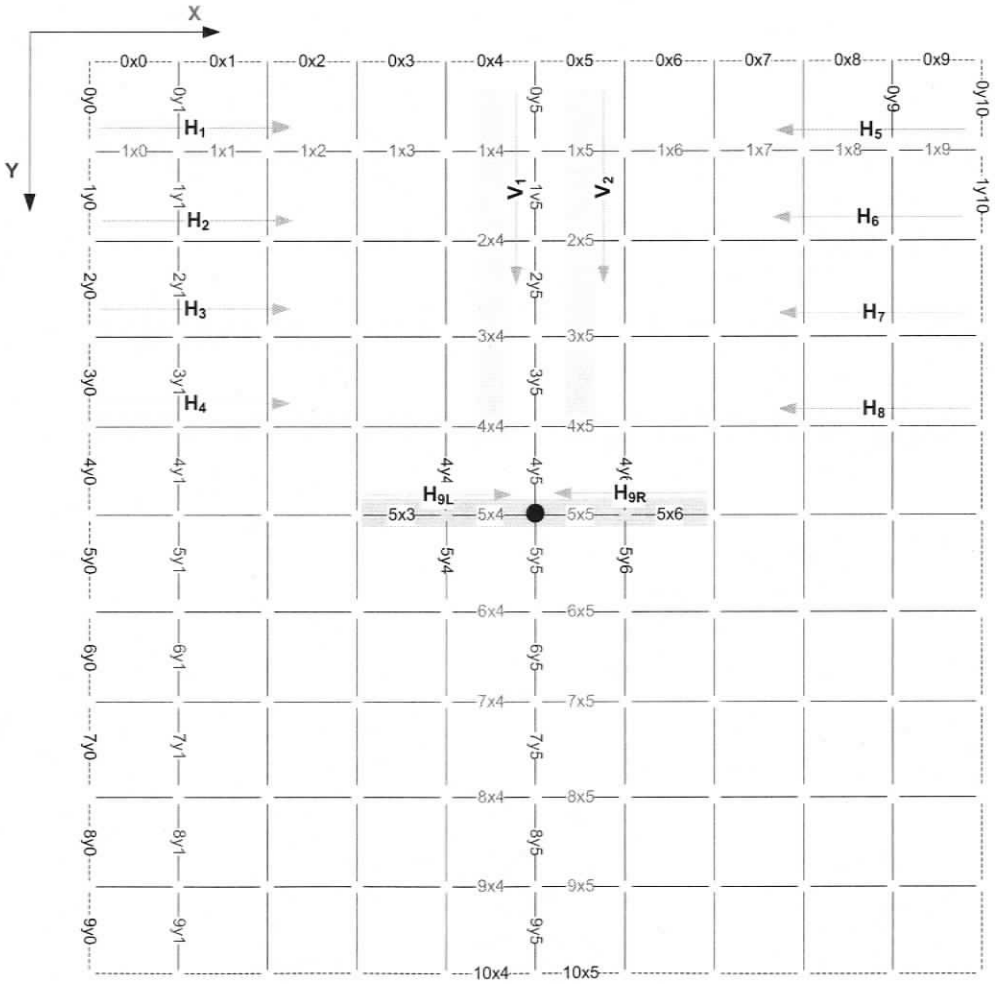

Figure 4-1. 10x11x2 Vivaldi array structure and some of 4-element measurement groups connected to the 4-port Vector Network Analyser (VNA). Dummy elements are placed around

the array denoted by dotted lines and the number of active elements is 180. (Source: Page 23, [10])

The element groups that are highlighted in different colors in Fig.4-1 are accompanied by an arrow to denote the connection sequence to the ports of the VNA. For example; the group H_1, containing elements of 1x0,1x1,1x2,1x3, is connected to the ports of the VNA in a sequence of (1, 2, 3, 4) respectively where the corresponding S-parameters (reflection or transmission coefficients) for ports *(p,q)* is denoted by,

$$S_{pq} = \begin{cases} \dfrac{V_q^{Reflected}}{V_p^{Incedent}} & p = q \\ & \text{where } p,q = 1,2,3,4 \\ \dfrac{V_q^{Transmitted}}{V_p^{Incedent}} & p \neq q \end{cases} \tag{4.7}$$

Only the forward S-parameters or the transmission coefficients, S_{12}, S_{13} and S_{14} are useful, and will be considered to analyse the behaviour of mutually coupled signals.

4.3.1 The Magnitude and Phase Measurements of Forward S-Parameters (Transmission Coefficients) in the Complete Operational Band (900MHz - 2200MHz)

The transmission coefficients measured over the complete operational band for arbitrarily selected groups, H_1, H_5, V_1 and H_5 are illustrated in Figs 4-2 to 4-5. They contain the element-wise magnitude[4] and phase[5] variation of transmission coefficients (in the top row) and inter-element magnitude, and phase variation of transmission coefficients (in the bottom row) for the operational frequency band 900MHz to 2200MHz of the array.

[4] All magnitude values are measured in dB, as $20\log_{10}(S_{pq})$ for $p,q = 1,2,3,4$.

[5] phase angles are first unwrapped[5] within the group (spatial phase unwrapping), and then unwrapped again with respect to frequencies (temporal phase unwrapping).

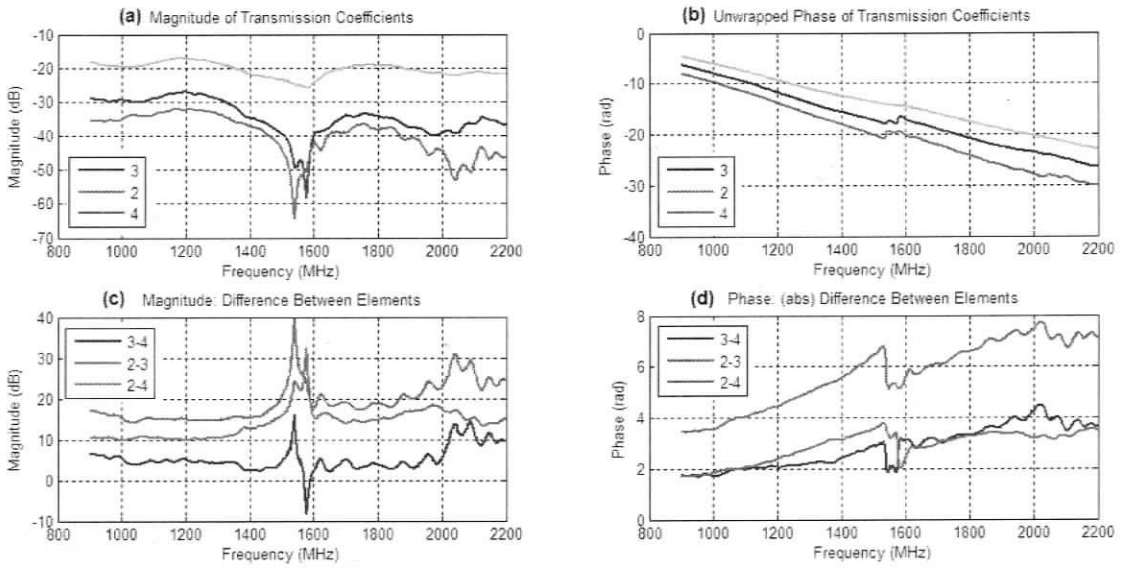

Figure 4-2. Magnitude and Phase variation of Transmission Coefficients of Group H1 (a) Magnitude (b) unwrapped phase (c) magnitude difference (d) absolute phase difference, in the complete operational frequency range 900-2200 MHZ

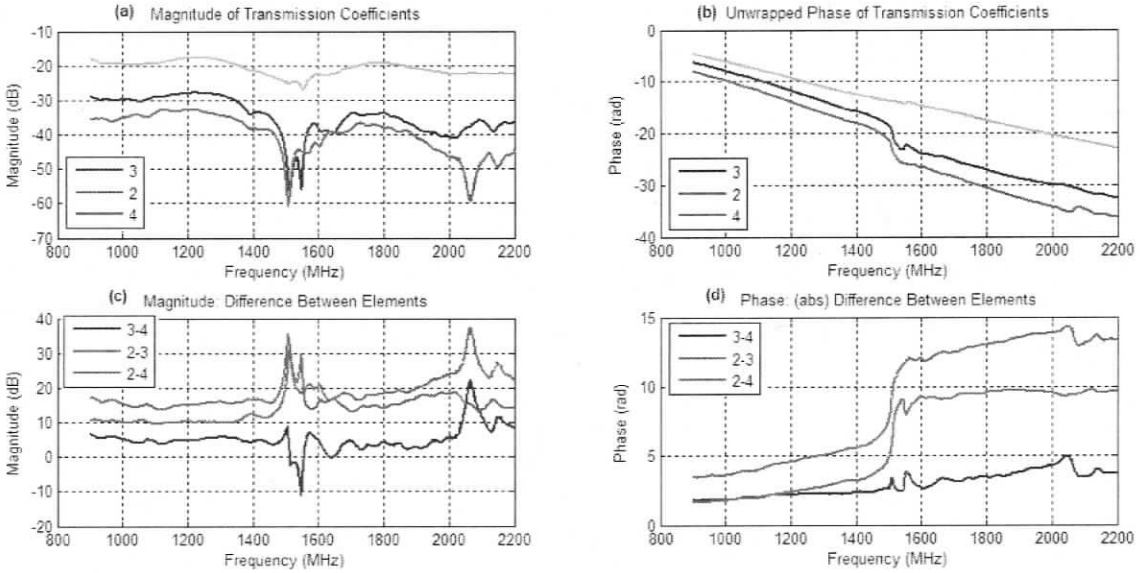

Figure 4-3. Magnitude and Phase variation of Transmission Coefficients of Group H5 (a) Magnitude (b) unwrapped phase (c) magnitude difference (d) absolute phase difference, in the complete operational frequency range 900-2200 MHZ

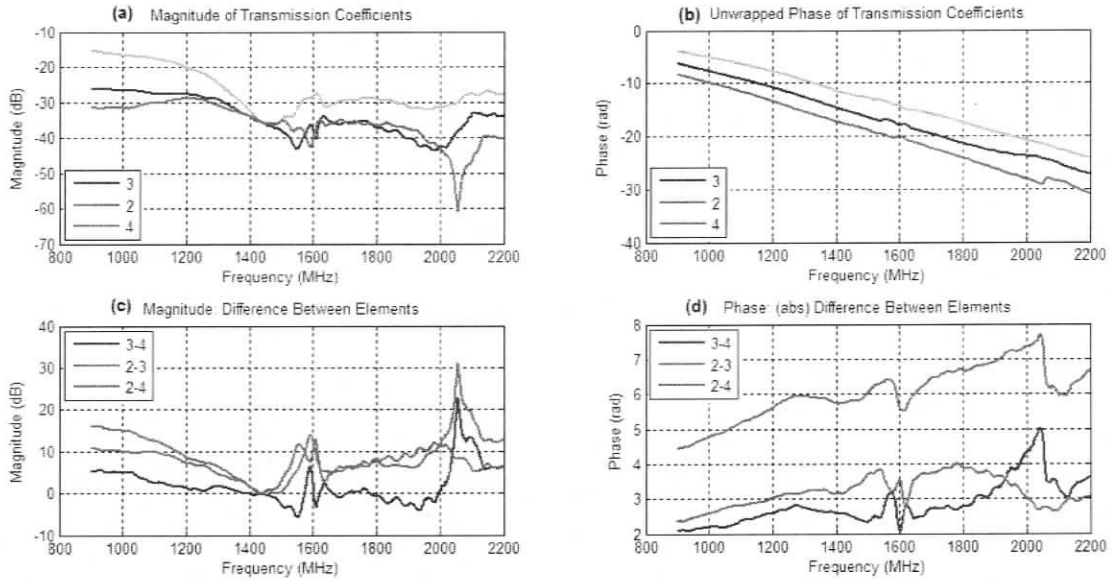

Figure 4-4. Magnitude and Phase variation of Transmission Coefficients of Group V2 (a) Magnitude (b) unwrapped phase (c) magnitude difference (d) absolute phase difference, in the complete operational frequency range 900-2200 MHZ

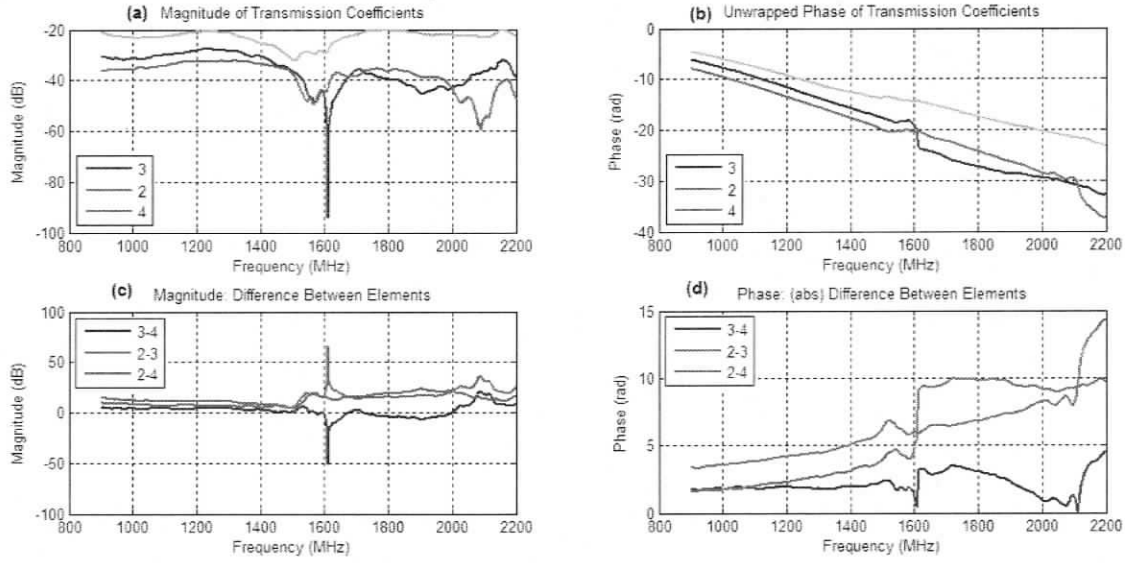

Figure 4-5. Magnitude and Phase variation of Transmission Coefficients of Group H9L (a) Magnitude (b) unwrapped phase (c) magnitude difference (d) absolute phase difference, in the complete operational frequency range 900-2200 MHZ

It is evident from Figs 4-2 to 4-5, that the transmission coefficients display non-consistent behaviour in the frequencies closer to 1.6GHz and 2.1GHz, possibly due to the resonance effects of densely placed Vivaldi antennas. A definite explanation for this behaviour is not investigated and is not within the scope of this work. Therefore, the

measurements in the frequency ranging approximately between 1.4-1.6GHz and 2-2.1GHz are not under consideration.

In the frequency range between 0.9GHz-1.4GHz all element groups show consistent behaviour in magnitude and phase variation of transmission coefficients. The groups H_1, H_5, V_2 and H_{9L} show approximately $\sigma =$ 20dB between element 1-2 (H_{9L} has a wide variation but with an average of $\sigma =$ 20dB) , approximately $\sigma =$ 10dB between element 2-3, and approximately $\sigma =$ 5dB between element 3-4. A similar behaviour is also observed in the frequency range between 2.1GHz-2.2GHz. The phase variation in both these frequency ranges is approximately linear. In the frequency range of 1.6GHz-2GHz however, only the groups of H_1 and H_5 show a consistent behaviour similar to the behaviour seen in the frequency band 0.9GHz-1.4GHz, whereas groups V_2 and H_{9L} show non-consistent behaviour from element 3-4. Again, a definite explanation to this behaviour between elements 3-4 is unknown and is not within the scope of this thesis. To obtain a broader idea about the inter-element attenuation of all element groups, the magnitude and phase variation between elements 2-4 is observed for the complete frequency band and illustrated in Fig.4-6.

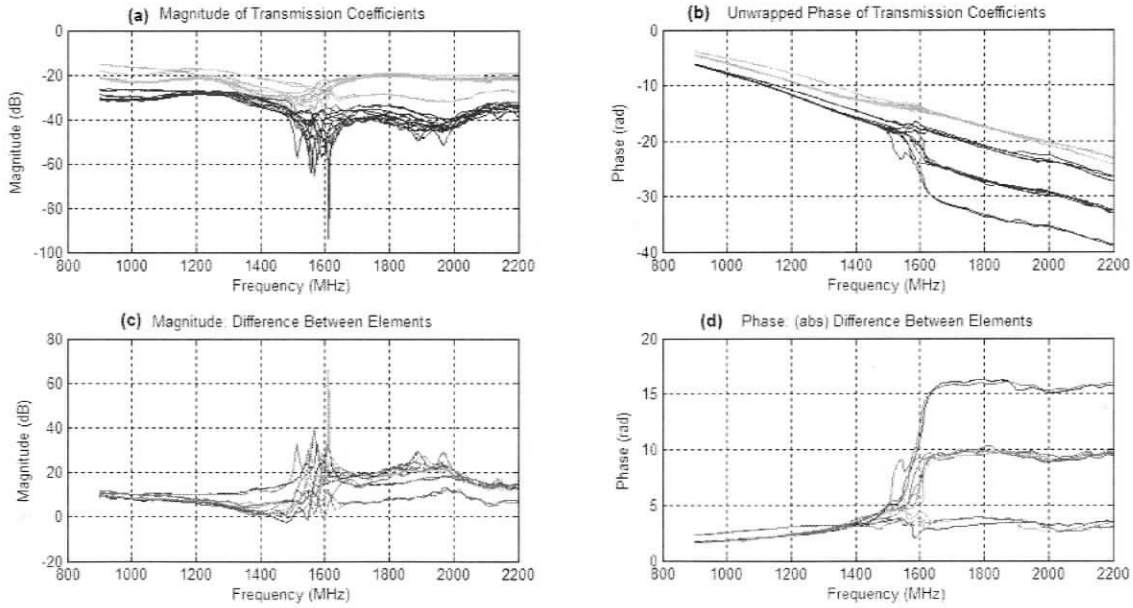

Figure 4-6 Magnitude and Phase variation of Transmission Coefficients between elements 2 -> 4 with respect to element 1, for all linear groups V1-2, H1-8 and H9L-9R in the complete operational frequency band 900-2200 MHZ

Fig.4-6 clearly indicates that the average inter-element attenuation between element 1-2, is approximately $\sigma =$ 20dB in the complete frequency bands of interest, whereas, average inter-element attenuation between element 2-4, is approximately $\sigma =$ 15dB in the frequency ranges 0.9GHz-1.4GHz and 1.6GHz-2GHz, and approximately $\sigma =$ 20dB in the frequency range 2.1GHz-2.2GHz. The phase variation on the other hand is observed to be linear for all groups confirming the circularly symmetric propagation of the coupling wave.

To observe the attenuation and phase pattern of transmission coefficients of all element groups, a frequency of 919MHz is selected such that it falls within the consistently behaved frequency range 0.9GHz-1.4GHz. The overlaid attenuation and phase pattern of transmission coefficients of all element groups is shown in Fig.4-7. The phase variation observed in Fig.4-7 validates the circularly symmetric propagation of MC signals where, as the magnitude variation indicates, it can be closely approximated by a linear function. A linear function in the dB scale translates to an exponentially decaying function in the spatial domain.

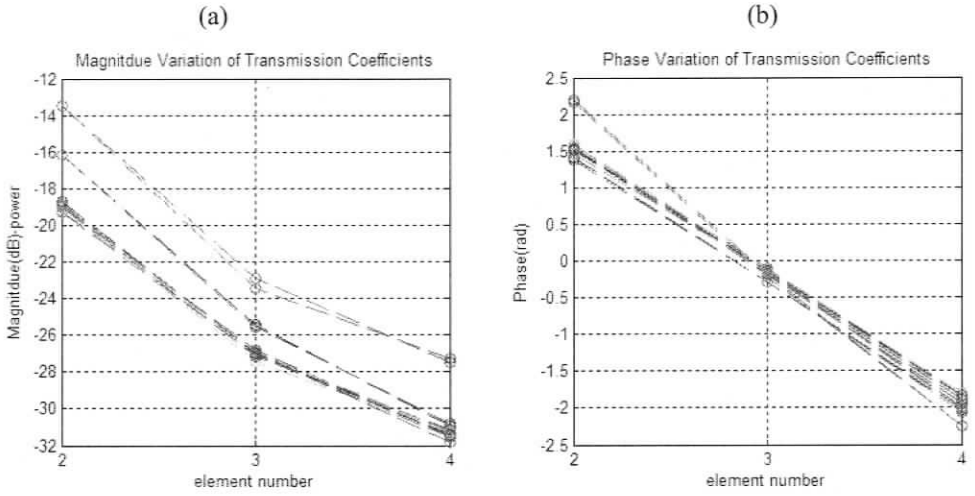

Figure 4-7. Attenuation Pattern: (a) Magnitude and (b) Phase variation, of Transmission Coefficients at, elements-2,3&4 with respect to element-1, of all linear groups shown in Fig.1, at operating frequency 919MHz.

By observing the attenuation patterns in the complete frequency bands of interest, an estimated value of inter-antenna attenuation σ between 15-20dB is found to be a close approximation to the inter-element attenuation for this Vivaldi array.

4.4 ROS of Continuous Domain Broadband Mutually Coupled ST Signals Emanating from the Middle Element, in the 3D Spatio-Temporal Frequency Domain

The propagation model explained in (4.5) is defined in the continuous space-time domain $(x, y, ct) \in \mathbf{R}^3$ whereas the origin of the wave may not necessarily be in the origin of the spatial dimensions $(x, y) \in \mathbf{R}^2$. Without loss of generality let us assume that the wave is emanated from the origin $(x, y) = (0,0)$ of an infinitely extent continuous domain 2-D sensor. Therefore, the MC signals received by the continues 2-D sensor can be expressed as,

$$w_{C\_MC}(x, y, ct) = e^{-a\sqrt{x^2+y^2}}\, \overline{w}(-\sqrt{x^2 + y^2} + ct) \tag{4.8}$$

where the corresponding continuous domain spatio-temporal frequency spectrum is derived by,

$$W_{C\_MC}(\Omega_x, \Omega_y, \Omega_{ct}) = \int_{-\infty}^{\infty}\int_{-\infty}^{\infty}\int_{-\infty}^{\infty} e^{-a\sqrt{x^2+y^2}}\, \overline{w}(-\sqrt{x^2 + y^2} + ct) e^{-j(x\Omega_x + y\Omega_y + ct\Omega_{ct})}\, dxdydct \tag{4.9}$$

where $(\Omega_x, \Omega_y, \Omega_{ct}) \in \mathbf{R}^3$. To thoroughly analyse the ROS of $W_{C\_MC}(\Omega_x, \Omega_y, \Omega_{ct})$ a Cartesian to spherical coordinate transformation is done as illustrated in Fig.4-8, to obtain a simplified expression of (4.9).

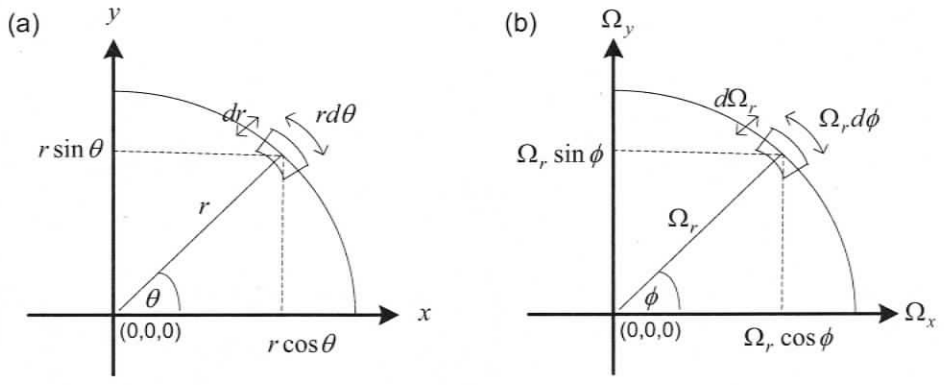

Figure 4-8. The Cartesian to spherical coordinate transformation (a) in the spatial domain (b) in the spatial frequency domain

The transformation in the spatial domain from $(x,y)\in R^2$ to $(r,\theta)\in\left(R^+,[0,2\pi]\right)$ with $dxdy = rdrd\theta$, is as illustrated in Fig.4-8(a) and similarly in the spatial frequency domain from $(\Omega_x,\Omega_y)\in R^2$ to $(\Omega_r,\phi)\in\left(R^+,[0,2\pi]\right)$ with $d\Omega_x d\Omega_y = \Omega_r d\Omega_r d\phi$, as illustrated in Fig.4-8(b). Therefore, (4.9) can be re-written as,

$$W_{C\_MC}(\Omega_x,\Omega_y,\Omega_{ct}) = \int_0^{\infty}\int_0^{2\pi}\int_{-\infty}^{\infty} e^{-ar}\overline{w}(-r+ct)e^{-j(r\Omega_r\cos\theta\cos\phi+r\Omega_r\sin\theta\sin\phi+ct\Omega_{ct})}\,rdrd\theta dct \tag{4.10}$$

$$= \int_0^{\infty}\int_0^{2\pi} e^{-ar}e^{-j(r\Omega_r\cos(\theta-\phi))}e^{-jr\Omega_{ct}}\,rdrd\theta \int_{-\infty}^{\infty}\overline{w}(-r+ct)e^{-j(-r+ct)\Omega_{ct}}\,dct$$

$$= \int_0^{\infty} e^{-ar}e^{-jr\Omega_{ct}}\underbrace{\int_0^{2\pi} e^{-j(r\Omega_r\cos(\theta-\phi))}\,d\theta}_{*}\,rdr\ \underbrace{\int_{-\infty}^{\infty}\overline{w}(-r+ct)e^{-j(-r+ct)\Omega_{ct}}\,dct}_{\overline{W}(\Omega_{ct})} \tag{4.11}$$

Further simplification of the term * in (4.11) requires a closer look at the functional form of the Bessel function of first kind and order-n, which is expressed as,

$$J_n(z) = \frac{1}{2\pi}\int_k^{2\pi+k} e^{j(n\beta-z\sin\beta)}\,d\beta \tag{4.12}$$

By considering $n=0$ and $\beta=(\theta-\phi)-\frac{3\pi}{2}$, (4.12) may be further simplified to,

$$J_0(z) = \frac{1}{2\pi}\int_{k+\phi+\frac{3\pi}{2}}^{2\pi+k+\phi+\frac{3\pi}{2}} e^{-jz\cos(\theta-\phi)}\,d\theta \tag{4.13}$$

Without loss of generality we may take, $k+\phi+\frac{3\pi}{2}=0$ and thus using (4.13) , (4.11) yields,

$$W_{C\_MC}(\Omega_x,\Omega_y,\Omega_{ct}) = \underbrace{\overline{W}(\Omega_{ct})}_{\substack{temporal\\ spectrum}}\ \underbrace{2\pi\int_0^{\infty} e^{-r(j\Omega_{ct}+a)}J_0(\Omega_r r)rdr}_{\substack{spatial\\ spectrum}}\ \text{where}\ \Omega_r=\sqrt{\Omega_x^2+\Omega_y^2} \tag{4.14}$$

The ROS of the $W_{C\_MC}(\Omega_x,\Omega_y,\Omega_{ct})$ can be visualised as the respective 2D spatial magnitude spectrum residing on a plane perpendicular to Ω_{ct} axis depending on the ROS of the temporal component of spectrum $\overline{W}(\Omega_{ct})$. A numerical integration of the spatial spectrum given by (4.14) simulated for $|\Omega_{x,y}|<\frac{2\pi}{3}\times 40 rad/m$, at $\Omega_{ct}=\frac{2\pi}{3}\times 30 rad/m$ and attenuation constant of $a=6.29$ ($\sigma=2dB$, $r_0=0.0366m$) is illustrated in Fig.4-9. Fig.4-9(a) is

a contour plot illustrating the circular symmetric spreading of the spectrum around the spectral light cone, and the corresponding 3D plot is shown in Fig.4-9(b).

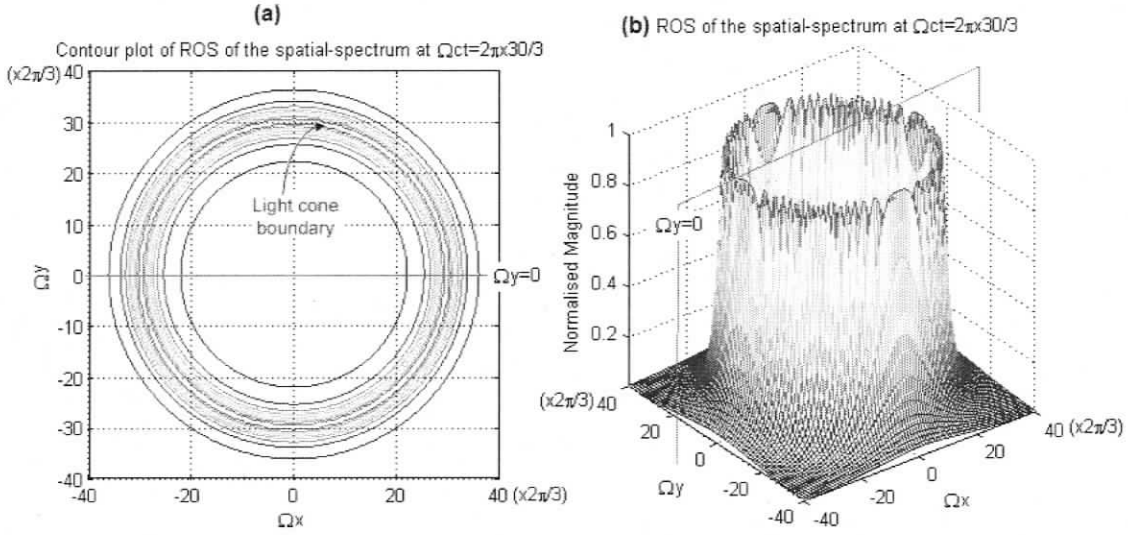

Figure 4-9. A numerical integration of the spatial spectrum in (4.14) simulated for $|\Omega_{x,y}| < \frac{2\pi}{3} \times 40 rad/m$, at $\Omega_{ct} = \frac{2\pi}{3} \times 30 rad/m$ and attenuation constant of $a = 6.29$ ($\sigma = 2dB$, $r_0 = 0.0366m$)

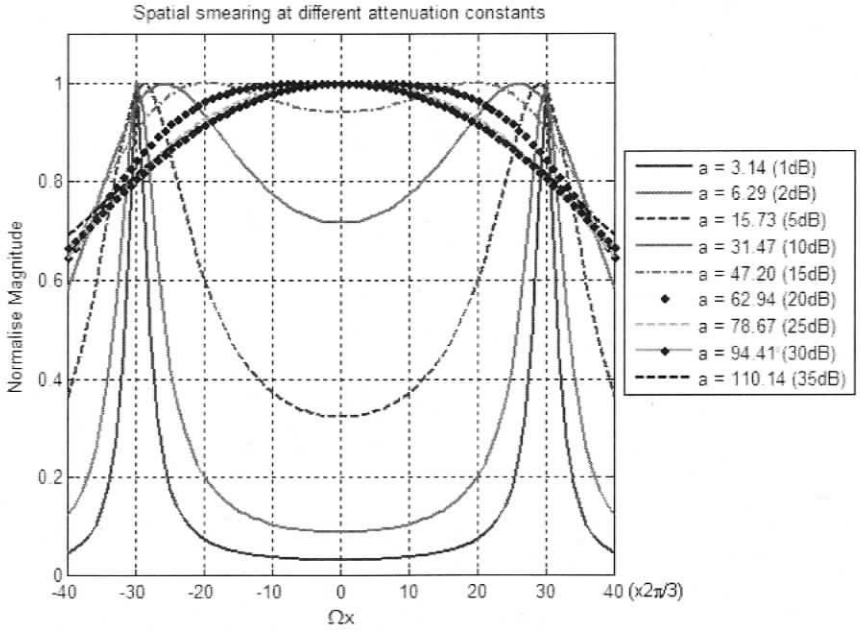

Figure 4-10. Spatial spectral smearing at different spatial attenuations at $r_0 = 0.0366m$, simulated for $|\Omega_x| < \frac{2\pi}{3} \times 40 rad/m$.

The spatial smearing due to different values of attenuation constants are illustrated in Fig.4-10 using slices at $\Omega_y = 0$. As is evident from Fig.4-10, the spatial smearing of the ROS due to the increase of the attenuation constant becomes vital beyond $a = 47.20$ ($\sigma = 15dB$, $r_0 = 0.0366m$) and the spectrum does not have a peak on the spectral light cone boundary. For this reason MC signals with lower a can be significantly suppressed by employing a suitable 3D ST filter that encloses spectral light cone in its stopband and at higher a such filter could only lead to moderate suppression of MC signals.

4.5 MC BB ST Signals Emanating from the Middle Element, in the 3D Discrete ST Domain and Spatio-Temporal Frequency Domain

A MC BB ST signal emanated from the middle element of an uniformly-weighted rectangularly-distributed infinite-extent antenna array is being received by the array as illustrated in Fig.4-11. The received MC BB ST signal $w_{M\_MC}(.)$ can be represented in the mixed domain as,

$$w_{M\_MC}(n_x, n_y, t) = e^{-a\sqrt{n_x T_x + n_y T_y}}\, \overline{w}(-\sqrt{(n_x T_x)^2 + (n_y T_y)^2} + ct) \tag{4.15}$$

where $n_{x,y,} \in \mathbf{Z}^1$, $t \in \mathbf{R}^1$ and $T_{x,y} \in \mathbf{R}^1$ are the spatial sampling intervals (or the inter-antenna distances) of the array.

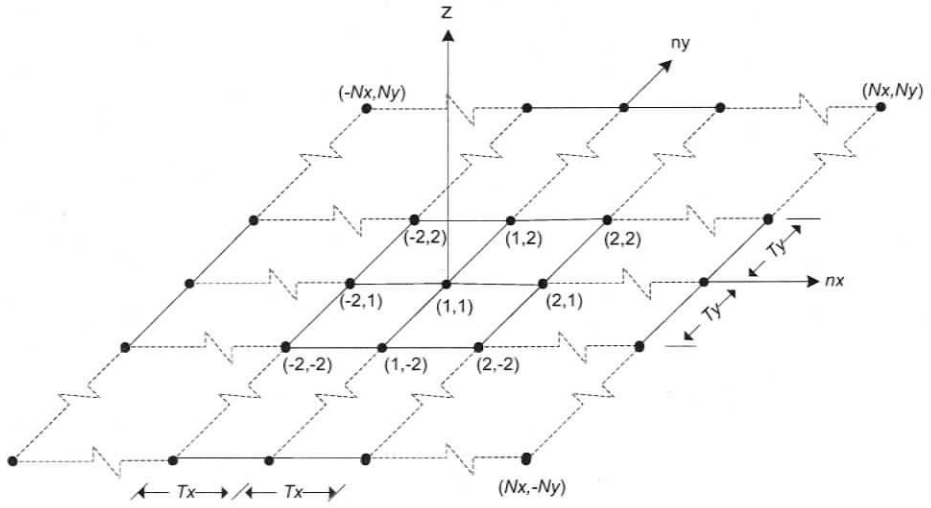

Figure 4-11. $(2N_x + 1) \times (2N_y + 1)$ element rectangularly-distributed uniformly-weighted antenna array with inter antenna distances of $T_{x,y} \in \mathbf{R}^1$

Interested readers may refer to [34] for various other arrangements of antenna elements that are not discussed here, such as circular or hexagonal, in which some of them may also be non-uniformly weighted arrays. Assuming that $w_{M\_MC}(.)$ undergoes an ideal temporal sampling process, the resultant discrete domain MC BB ST signal $w_{D\_MC}(.)$ can be expressed in the form of,

$$w_{D\_MC}(n_x, n_y, n_t) = e^{-a\sqrt{n_x T_x + n_y T_y}}\, \overline{w}(-\sqrt{(n_x T_x)^2 + (n_y T_y)^2} + c n_t T_t) \tag{4.16}$$

where, $n_t \in \mathbf{Z}^1$ and $T_t \in \mathbf{R}^1$ is the temporal sampling interval. For simplicity of analysis in the spatio-temporal frequency domain however, the temporal axis is usually re-scaled by the speed of light c, i.e $f_{ct} = {f_t}/{c}$ and therefore, (4.16) is written in the form,

$$w_{D\_MC}(n_x, n_y, n_{ct}) = e^{-a\sqrt{n_x T_x + n_y T_y}}\, \overline{w}(-\sqrt{(n_x T_x)^2 + (n_y T_y)^2} + n_{ct} T_{ct}) \tag{4.17}$$

Where $n_{ct} \in \mathbf{Z}^1$ and $(T_{ct} = cT_t) \in \mathbf{R}^1$. Thus the discrete domain $w_{D\_MC}(n_x, n_y, n_{ct})$ relates to its 3D Fourier transform $W_{D\_MC}(e^{j\omega_x}, e^{j\omega_y}, e^{j\omega_{ct}})$ by,

$$W_{D\_MC}(e^{j\omega_x}, e^{j\omega_y}, e^{j\omega_{ct}}) = \sum_{-\infty}^{\infty}\sum_{-\infty}^{\infty}\sum_{-\infty}^{\infty} w_{D\_MC}(n_x, n_y, n_{ct}) e^{-j(n_x\omega_x + n_y\omega_y + n_{ct}\omega_{ct})} \tag{4.18}$$

whereas the periodicity of $W_{D\_MC}(.)$ is related to $W_{C\_MC}(.)$ given by,

$$W_{D\_MC}(e^{j\omega_x}, e^{j\omega_y}, e^{j\omega_{ct}}) = \frac{1}{T_x T_y T_{ct}} \sum_{-\infty}^{\infty}\sum_{-\infty}^{\infty}\sum_{-\infty}^{\infty} W_{C\_MC}\left(j\frac{\omega_x - 2\pi k_x}{T_x}, j\frac{\omega_y - 2\pi k_y}{T_y}, j\frac{\omega_{ct} - 2\pi k_{ct}}{T_{ct}} \right) \tag{4.19}$$

where $\omega_{x,y,ct}$ are the normalised version of $\Omega_{x,y,ct}$ associated as,

$$\Omega_i = \frac{\omega_i}{T_i}, \quad i = x, y, ct \tag{4.20}$$

The relationship of (4.20) to (4.19), implies that the normalised version of $W_{C\_MC}(.)$ is repeated at intervals of 2π in all three dimensions to form the spectrum of $W_{D\_MC}(.)$. Given that $\overline{w}(.)$ is a temporally band-limited signal, then, there exist f_s such that $\frac{f_s}{2} \geq \max\{f_x, f_y, f_{ct}\}$ where $f_{x,y}$ are the spatial frequencies[6]. Hence, it is possible to find the required spatio-temporal sampling periods that satisfy the Nyquist condition given by,

---

[6] Wave number $k_{x,y}$ is related to the spatial frequency $f_{x,y}$, by $k_{x,y} = 2\pi f_{x,y}$ where $f_{x,y} = \frac{1}{\lambda_{x,y}} = \frac{f_t}{c}$, c is the speed of light and f_t is the temporal frequency of the propagating wave.

$$T_x \le \frac{1}{2\max\{f_x\}}, T_y \le \frac{1}{2\max\{f_y\}} \text{ and } T_{ct} \le \frac{1}{2\max\{f_{ct}\}} \tag{4.21}$$

Employing suitable sampling periods that satisfy the conditions in (4.21), leads to a simpler form of (4.19) in the fundamental Nyquist box $|\omega_{x,y,ct}| \le \pi$ given by,

$$W_{D\_MC}(e^{j\omega_x}, e^{j\omega_y}, e^{j\omega_{ct}}) = \frac{1}{T_x T_y T_{ct}} W_{C\_MC}\left(j\frac{\omega_x}{T_x}, j\frac{\omega_y}{T_y}, j\frac{\omega_{ct}}{T_{ct}}\right) \tag{4.22}$$

where $|\omega_{x,y,ct}| \le \pi$. This implies that $W_{D\_MC}(.)$ completely encloses the spectral information of $W_{C\_MC}(.)$ in the fundamental Nyquist box $|\omega_{x,y,ct}| \le \pi$.

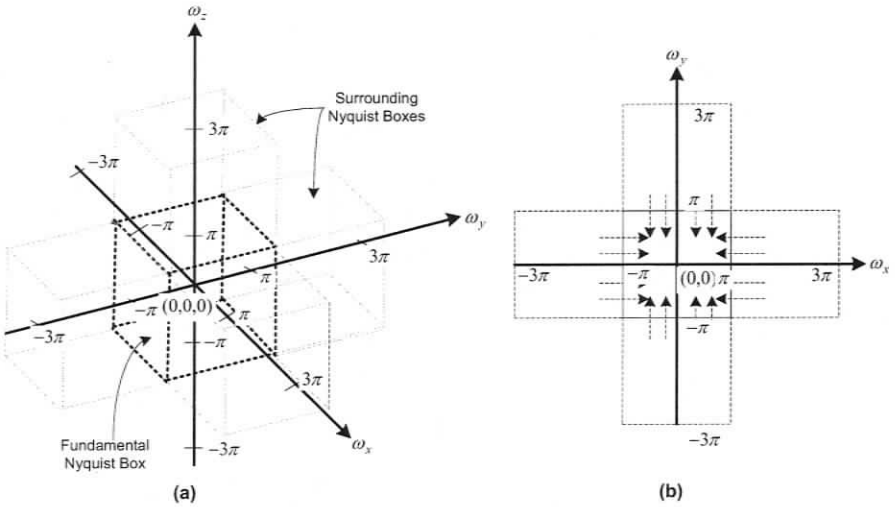

Figure 4-12. Illustration of (a) fundamental Nyquist box (b) directions of possible spatial aliasing, in the discrete-time 3D spatio-temporal frequency domain

In the case where temporal sampling periods violate the Nyquist condition the spectrum of $W_{C\_MC}(.)$ normalised to f_s in each of the Nyquist boxes $(2n-1)\pi \le \omega_{x,y,ct} \le (2n+1)\pi$ will extend to surrounding Nyquist boxes along the temporal frequency axis. This phenomenon is called temporal aliasing. Similarly, at the violation of the spatial Nyquist condition, spatial aliasing will occur. Therefore, it is mandatory that spatio-temporal sampling periods $T_{x,y,ct} \in \mathbf{R}^1$ are selected in accordance with the Nyquist sampling condition as mentioned in (4.21), in order to avoid any spatial and temporal aliasing.

Antenna arrays are limited by the number of spatial samples while it is possible to extract large (can be considered infinite) number of temporal samples; therefore, (4.17) undergoes a spatial windowing process thus the resultant windowed discrete domain BB MC ST signal $w_{W\_D\_MC}(.)$ can be represented as,

$$w_{W\_D\_MC}(n_x, n_y, n_{ct}) = e^{-a\sqrt{n_x T_x + n_y T_y}}\, \overline{w}(-\sqrt{(n_x T_x)^2 + (n_y T_y)^2} + n_{ct} T_{ct}) rec_{D\_3D}(n_x, n_y) \tag{4.23}$$

where,

$$rec_{D\_3D}(n_x, n_y) = \begin{cases} 1 & |n_x| \le N_x, |n_y| \le N_y \\ 0 & elesewhere \end{cases} \tag{4.24}$$

for which $N_{x,y} \in \mathbf{Z}^1$ at an array of size $(2N_x + 1) \times (2N_y + 1)$. The corresponding 3D frequency domain representation of $w_{W\_D\_MC}(.)$ is therefore derived as,

$$W_{W\_D\_MC}(\omega_x, \omega_y, \omega_{ct}) = W_{D\_MC}(\omega_x, \omega_y, \omega_{ct}) *** REC_{D\_3D}(\omega_x, \omega_y)\delta(\omega_{ct}) \tag{4.25}$$

where $W_{W\_D\_MC}(\omega_x, \omega_y, \omega_{ct}) \underset{DFT}{\overset{IDFT}{\Leftrightarrow}} w_{W\_D\_MC}(n_x, n_y, n_{ct})$ and $REC_{D\_3D}(\omega_x, \omega_y) \underset{DFT}{\overset{IDFT}{\Leftrightarrow}} rec_{D\_3D}(n_x, n_y)$ which is given by,

$$REC_{D\_3D}(\omega_x, \omega_y) = \frac{\sin\left(\omega_x \dfrac{(N_x + 1)}{2}\right) \sin\left(\omega_y \dfrac{(N_y + 1)}{2}\right)}{\sin\left(\dfrac{\omega_x}{2}\right) \sin\left(\dfrac{\omega_y}{2}\right)} \tag{4.26}$$

The spectral broadening and leakage caused by (4.26) in the 3D spatio-temporal frequency domain is the finite aperture effect discussed in Chapter-3, Section 3.4.2.

4.6 A Numerical Simulation Analysis of MC Photonically Reflected BB ST SOI/RFI Signals Emanating from the Middle Element in the 3D Discrete ST and Frequency Domains

Consider a hypothetical $(2N_x + 1) \times (2N_y + 1) = 81 \times 81$ element rectangularly-distributed uniformly-weighted broadband antenna array which has an operational bandwidth of 0.05-4GHz. The temporal variation $\overline{w}(.)$ of the band-limited BB ST SOI/RFI which is photonically reflected at the antenna element resulting in a BB MC signal, is synthesised by superimposing equi-amplitude cosine functions in the form of,

$$\overline{w}(.) = \sum_{k=1}^{k_{MAX}} \cos[2\pi f_k(.)] \quad ..\mathbf{f} = [f_1, f_2 .... f_{k_{MAX}}] \tag{4.27}$$

where $f_{k_{MAX}} = 4GHz$ is the maximum frequency with $\mathbf{f} = [0.05,0.1,0.15...4]GHz$. Assuming that the speed of light is $c = 0.3Gm/s$, the corresponding slightly over-sampled spatio-temporal sampling distances are chosen to be, $T_{x,y,ct} = T_s = \frac{1}{f_s} == 0.0366m$.

The space-time representation of the synthesised broadband signal (in Fig.3-8) emanating from the middle element of a 81×81 array, i.e a MC BB ST signal, which propagates at a spatial attenuation of $a = 6.29\,(\sigma = 2dB, r_0 = T_s = 0.0366m)$ is illustrated in Fig.4-13. The spatial attenuation used here may be small compared to experimentally reported attenuation values; however, it is useful to explain the behaviour of its ROS in the frequency domain. The cone shape in Fig.4-13 (a) contains 90% of the total energy of the signal which corresponds to the ST propagation of the signal peak at $n_{ct} = 0$ in Fig.3-8. The smaller ripples of the broadband signal in Fig.3-8 are not visible. Two contour plots of the slices at $n_{ct} = 10$ and $n_y = 0$ are shown in Fig.4-13.(b) and Fig.4-13.(c) respectively. Fig.4-13.(b), can be considered as a snap-shot of a birds-eye view of the antenna array at time $n_{ct} = 10$.

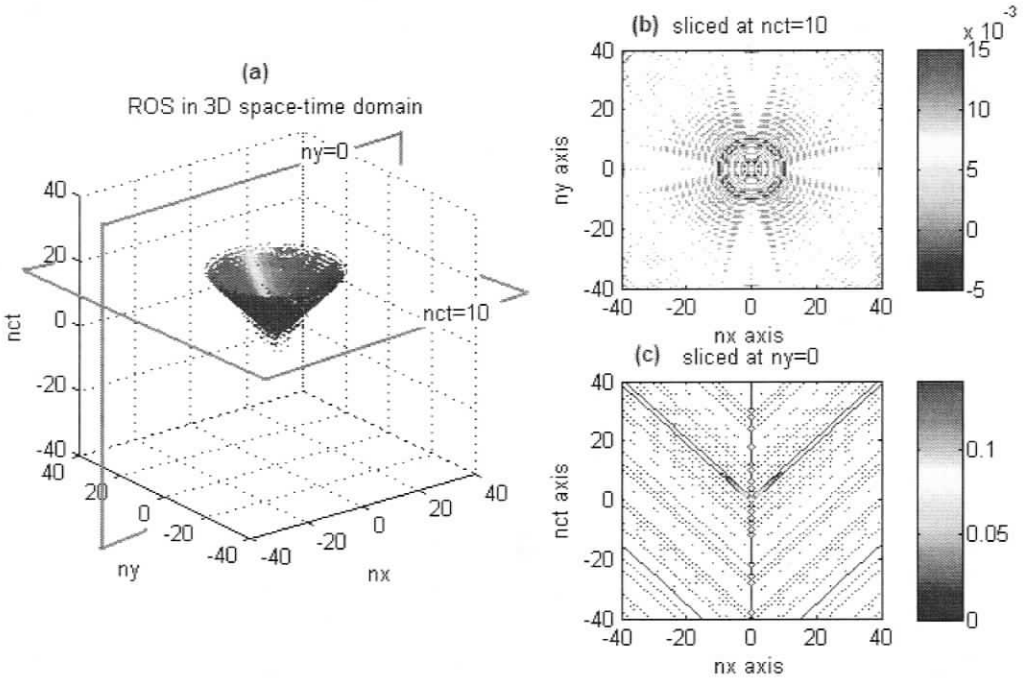

Figure 4-13. 3D space-time representation of BB MC ST signal emanating from the middle element with an attenuation constant of $a = 6.29\,(\sigma = 2dB, r_0 = T_s = 0.0366m)$ (a) the 3D ROS that contains 90.0% of the signal energy (b) a 2D contour plot sliced at $n_{ct} = 10$ (c) a 2D contour plot sliced at $n_y = 0$

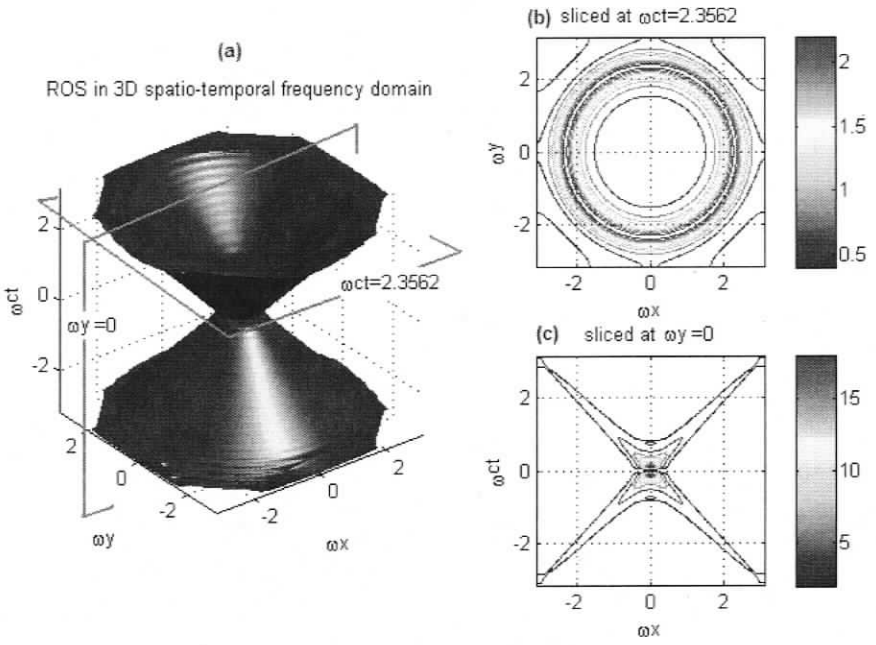

Figure 4-14. 3D spatio-temporal frequency domain representation of BB MC ST signal emanating from the middle element propagating with an attenuation constant of $a = 6.29$ ($\sigma = 2dB$, $r_0 = T_s = 0.0366m$) (a) the 3D ROS that contains 87.2% of the signal energy (b) a 2D contour plot sliced at $\omega_{ct} = 2.3562$ (c) a 2D contour plot sliced at $\omega_y = 0$

A series of observations of Fig.4-13.(b) at different n_{ct}'s can be best explained as observing the outward moving rings of a water surface due to a disturbance in the middle. The spatial attenuation of such rings is clearly illustrated in Fig.4-13.(c) as 'V' shapes, where the edge of the 'V' is faded along spatial dimension n_x.

The BB MC ST signal illustrated in Fig.4-13 has the corresponding ROS in the 3D spatio-temporal frequency domain as illustrated in Fig.4-14. Confirming the observations in the continuous frequency domain illustrated in Fig.4-10, the circular contour plot in Fig.4-14(b), at a slice $\omega_{ct} = 2.3562$, also verifies that the ROS of the BB MC signal at attenuation constant of $a = 6.29$ ($\sigma = 2dB$, $r_0 = T_s = 0.0366m$) confines to and around the spectral light cone boundary. The middle thick circle of Fig.4-14(b) is exactly on the spectral light cone and this is also evident from the 45 degree 'X' shape, observed at a slice $\omega_y = 0$ illustrated in Fig.4-14(c). A 3D visualisation of the ROS is illustrated in Fig.4-14(a) and can be best explained as a spatially smeared spectral light cone. The amount of thickness of the cone illustrated in Fig.4-14(a) is dependent on the attenuation constant a as explained in Fig.4-10. The spatial smearing increases as a increases, and at

higher values of a the smearing leads to spatial leakage towards subsequent Nyquist boxes causing spatial aliasing as illustrated in Fig.4-15. Fig.4-15, is a comparison of spatial smearing simulated at different attenuation constants a. It is very clear that as a increases, the ROS no longer confine to and around the spectral light cone and, therefore, at very high attenuations the spatial smearing increases introducing spatial aliasing. The reason for spatial aliasing in this case is spectral broadening in the spatial frequency violating (4.21) such that,

$$T_{x,y} > \frac{1}{2\max\left\{f_{x,y}^{smeared}\right\}} \tag{4.28}$$

where $f_{x,y}^{smeared}$ are smeared spatial frequencies. The Nyquist condition could be violated as a result of not selecting sufficiently small sampling intervals. Consider a case,

$$T_{ct}^{new} > \frac{1}{2\max\left\{f_{ct}\right\}} \tag{4.29}$$

where $T_{ct}^{new} > T_{ct}$.

Fig.4-16 illustrates a temporal aliasing example where the new temporal sampling interval is chosen to be $T_{ct}^{new} = 0.0549m$, which is 50% less than in the example illustrated in Fig.4-14. Due to the violation of the Nyquist condition in the temporal dimension, the aliasing appears along ω_{ct} and is clearly visible in Fig.4-16(c), which is a slice taken at $\omega_y = 0$. Fig.4-16(a) can be best explained as the cone shaped ROS observed in Fig.4-14(a) being elongated along ω_{ct} and being reflected at $|\omega_{ct}| = \pi$ planes inside the Nyquist cube. The actual source of reflections is the spectral leakages from subsequent Nyquist boxes along ω_{ct}.

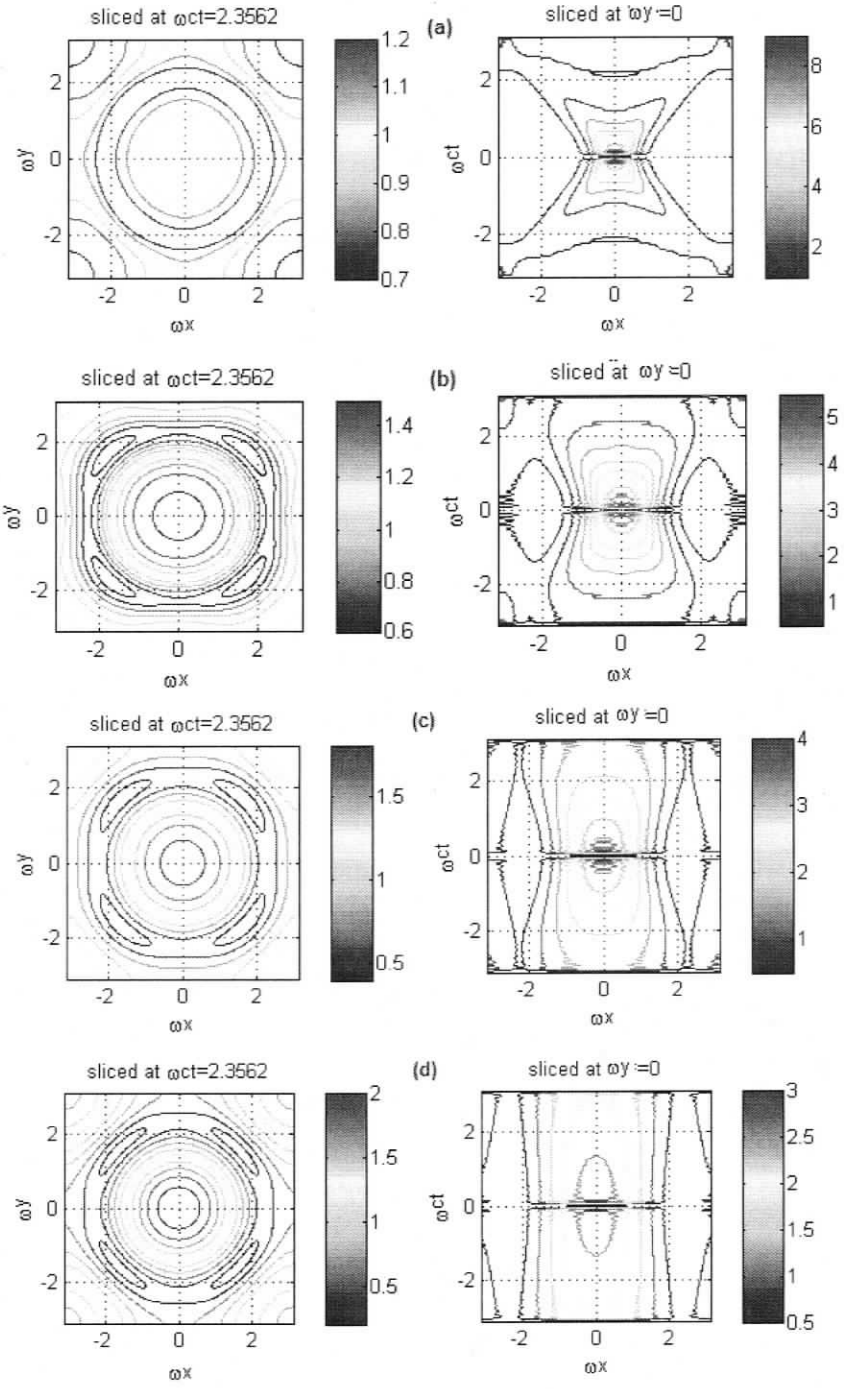

Figure 4-15. 2D contour plots sliced at $\omega_{ct} = 2.3562$ and $\omega_y = 0$ in the 3D spatio-temporal frequency domain of BB MC ST signal emanating from the middle element propagating with an attenuation constants: (a) $a = 15.73$ ($\sigma = 5dB$, $r_0 = T_s = 0.0366m$) (b) $a = 31.47$ ($\sigma = 10dB$, $r_0 = T_s = 0.0366m$) (c) $a = 47.20$ ($\sigma = 15dB$, $r_0 = T_s = 0.0366m$) (d) $a = 62.94$ ($\sigma = 20dB$, $r_0 = T_s = 0.0366m$)

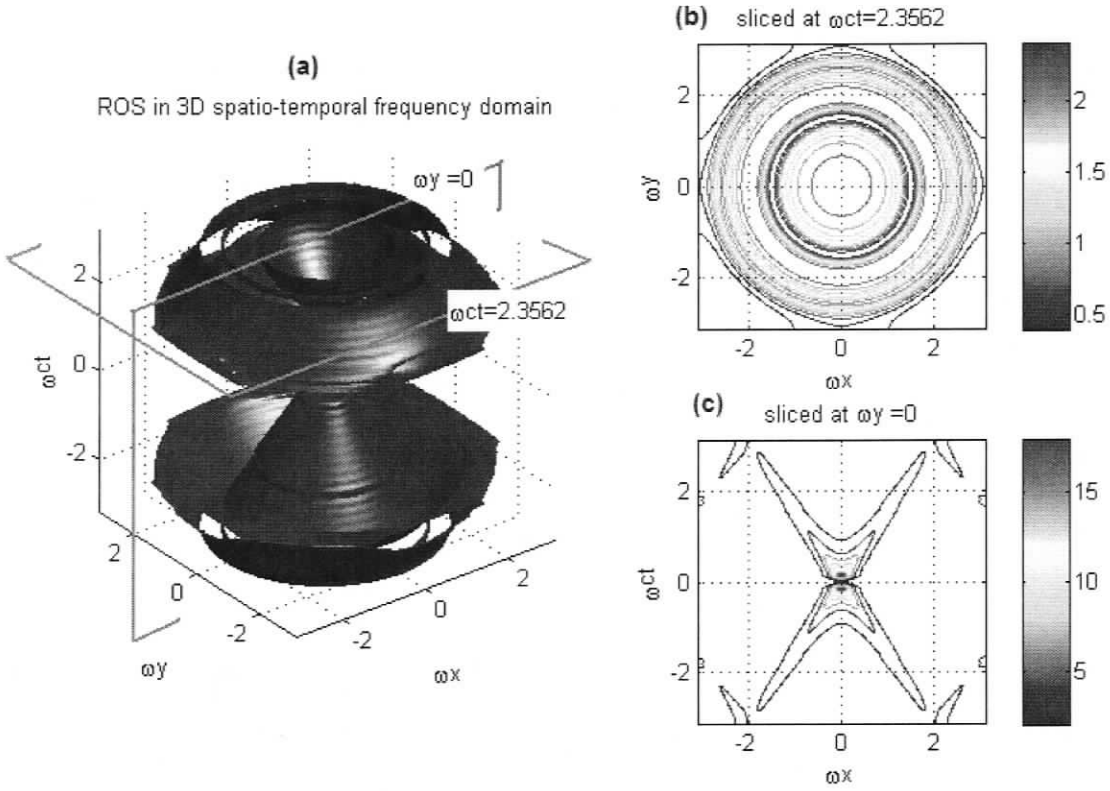

Figure 4-16. 3D spatio-temporal frequency domain representation of BB MC ST temporally under-sampled signal ($T_{x,y} = 0.0366m$ and $T_{ct}^{new} = 0.0549m$) emanating from the middle element propagating with an attenuation constant of $a = 6.29$ ($\sigma = 2dB$, $r_0 = 0.0366m$) (a) the 3D ROS that contains 91.2% of the signal energy (b) a 2D contour plot sliced at $\omega_{ct} = 2.3562$ (c) a 2D contour plot sliced at $\omega_y = 0$.

The finite aperture effect due to the finite array size is illustrated in Fig.4-17. The slices taken at $\omega_{ct} = 2.3562$ for array sizes of $(2N_x + 1) \times (2N_y + 1) = 61 \times 61$, $(2N_x + 1) \times (2N_y + 1) = 41 \times 41$ and $(2N_x + 1) \times (2N_y + 1) = 11 \times 11$ is shown in the left column of Fig.4-17 (a), (b) and (c) respectively. It is clearly evident from the figures that the finite aperture effect is dominant at lower array sizes and should be taken in to consideration at lower inter-antenna attenuations to define the required stopband angle of the 3D ST filter.

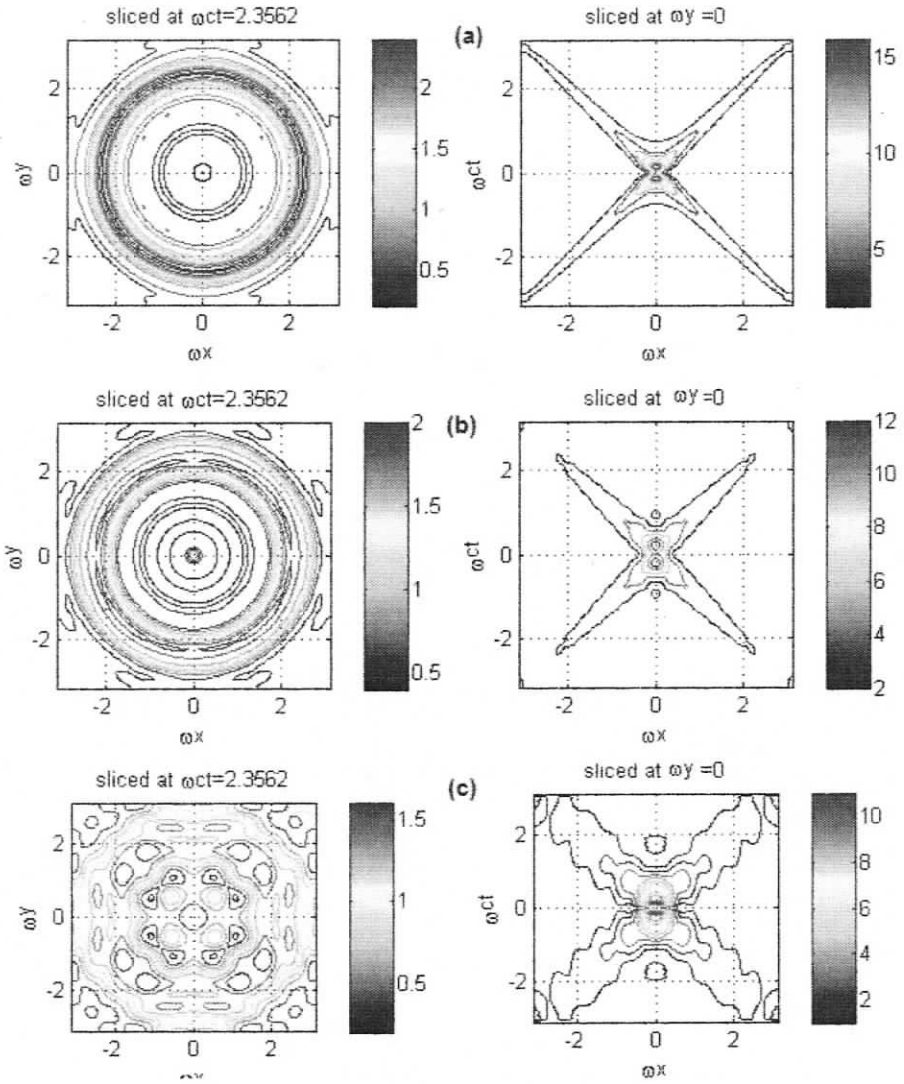

Figure 4-17 The finite aperture effect: 2D contour plots sliced at $\omega_{ct} = 2.3562$ and $\omega_y = 0$ of the 3D spatio-temporal frequency domain of BB MC ST signal emanating from the middle element of an arrays (a) $(2N_x+1)\times(2N_y+1) = 61\times 61$ (b) $(2N_x+1)\times(2N_y+1) = 41\times 41$, (b) $(2N_x+1)\times(2N_y+1) = 11\times 11$ propagating with an attenuation constant $a = 6.29$ ($\sigma = 2dB$, $r_0 = T_s = 0.0366m$)

4.7 BB Mutually Coupled (MC) LNA Noise

One of the main objectives of the LNA is to amplify the SOI which are very weak signals that fall in to the power range of -100dBm [9]. Furthermore, since sensitivity of the LNA governs the overall receiver sensitivity according to the Friis Formula [34], it is

also required that minimal internal noise be emitted from the LNA towards other LNAs in the array. Among different internal sources of noise in the LNA, the dominant sources can be categorised as Shot noise, Flicker noise and Thermal noise. Shot noise is a type of a white noise associated with the particulate nature of electrons which is usually observed in transistors and operational amplifiers. Flicker noise is associated with combination-recombination of carriers in the emitter base area of a transistor that are caused by contamination and defects in the silicon lattice structure. This is also called 1/f noise because the amplitude of the noise increases as the frequency decreases. Thermal noise is caused by the random motion of charges due to the thermal energy absorbed from the surroundings. In the following analysis, it is assumed that thermal and shot noise are dominant and therefore LNA noise is synthesised by a white noise model.

4.8 A Numerical Simulation Analysis of BB MC LNA Noise Emanating From the Middle Element in the 3D Discrete ST Domain and in Frequency Domain

The temporal variation $\overline{w}(.)$ of the band-limited MC LNA signal is synthesised as in (4.30) by convolving a FIR bandpass filter with Gaussian white noise with mean $\overline{m}$ and standard deviation σ generated by a stochastic process.

$$\overline{w}(.) = N_{GWN,\overline{m},\sigma}(.) * h_{FIR,BW}(.) \tag{4.30}$$

Consider a hypothetical $(2N_x+1)\times(2N_y+1) = 81\times 81$ element rectangularly-distributed uniformly-weighted broadband antenna array which has an operational bandwidth of 0.05-4GHz. Given that the array is band-limited, the bandwidth of the filter is chosen to be 0.05-4GHz. Assuming that the speed of light is $c = 0.3Gm/s$ the corresponding slightly over-sampled spatio-temporal sampling distances are chosen to be, $T_{x,y,ct} = T_s = \frac{1}{f_s} == 0.0366m$ such that $\frac{f_s}{2} = \frac{4.1GHz}{3Gm/s}$. The temporal variation and the magnitude spectrum of the synthesised LNA Noise are shown in Fig.4-18.

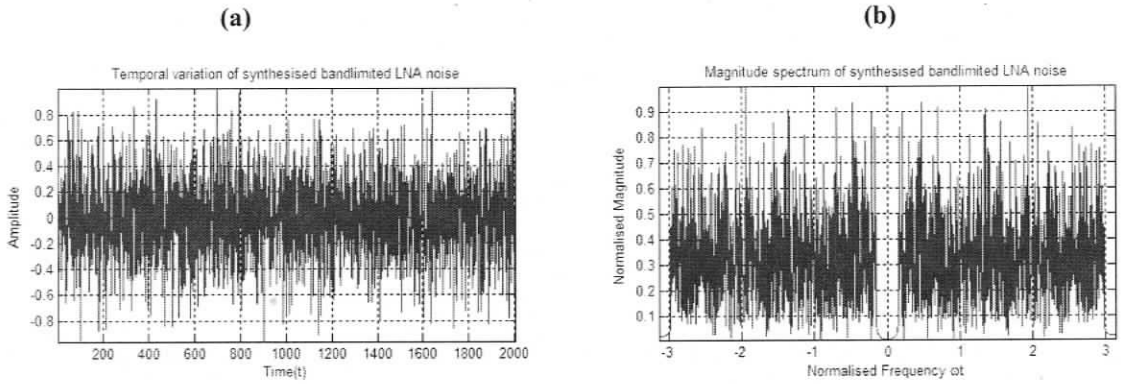

Figure 4-18. (a) the temporal variation (b) the magnitude spectrum; of the synthesised LNA Noise using bandlimited (0.05-4)GHz white Gaussian noise of $\overline{m}=0$ and $\sigma=0.5$ as in (4.30)

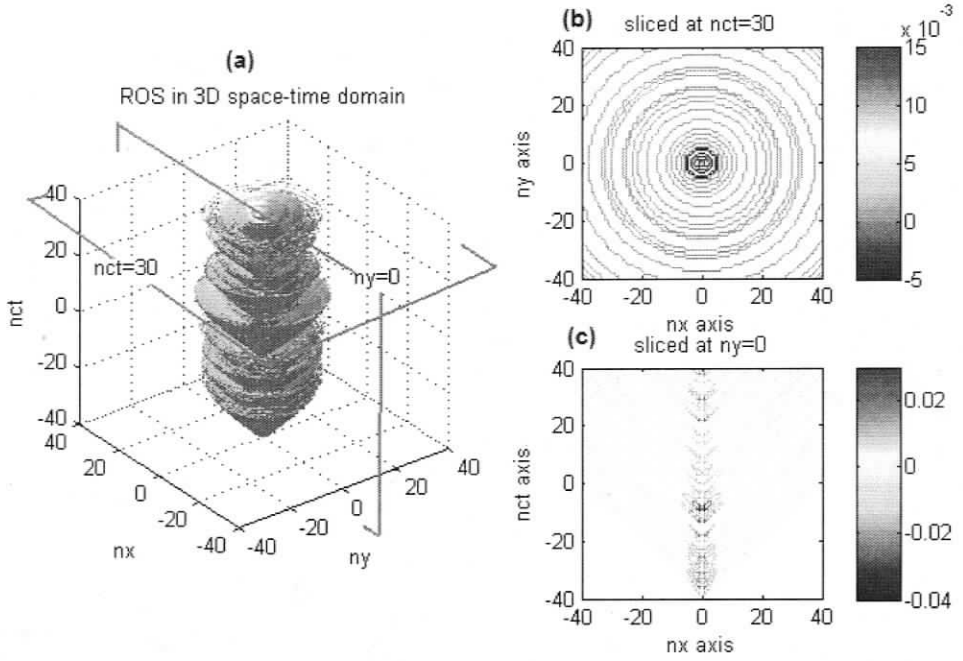

Figure 4-19. 3D space-time representation of BB MC LNA noise emanating from the middle element with an attenuation constant of $a=6.29\,(\sigma=2dB\,,r_0=T_s=0.0366m)$ (a) the 3D ROS that contains 47.32% of the signal energy (b) a 2D contour plot sliced at $n_{ct}=10$ (c) a 2D contour plot sliced at $n_y=0$

The space-time representation of the synthesised BB MC LNA noise signal emanating from the middle element of a 81×81 array which propagates at a spatial attenuation of $a=6.29\,(\sigma=2dB\,,r_0=T_s=0.0366m)$ is illustrated in Fig.4-19. The corresponding ROS in

the 3D spatio-temporal frequency domain of the synthesised BB MC LNA noise is illustrated in Fig.4-20. The properties of the ROS of BB MC photonically reflected signals discussed in sub-section 4.6 remain valid for BB MC LNA noise signals as well.

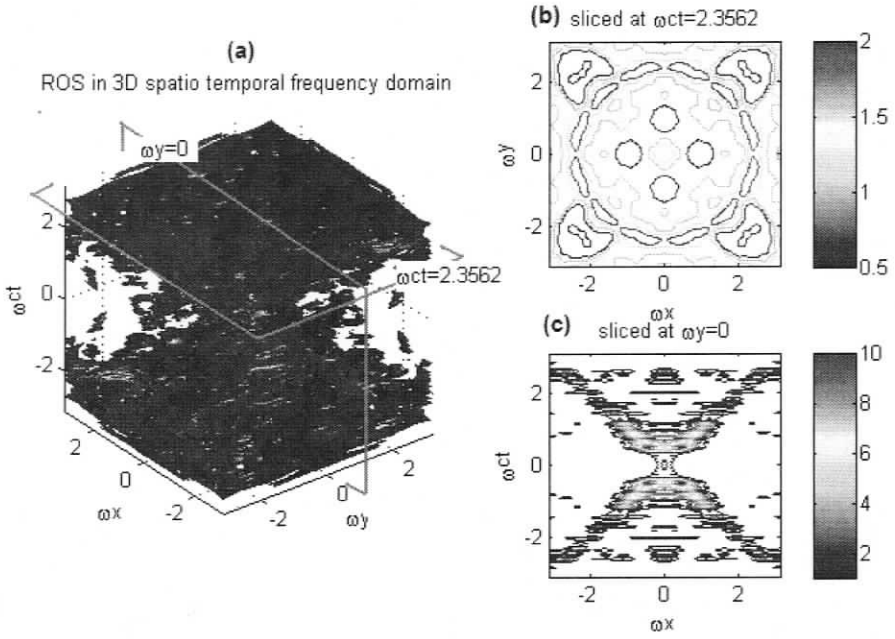

Figure 4-20. spatio-temporal frequency domain representation of BB MC LNA noise emanating from the middle element propagating with an attenuation constant of $a = 6.29$ ($\sigma = 2dB$, $r_0 = T_s = 0.0366m$) (a) the 3D ROS that contains 88.72% of the signal energy (b) a 2D contour plot sliced at $\omega_{ct} = 2.3562$ (c) a 2D contour plot sliced at $\omega_y = 0$

Fig.4-21, is a comparison of spatial smearing simulated at different attenuation constants a. Similar to Fig.4-15, it is clear that as a increases, the ROS of BB MC LNA noise in the 3D spatio-temporal domain is no longer confined to and around the spectral light cone. At higher attenuations the spatial smearing increases and introduces spatial aliasing.

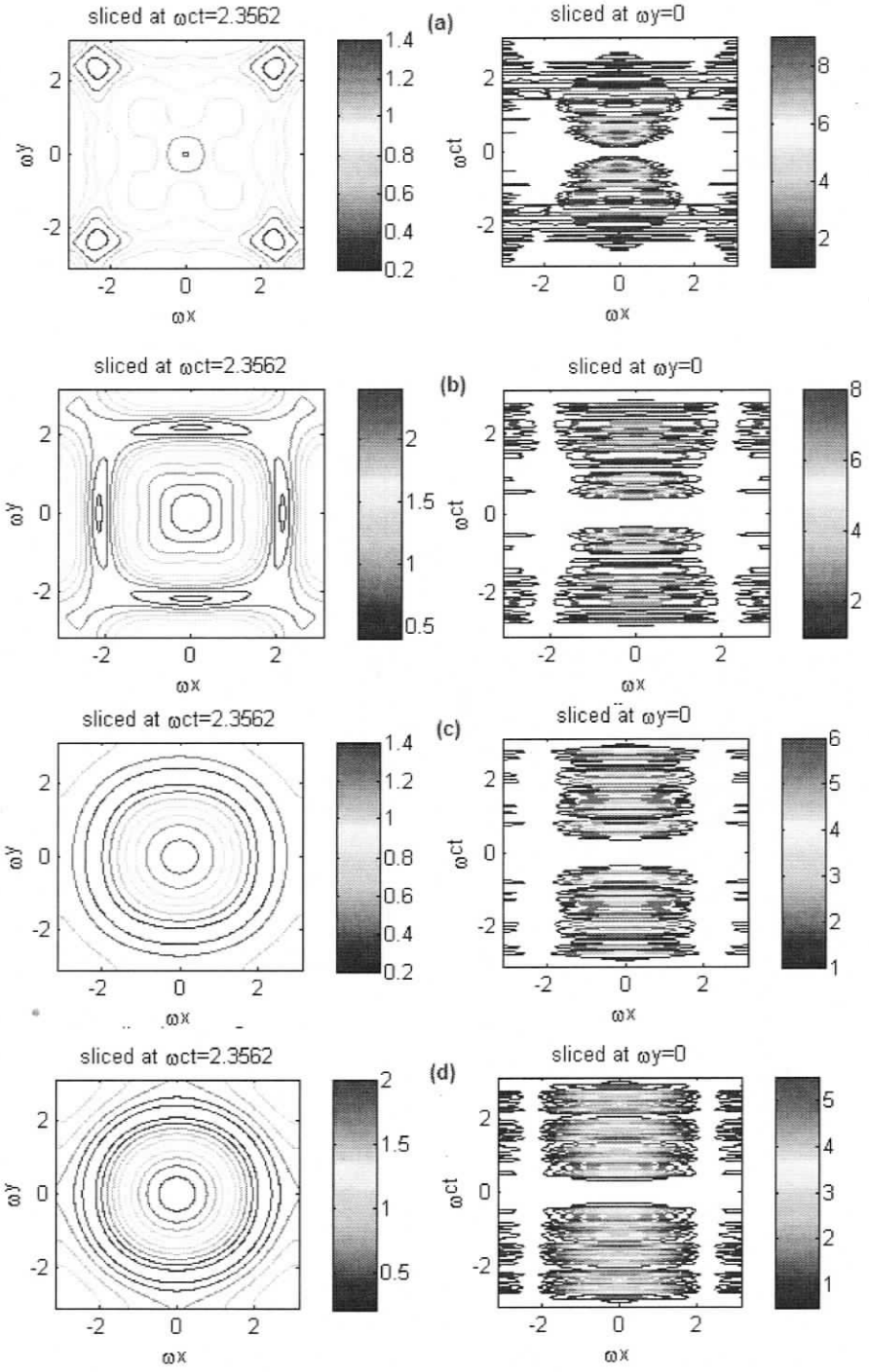

Figure 4-21. Slices of the 3D spatio-temporal frequency domain representation of MC LNA Noise emanating from the middle element propagating at inter-antenna attenuation (a)5dB (b)10dB (c)15dB (d)20dB

4.9 A Brief Overview of BB MC ST Signals/LNA Noise Coupling Emanated from all Array Elements

So far, the analysis of BB MC ST signals has been discussed based on a model of MC signal being emanated from the middle element. In practical applications however, the MC signals are emanated from all array elements and therefore it is important to discuss the ROS of the composite BB MC signals in the 3D spatio-temporal frequency domain. Assuming that BB MC ST signals are additive and the origin of the signals from antenna sources is asynchronous, the respective ROS of the composite signal in 3D spatio-temporal frequency domain display characteristics similar to that of the middle antenna element. However, depending on the location of MC signals emanation in the array, the energy contribution to the composite MC signal of the array may differ. To observe this effect, consider a mutual coupling emanation occurring in an element located at the edge of an array $(n_x, n_y) = (0, 40)$ using the same synthetic BB MC signal discussed in sub-section 4.6, (4.27).

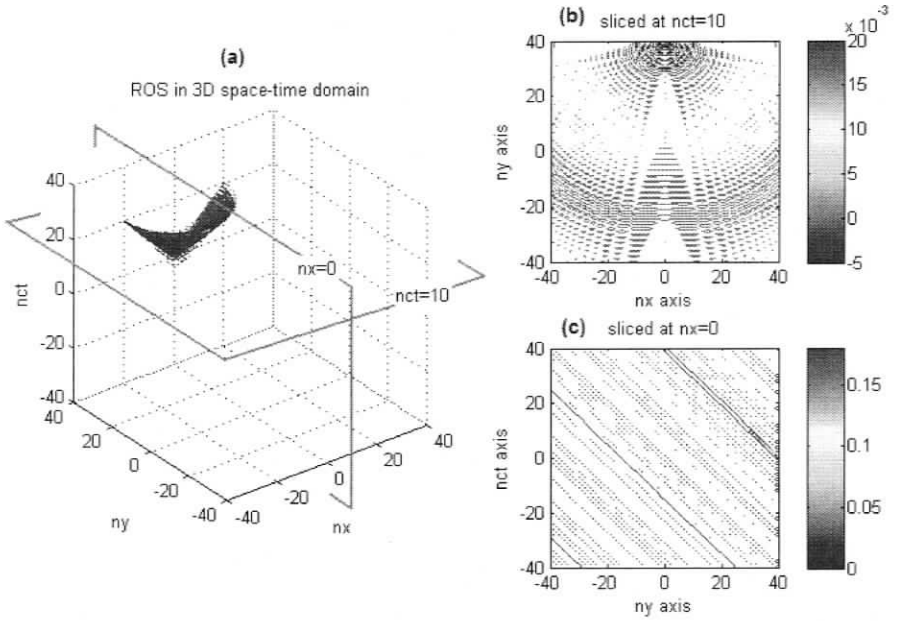

Figure 4-22. 3D space-time representation of BB MC ST signal emanating from $(n_x, n_y) = (0,40)$ element with an attenuation constant of $a = 6.29$ ($\sigma = 2dB$, $r_0 = T_s = 0.0366m$) (a) the 3D ROS that contains 91.5% of the signal energy (b) a 2D contour plot sliced at $n_{ct} = 10$ (c) a 2D contour plot sliced at $n_y = 0$

The space-time representation of the synthesised BB MC signal being emanated from the $(n_x, n_y) = (0,40)$ element of a 81×81 array which propagates at a spatial attenuation of $a = 6.29$ ($\sigma = 2dB$, $r_0 = T_s = 0.0366m$) is illustrated in Fig.4-22. The corresponding ROS in the 3D spatio-temporal frequency domain is illustrated in Fig.4-23, and it can be seen that it is similar to the ROS of the mutual coupling signal emanated from the middle element $(n_x, n_y) = (0,0)$. Compared to the energy contributed to the ROS of the composite signal, the emanation from the $(n_x, n_y) = (0,40)$ element contributes approximately 50% of spectral energy contributed by the signal emanating from the middle element.

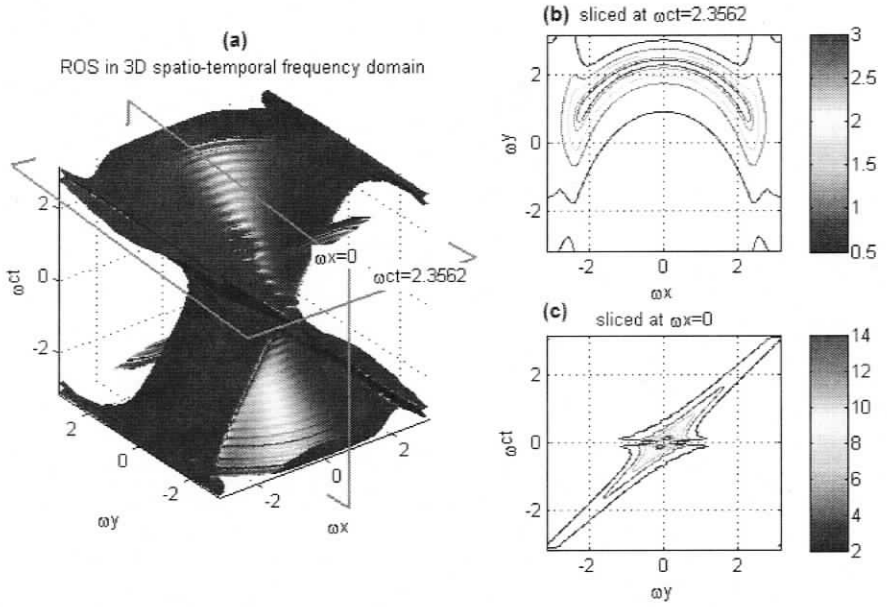

Figure 4-23. 3D spatio-temporal frequency domain representation of BB MC ST signal emanating from $(n_x, n_y) = (0,40)$ element propagating with an attenuation constant of $a = 6.29$ ($\sigma = 2dB$, $r_0 = T_s = 0.0366m$) (a) the 3D ROS that contains 89.02% of the signal energy (b) a 2D contour plot sliced at $\omega_{ct} = 2.3562$ (c) a 2D contour plot sliced at $\omega_y = 0$

4.10 Summary

In this chapter a novel ST propagation model has been investigated to represent mutually coupled (MC) ST signals that exist on dense broadband (BB) antenna arrays. For this purpose, a simplistic ST theoretical model that has a circularly symmetric propagation with an exponential damping in spatial dimensions has been derived. To

investigate the validity of the proposed theoretical model the scattering parameter data measured from a BB Vivaldi antenna array of DRAO, Canada has been examined. Satisfactory evidence is shown in sub-section 4.3, that the simplistic circularly symmetric propagation model is reasonable to approximate the propagation of MC signals of certain frequency bands on the 180-element Vivaldi array. The spatial inter-antenna attenuation of the array has been observed to be approximately between 15-20dB.

A theoretical study on the spectral characteristics of BB ST MC signals is then presented, followed by a numerical simulation analysis in the 3D space-time and spatio-temporal frequency domains. In this analysis, two possible MC signal categories, namely photonically reflected incident waves and internally generated LNA noise waves were considered. Without loss of generality the analysis was carried out for the case of emanation from the middle element. The spectral analysis of BB MC signals indicated that at lower spatial attenuation constants MC signals have their ROS of the spectrum in the 3D spatio-temporal frequency domain confined to and around the spectral light cone. At higher spatial attenuations, such as inter-antenna attenuation of 15dB corresponding to the analysed Vivaldi array, the ROS smeared along spatial frequency plane in the complete Nyquist cube.

Assuming that MC signals are additive and the origin of the signals from antenna sources is asynchronous, the respective ROS in 3D spatio-temporal frequency domain of the composite MC signal emanating from all array elements, will display similar characteristics to that of the middle antenna element.

Based on the analysis of ROSs of MC signals in the 3D spatio-temporal frequency domain at various attenuation constants, it is evident that a suitable ST filter enclosing the spectral light cone in its stopband can be employed to suppress BB MC signals. For MC signals with lower a the suppression will be significant whereas at higher a such filter could only lead to a moderate suppression.

Chapter 5

3D Space-Time Cone Filter Design

In this chapter, an ST digital filter is proposed to approximate the required cone shaped passband to filter ST BB signals discussed in Chapters 3 and 4. Two previously reported analytic FIR and IIR 3D ST cone filters are analysed and simulated to investigate their properties. A novel FIR cone filter approximation is introduced to satisfy the design requirements of BB ST signals involved in radio-astronomical applications. Finally, synthetic BB signals are used to analyse and compare the performance of the proposed ST FIR filter with the other two techniques to demonstrate the superior performance of the proposed filter.

5.1 Introduction

The previously reported publications [4] [5] [7] [6] [8] [48] on 3D ST filter designs have aimed at developing closed form analytical methods that can be used to selectively enhance/suppress ST-PWs based on their DOAs. These earlier studies have addressed the need for design methods that can adaptively approximate the desired 3D passband shapes within the complete 3D Nyquist box. In the context of radio astronomy however, especially for the filtering of signals analysed in Chapters 3 and 4, an adaptive ST filter with a cone-shaped passband enclosing the temporal frequency axis may be sufficient. Furthermore, in order to effectively suppress the disturbing signals, such as BB MC signals and BB RFIs, the approximation of the passband of the 3D ST cone filter requires a circularly symmetric cross section with a steep passband to stopband transition. In addition, to avoid any perturbations being introduced to the phase information of the SOI (as it is essential for the subsequent beamforming and signal processing operations), the phase of the filter must also be linear. To address these concerns a novel 3D ST filter bank structure comprised of 2D zero-phase circularly symmetric FIR filters and 1D linear phase bandpass FIR filters, is being introduced. The closed-form analytical structure of the proposed filter bank further allows us to easily define the required cone passband

angle in comparison to previously reported fixed-DOA 3D ST non-analytical cone filter design methods based on optimisation techniques [49] [50] and spectral transformation techniques (ex. McLellan transformation) etc. [51].

5.2 Background of 3D ST Filtering

The objective of 3D ST filtering is to separate the desired signal from noise, interference, or any other signals [2]. In 3D spatio-temporal frequency domain, this can be regarded as localization of signal energy of specific frequencies, or equivalently, suppression of signal energy at other frequencies [2] [1]. Apart from the fact that the design of 3D ST filters requires complex multidimensional visualisation in its spectral domain, the DSP concepts are very similar to its 1D temporal version. Suppose that a discrete domain 3D ST signal represented as $w_{input}(n_x, n_y, n_{ct}) \overset{DTFT}{\Leftrightarrow} W_{input}(\omega_x, \omega_y, \omega_{ct})$ where $n_{x,y,ct} \in \mathbf{Z}$ and $\omega_{x,y,ct} \in \mathbf{R}$, is being sent through a 3-D linear, shift-invariant filter with an impulse response of $h(n_x, n_y, n_{ct}) \overset{DTFT}{\Leftrightarrow} H(\omega_x, \omega_y, \omega_{ct})$ designed to pass only the spectral components of SOI and reject those unwanted signals such as noise, interference etc. to yield the filtered output signal $w_{output}(n_x, n_y, n_{ct}) \overset{DTFT}{\Leftrightarrow} W_{ouput}(\omega_x, \omega_y, \omega_{ct})$, then the corresponding filtering operation can be expressed in the frequency domain as,

$$W_{ouput}(\omega_x, \omega_y, \omega_{ct}) = W_{input}(\omega_x, \omega_y, \omega_{ct}) H(\omega_x, \omega_y, \omega_{ct}) \tag{5.1}$$

The filtering operation in discrete space-time domain $n_{x,y,ct} \in \mathbf{Z}$ can be represented in the form of a difference equation,

$$w_{ouput}(n_x, n_y, n_{ct}) = \frac{1}{b(0,0,0)} \Bigg[\sum_{r_x=1}^{N_1} \sum_{r_y=1}^{N_2} \sum_{r_{ct}=1}^{N_3} a(r_x, r_y, r_{ct}) w_{input}(n_x - k_x, n_y - k_x, n_{ct} - k_x) \underbrace{- \sum_{k_x=1}^{N_1} \sum_{k_y=1}^{N_2} \sum_{k_{ct}=1}^{N_3} b(k_x, k_y, k_{ct}) w_{output}(n_x - k_x, n_y - k_x, n_{ct} - k_x)}_{k_x + k_y + k_{ct} \neq 0} \Bigg] \tag{5.2}$$

where $a(n_x, n_y, n_{ct})$ are numerator coefficients, $b(n_x, n_y, n_{ct})$ are denominator coefficients and $N_1 \times N_2 \times N_3$ is the order of the filter. Such a difference equation leads to a continuous growth of the impulse response, and hence is of infinite extent. Therefore these filters are known as Infinite-extent Impulse Response (IIR) filters. In the special case where

$b(n_x, n_y, n_{ct}) \equiv b(0,0,0)$, the difference equation narrows down to a finite convolution expression, and the filter coefficients become $h(n_x, n_y, n_{ct}) = \frac{1}{b(0,0,0)} a(n_x, n_y, n_{ct})$ which is of finite extent. Hence, such filters are known as Finite Impulse Response (FIR) filters.

Previously reported work [4] [5] [7] [6] [8] [48] has been focused on both IIR and FIR designs mainly on the filtering of ST PWs based on their DOA. Therefore, the passband of the corresponding 3D ST filter $H(\omega_x, \omega_y, \omega_{ct})$ is designed to enclose a broadband spectral line with an orientation given by the relevant space-time DOA. As illustrated in Fig.5-1 a narrow cone filter and a beam filter are among the best candidates for such 3D ST filters. A Beam filter is a simple and effective method for filtering 3D ST-PW signals; however, for wide-angle approximations, the uniform width of passband suffers from poor directional selectivity near the origin $(\omega_x, \omega_y, \omega_{ct}) = (0,0,0)$; hence, is subjected to invasion of unwanted signals at lower frequencies [48]. Cone filters on the other hand are superior in this respect and, therefore, are of interest here.

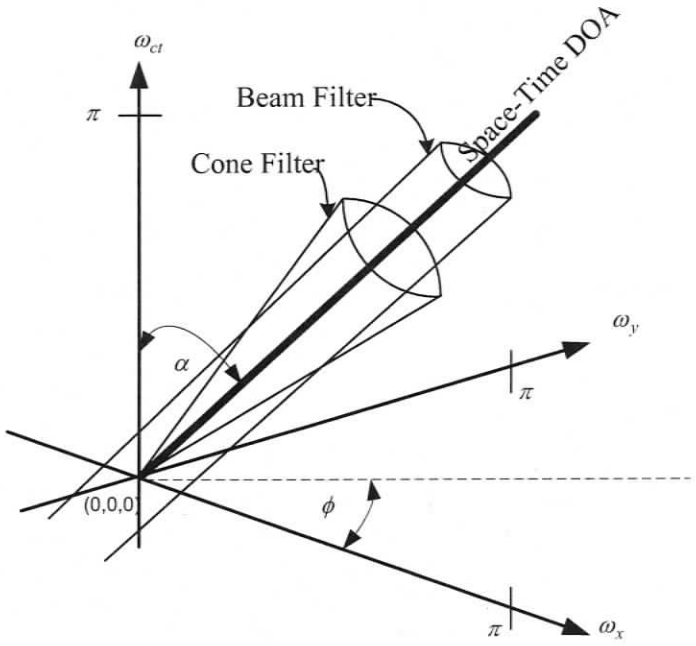

Figure 5-1. passband of the corresponding Cone and Beam filters enclosing a broadband spectral line with an orientation given by the relevant space-time DOA (θ, α)

5.3 Review of an Analytical IIR 3D ST Cone Filter Design

5.3.1 Review of Beam Filter Design using the Concept of Network Resonance

An innovative method of designing an IIR beam filter using a cascade of planar filters is discussed in [4]. In order to understand the planar filter design [3], consider an analogous 3D lossless inductance 2-port network terminated at a resistance as shown in Fig.5-2.

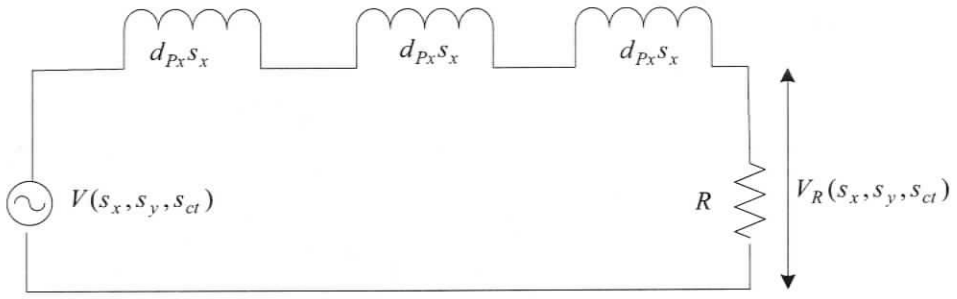

Figure 5-2. A lossless inductive 2-port network terminated at a resistance as an analogy to a beam filter design using the concept of network resonance

The transfer function across the resistor can be expressed by,

$$H_R(s)=\frac{1}{1+\frac{1}{B}d_P^T.S} \tag{5.3}$$

where $S=(s_x,s_y,s_{ct})\in\mathbf{C}^3$ is the Laplace variable, $d_P=[d_{Px}\ d_{Py}\ d_{Pct}]^T$ is the vector of inductance, and B is the uniform beamwidth corresponding to -3dB frequency planes $(d_P^T\Omega)=0$ of the magnitude spectrum $|H_R(s)|$ given by,

$$|H_R(s)|=\frac{B}{\sqrt{B^2+(d_P^T.\Omega)^2}} \tag{5.4}$$

where $\Omega=[\Omega_x,\Omega_y,\Omega_{ct}]^T$ and $s_{x,y,ct}=j\Omega_{x,y,ct}$. The corresponding practical-BIBO stable [52] discrete-domain transfer function $H_R(z)$ of $H_R(s)$ can be obtained by employing the triple bilinear transformation,

$$s_{x,y,ct}=\frac{z_{x,y,ct}-1}{z_{x,y,ct}-1} \tag{5.5}$$

which results in,

$$H_R(z) = H_R(s)\Big|_{s_i=\frac{z_i-1}{z_i-1}} = \frac{1}{1+\frac{1}{B}d_P^T.S}\Bigg|_{s_i=\frac{z_i-1}{z_i-1}} \tag{5.6}$$

where $z=[z_x\ z_y\ z_{ct}]^T \in \mathbf{C}^3$ and $z_{x,y,ct} = e^{j\omega_{x,y,ct}}$. This leads to the corresponding difference equation given by,

$$w_{output}(n_x, n_y, n_{ct}) = \frac{1}{b_{000}}\left[\sum_{i=0}^{1}\sum_{j=0}^{1}\sum_{k=0}^{1} a_{ijk}.w_{input}(n_x-i, n_y-j, n_{ct}-k) - \sum_{\substack{i=0\\ i+j+k\neq 0}}^{1}\sum_{j=0}^{1}\sum_{k=0}^{1} b_{ijk}.w_{output}(n_x-i, n_y-j, n_{ct}-k)\right] \tag{5.7}$$

This is a first order IIR 3D ST plane filter which has a uniform -3dB bandwidth of B. The respective numerator a_{ijk} and denominator coefficients b_{ijk} are derived by expanding the difference equation in (5.7) and are shown in Table 5-1.

Table 5-1. Numerator coefficients a_{ijk} and denominator coefficients b_{ijk} of the first-order IIR beam filter given in the difference equation (5.7)

a_{ijk}		b_{ijk}	
$a_{000} = B$	$a_{001} = B$	$b_{000} = d_{px} + d_{py} + d_{pct} + B$	$b_{001} = d_{px} + d_{py} - d_{pct} + B$
$a_{010} = B$	$a_{011} = B$	$b_{010} = d_{px} - d_{py} + d_{pct} + B$	$b_{011} = d_{px} - d_{py} - d_{pct} + B$
$a_{100} = B$	$a_{101} = B$	$b_{100} = -d_{px} + d_{py} + d_{pct} + B$	$b_{101} = -d_{px} + d_{py} - d_{pct} + B$
$a_{110} = B$	$a_{111} = B$	$b_{110} = -d_{px} - d_{py} + d_{pct} + B$	$b_{111} = -d_{px} - d_{py} - d_{pct} + B$

With an appropriate selection of two different transfer functions (or planar filters) such as $H_{R1}(z)$ and $H_{R2}(z)$ with suitable orientations in $(\omega_x, \omega_y, \omega_{ct})$ space, the intersection of the two filters will closely approximate a beam filter as illustrated in Fig.5-3. Clearly, there is an infinite number of selections for $H_{R1}(z)$ and $H_{R2}(z)$, and it is recommended in [48] to select mutually orthogonal plane filters for a better approximation of the beam. Thus a beam filter of half power beam width B having its beam axis line given by $d_{beam}^T = [d_{Px}\ d_{Py}\ d_{Pct}]$ can be obtained by,

$$H(e^{j\omega}) = H_{R1}(z)H_{R2}(z) = \left(\frac{1}{1+\frac{1}{B}d_{P1}^{T}.\Omega}\right)\left(\frac{1}{1+\frac{1}{B}d_{P2}^{T}.\Omega}\right) \tag{5.8}$$

where, $\Omega = [2\tan(\frac{\omega_x}{2})\,2\tan(\frac{\omega_y}{2})\,2\tan(\frac{\omega_{ct}}{2})]$ (the trigonometric version of (5.5)). If d_{beam}^{T} is represented in polar coordinates given by, $d_{beam}^{T} = [\sin\theta\cos\phi\ \sin\theta\sin\phi\ \cos\theta]$ with its centre axis-line in a certain orientation $\theta \in [0,\pi], \phi \in [0,2\pi]$, the corresponding d_{P1}^{T} and d_{P2}^{T} can be chosen as,

$$d_{P1}^{T} = [-\cos\upsilon_1\ 0\ \sin\upsilon_1] \text{ and } d_{P2}^{T} = [0\ -\cos\upsilon_2\ \sin\upsilon_2] \tag{5.9}$$

such that,

$$\upsilon_1 = \tan^{-1}(\sin\theta\cos\phi) \text{and } \upsilon_2 = \tan^{-1}(\sin\theta\sin\phi) \tag{5.10}$$

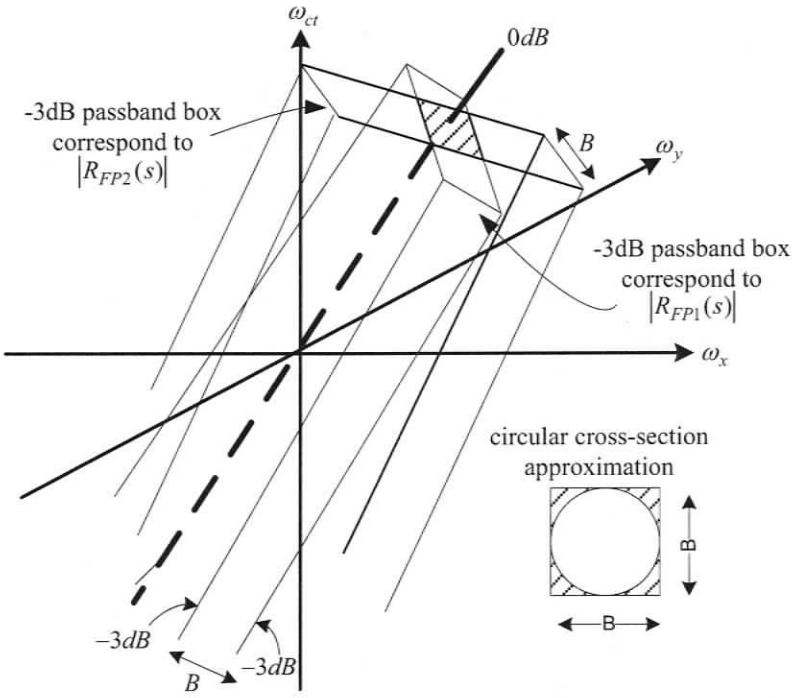

Figure 5-3. Illustration of the beam filter approximation as in (5.8) using two orthogonal planar filters explained in (5.6)

A simulated illustration of the surface area enclosed by-3dB planes of the orthogonal planar filters $H_{R1}(z)$ with $d_{P1}^{T} = [-1\,0\,0]$ and $H_{R2}(z)$ with $d_{P2}^{T} = [0\,-1\,0]$ having B=0.2 is shown in Figs.5-4 and 5-5.

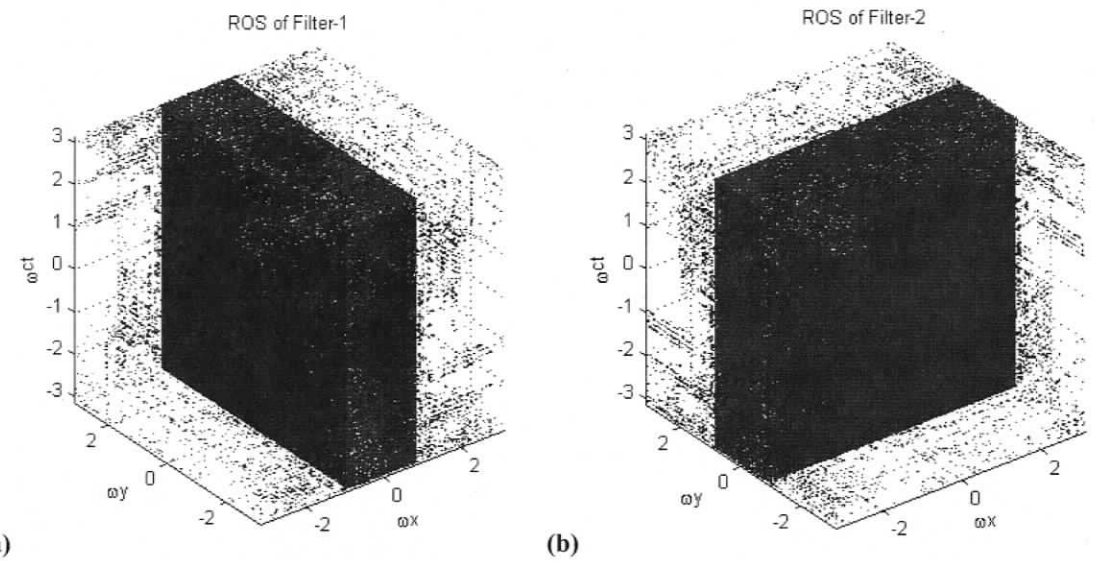

Figure 5-4 . Surface area enclosed by-3dB planes of the orthogonal planar filters (a) $H_{R1}(z)$ with $d_{P1}^T = [-1\ 0\ 0]$ (b) $H_{R2}(z)$ with $d_{P2}^T = [0\ -1\ 0]$

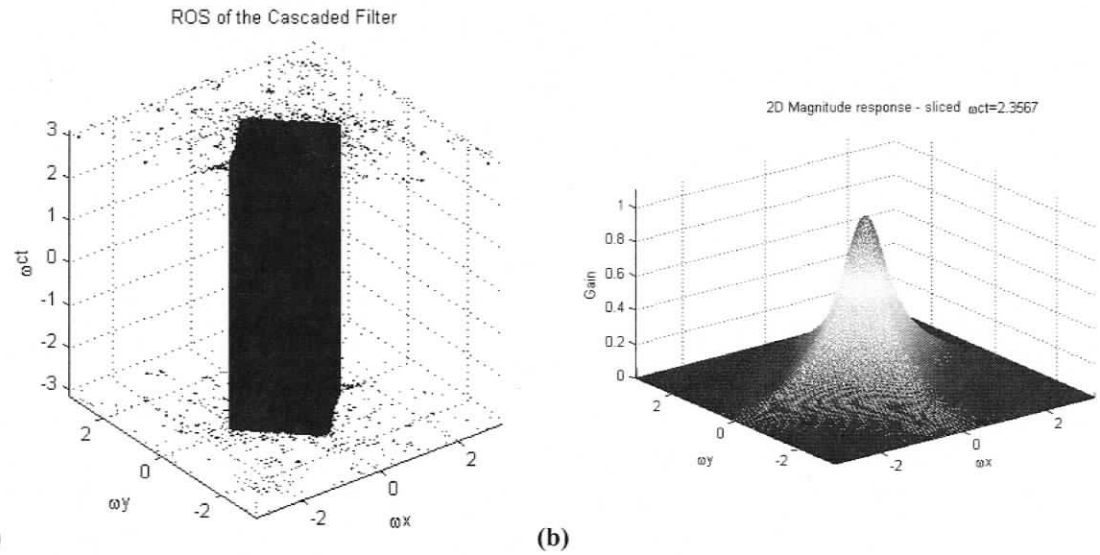

Figure 5-5. Beam approximation by cascading planar filters as in (5.8) (a)-3dB surface of approximated beam (b) magnitude response along the slice at $\omega_{ct} = 2.3562$

5.3.2 The Approximation of a Cone Filter Using a Filter Bank Structure of IIR Beam Filters and FIR Bandpass Filters

In [4] [5], an interesting method is introduced to approximate a cone shape passband by cascading several beam filters of different beam-widths at pre-assigned temporal sub-

bands. If L sub-bands are required to approximate the cone passband, then the k^{th} sub band may have its half-power beam width given by, $B_k = k\frac{2\pi \tan(\varepsilon)}{L}$. The temporal 1D bandpass filters are realized from the unit impulse response,

$$h_{BP,k}^{M} = w(n_{ct})h_{HB}^{M}(n_{ct})W_L^{-k} \overset{DTFT}{\Leftrightarrow} H_{BP,k}^{M}(e^{j\omega_{ct}}) \tag{5.11}$$

where $h_{HB}^{M}(n_{ct})$ is the prototype lowpass half-band filter of order M and $w(n_{ct})$ is a window function (Hamming) of order M, and $W_L \equiv \exp(-\frac{j\omega_{ct}}{L})$ is used to obtain the k^{th} sub-band from the k^{th} beam. The corresponding discrete domain 3D closed form transfer function $H_{CONE}(e^{j\omega})$ of the approximated 3D cone filter bank can therefore be expressed as,

$$H_{IIR\_S\_3D}(e^{j\omega_x}, e^{j\omega_y}, e^{j\omega_{ct}}) = \sum_{k=1}^{L} \frac{H_{BP,k}^{M}(e^{j\omega_{ct}})}{\left(\frac{1}{1+\left(\frac{L}{k2\pi\tan(\varepsilon)}\right)d_{F1}^{T}\Omega}\right)\left(\frac{1}{1+\left(\frac{L}{k2\pi\tan(\varepsilon)}\right)d_{F2}^{T}\Omega}\right)} \tag{5.12}$$

where, $\Omega = [2\tan(\frac{\omega_x}{2})\ 2\tan(\frac{\omega_y}{2})\ 2\tan(\frac{\omega_{ct}}{2})]$.

An illustration of this structure is given in Fig.5-6 which contains subsequent sub-bands k and $k+1$. An illustration of the filter bank ROS with a passband angle of 20° and $L=32$ bands, each band consisting of a 1-D FIR half-band bandpass filters of order 40 and a first order 2D IIR beamfilter is shown in Fig.5-7. The use of such 3D cone filter banks has a computational complexity and data storage requirements of $O(NM)$ where N is the number of bands and M is the order of the bandpass filter of the filter bank. This can be a concern especially in the case of real time implementation. For this reason [6] [8] have introduced a polyphase filter bank structure that significantly reduces the computational complexity.

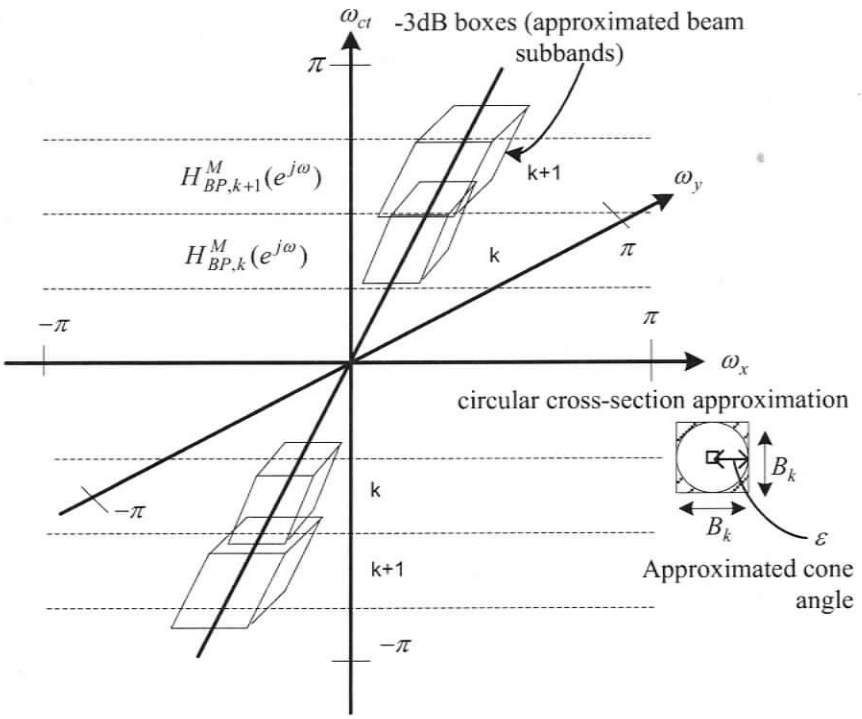

Figure 5-6. Cone passband approximation using a filter bank structure of 2-D IIR beam filters as in (5.8) and 1-D FIR half-band bandpass filters as in (5.11)

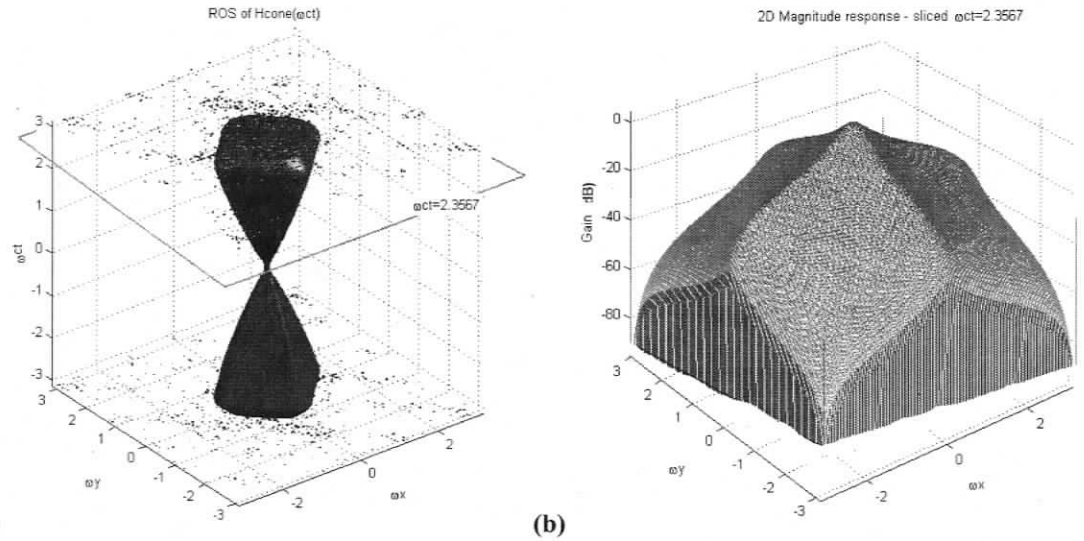

(a) (b)

Figure 5-7. The cone filter approximation as in (5.12) with a passband angle of 20° and $L=32$ bands, each band consisting of a 1-D FIR half-band bandpass filters of order 40 and a first order 2D IIR beamfilter (a) 3D ROS of the magnitude spectrum, containing 73.17% of energy (b) 2D, magnitude response sliced at $\omega_{ct}=2.3562$

5.4 An Overview of an Analytical FIR 3D ST Cone Filter Design by Cascading Two Wedge Shaped 3D ST Filters

In [22] [53] a method is presented to obtain the transfer function of the approximated cone by cascading two wedge shaped filters, as illustrated in Fig.5-8,

$$H_{FIR\_w\_3D}(\omega_x,\omega_y,\omega_{ct}) = H_{wedge1}(\omega_x,\omega_y,\omega_{ct}) \times H_{wedge2}(\omega_x,\omega_y,\omega_{ct}) \tag{5.13}$$

where $H_{wedge1}(\omega_x,\omega_y,\omega_{ct}) = H_{fan\_\alpha_x\_\varepsilon_x}(\omega_x,\omega_{ct})$ and $H_{wedge2}(\omega_x,\omega_y,\omega_{ct}) = H_{fan\_\alpha_y\_\varepsilon_y}(\omega_y,\omega_{ct})$.

The design of the FIR fan filters $H_{fan\_\alpha_{x/y}\_\varepsilon_{x/y}}(\omega_{x/y},\omega_{ct})$ is done using the modified Pie-Jaw fan filter design method with Leila-Bruton windowing [53]. The ROS of the impulse response of each wedge functions lie only on a plane in $(n_x,n_y,n_{ct}) \in \mathbf{R}^3$ given by,

$$h_{wedge1}(n_x,n_y,n_{ct}) = \delta(n_y).h_{fan\_\alpha_x\_\varepsilon_x}(n_x,n_{ct}) \text{ and}$$

$$h_{wedge2}(n_x,n_y,n_{ct}) = \delta(n_x).h_{fan\_\alpha_y\_\varepsilon_y}(n_y,n_{ct}) \tag{5.14}$$

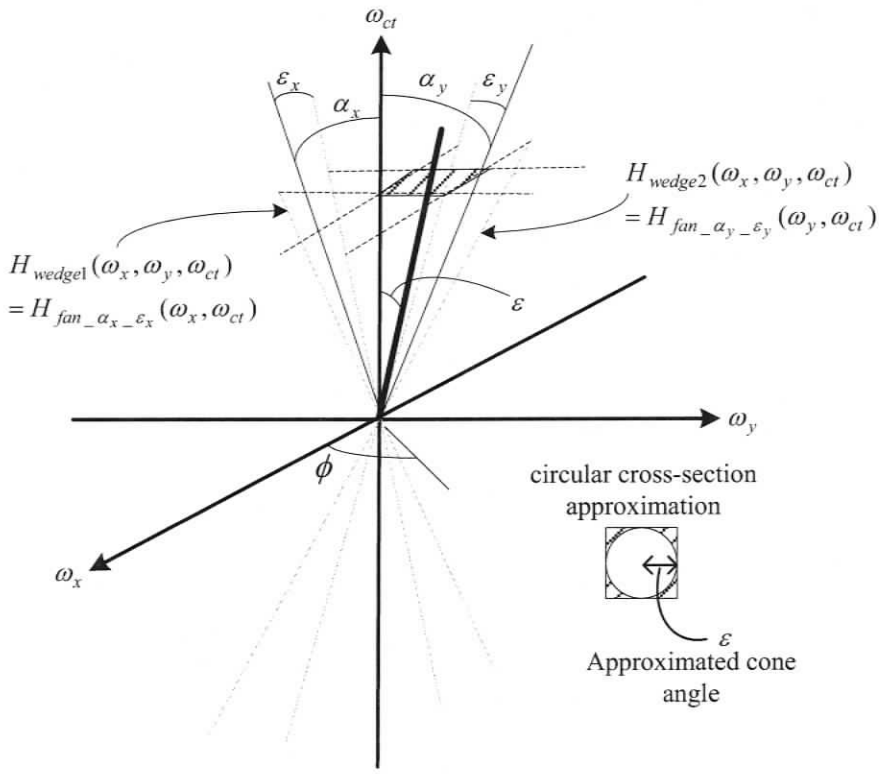

Figure 5-8. Cone passband approximation by cascading two wedge shaped filters as in (5.13)

As the multiplication of wedge shaped filters in the frequency domain is a convolution of their impulse responses, the respective impulse response $h(n_x, n_y, n_{ct})$ of the cone filter can be obtained by convolving the two fan filter impulse responses.

$$h_{wedge1}(n_x, n_y, n_{ct}) = \delta(n_x).h_{fan}(n_y, n_{ct}) *** \delta(n_y).h_{fan}(n_x, n_{ct}) \tag{5.15}$$

The 3D convolution of the impulse responses can also be interpreted as the convolution of the two normal planes given in (5.14) in the 3D space-time domain. Extending the idea in [53], a 3D thresholding method can be applied as proposed in [22] which lead to a reduction of the computational complexity of the resultant 3D cone filter. Simulated -3dB surfaces of the magnitude spectrum of two wedge shaped filters are illustrated in Fig.5-9. The FIR cone filter with a passband angle of 30° can be approximated as in (5.12) by cascading these two wedge filters. The-3dB surface plot of the approximated cone filter in the 3D spatio-temporal domain is illustrated in Fig.5-10

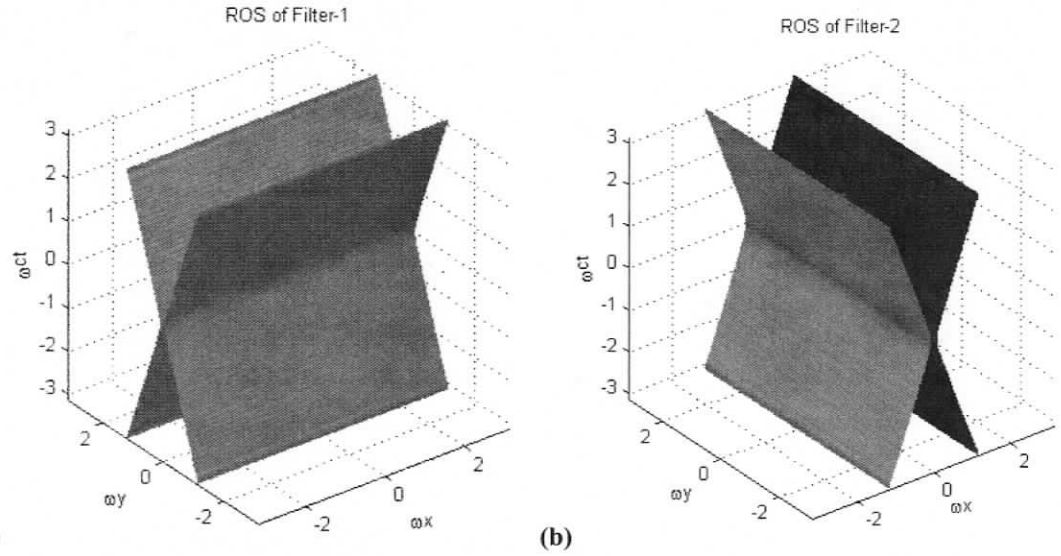

Figure 5-9. -3dB surface plot in the 3D frequency domain of (a) wedge filter-1 (b) wedge filter-2

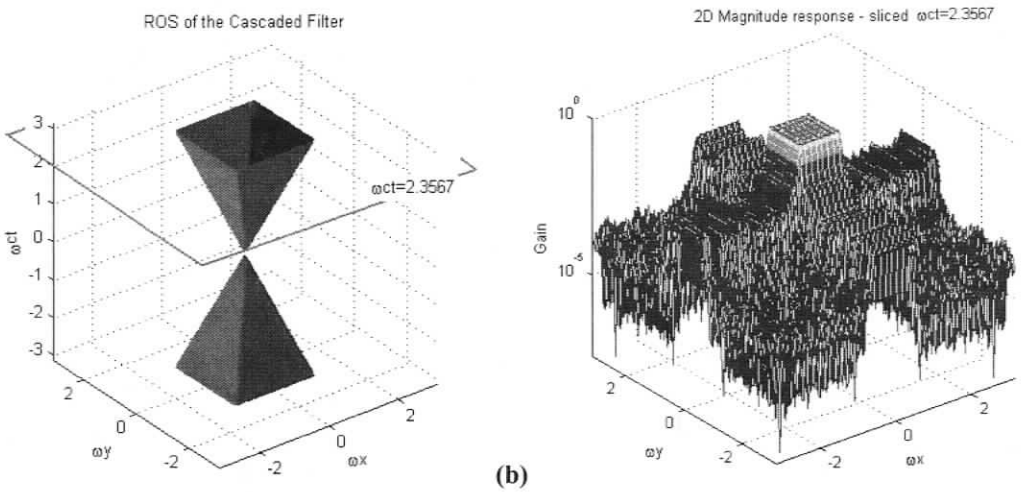

Figure 5-10. The cone filter of a passband angle $\varepsilon = 30$ approximated by cascading wedge sgaped filters (a) -3dB surface plot of 3D ROS of the magnitude spectrum (b) 2D, magnitude response sliced at $\omega_{ct} = 2.3562$

5.5 The Proposed 3D Linear Phase FIR Cone Filter Bank of 1D Linear Phase FIR Filters and 2D Circularly Symmetric Zero Phase FIR Filters.

The proposed 3D linear phase FIR cone filter is based on a filter bank structure consisting of 1D linear phase FIR filters and 2D circularly symmetric zero phase FIR filters. The transfer function of the filter bank can be expressed by,

$$H_{FIR\_C\_3D}(e^{j\omega_x}, e^{j\omega_y}, e^{j\omega_{ct}}) = \sum_{k=1}^{L} H_k^{N_1}(e^{j\omega_{ct}}) H_{C,k}^{N_2}(e^{j\omega_x}, e^{j\omega_y}) \tag{5.16}$$

where $H_k^{N_1}(e^{j\omega_{ct}})$ is the transfer function of the k^{th} band 1D FIR filter of order N_1, and $H_{C,k}^{N_2}(e^{j\omega_x}, e^{j\omega_y})$ is the k^{th} band 2D FIR filter of order $N_2 \times N_2$, where L bands are used to approximate the cone passband. The structure of the filter bank that constructs the transfer function derived in (5.16) is illustrated in Fig.5-11 and an illustration cone shaped passband approximation using subbands is shown in Fig.5-12.

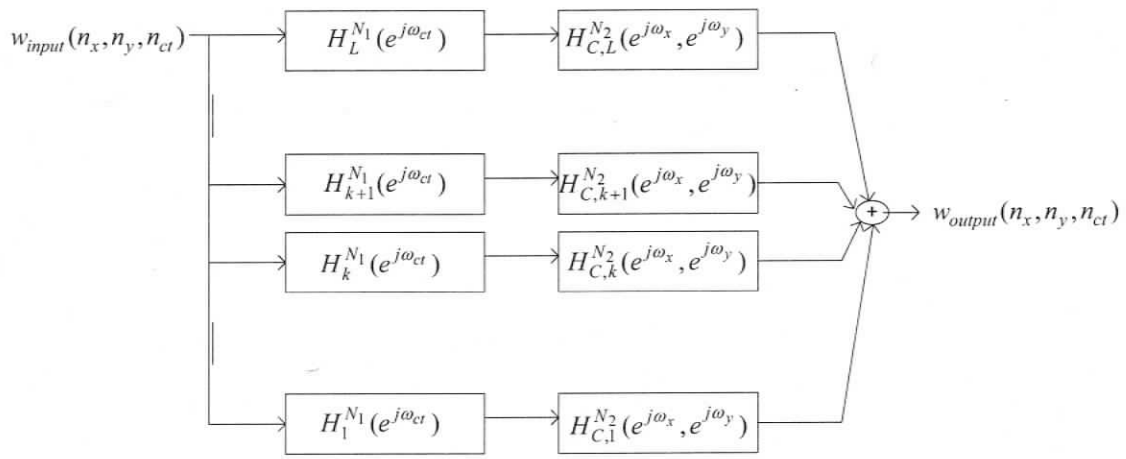

Figure 5-11. The structure of the filter bank as in (5.16) which approximates the required cone shaped passband

The $H_k^{N_1}(e^{j\omega_{ct}})$ is obtained from its impulse response given by,

$$h_k^{N_1}(n_{ct}) = i_k^{N_1}(n_{ct}) w_{hamm}(n_{ct}) \quad k = 1,2...L \tag{5.17}$$

where $w_{hamm}(n_{ct})$ is the hamming window of order N_1, and $i_k^{N_1}(n_{ct})$ is the ideal impulse response,

$$i_k^{N_1}(n_{ct}) = \frac{\omega_{k+1}}{\pi}\operatorname{sinc}(n_{ct}\omega_{k+1}) - \frac{\omega_k}{\pi}\operatorname{sinc}(n_{ct}\omega_k) \quad \text{for } \omega_k = Lk/\pi \tag{5.18}$$

derived from the inverse discrete time Fourier transform of the ideal transfer function,

$$I_k^{N_1}(e^{j\omega_{ct}}) = \begin{cases} 1 & \pi(k-1) \le \omega_{ct}(L-1) < \pi k \\ 0 & elsewhere \end{cases} \tag{5.19}$$

Similarly, $H_{C,k}^{N_2}(e^{j\omega_x},e^{j\omega_y})$ is obtained from its impulse response given by,

$$h_{C,k}^{N_2}(n_x,n_y) = i_{C,k}^{N_2}(n_x,n_y) w_{hamm2}^{N_2}(n_x,n_y), \quad k = 1,2..L \tag{5.20}$$

where $w_{hamm2}^{N_2}(n_x,n_y)$ is the 2D hamming window that preserves the zero phase property [1], and the ideal impulse response $i_{C,k}^{N_2}(n_x,n_y)$ is derived from the 2D FIR circularly symmetric ideal transfer function,

$$I_{C,k}^{N_2}(e^{j\omega_x},e^{j\omega_y}) = \begin{cases} 1 & \sqrt{\omega_x^2+\omega_y^2} \le r_k = \dfrac{k\pi}{L}\tan(\varepsilon) \\ 0 & elsewhere \end{cases} \tag{5.21}$$

where ε is the required passband cone angle. The derivation of $i_{C,k}^{N_2}(n_x,n_y)$ uses the inverse Fourier transform given by,

$$i_{C,k}^{N_2}(n_x,n_y)=\frac{1}{4\pi^2}\int_{\omega_x=-\infty}^{\infty}\int_{\omega_y=-\infty}^{\infty} I_{C,k}^{N_2}(e^{j\omega_x},e^{j\omega_y})e^{j(n_x\omega_x+n_y\omega_y)}d\omega_x d\omega_y \tag{5.22}$$

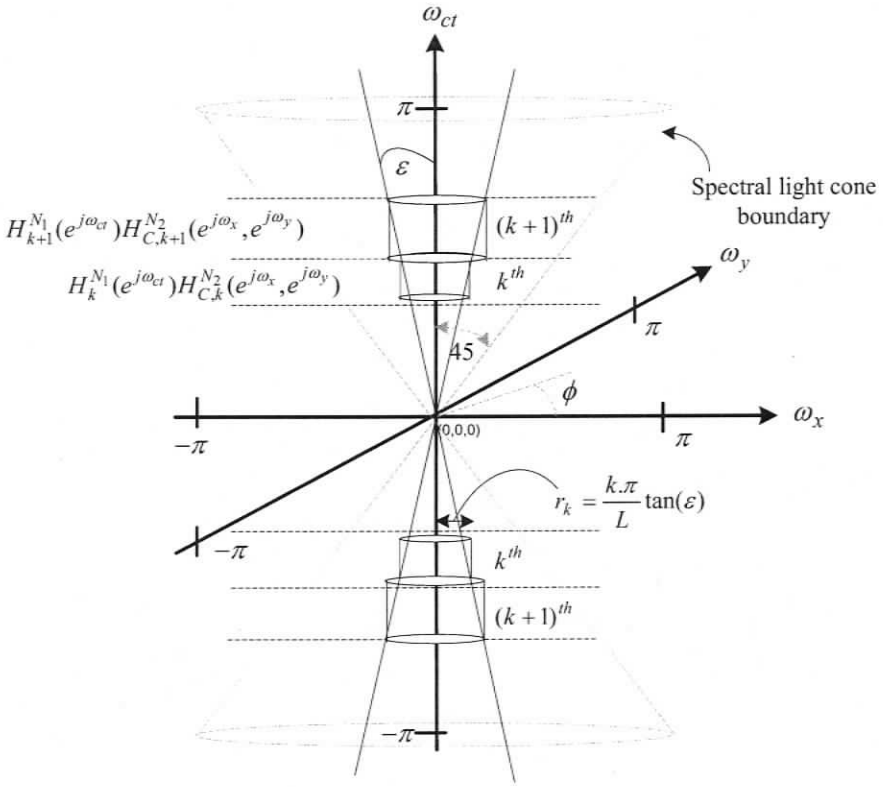

Figure 5-12. The linear phase analytic cone filter approximation with L bands, each band consisting of a 1D linear phase FIR filter and a 2D zero phase circularly symmetric FIR filter.

The region of integration in (5.22) is circular, hence it is not separable in the Cartesian coordinates. The integration can easily be performed by replacing the variables ω_x and ω_y into polar coordinate variables (the Hankel Transformation) as,

$$\overline{\omega}\equiv\sqrt{\omega_x^2+\omega_y^2}\ ,\ \overline{\psi}\equiv\tan^{-1}\frac{\omega_y}{\omega_x}\text{ and }\overline{\vartheta}\equiv\tan^{-1}\frac{n_y}{n_x} \tag{5.23}$$

The expression in (5.22) now can be simplified to,

$$i_{C,k}^{N_2}(n_x,n_y)=\frac{1}{4\pi^2}\int_0^{\eta_k}\int_0^{2\pi}\overline{\omega}e^{j\overline{\omega}\left[\sqrt{n_x^2+n_y^2}\cos(\overline{\psi}-\overline{\vartheta})\right]}d\overline{\omega}d\overline{\psi}$$

$$= \frac{1}{2\pi} \int_0^{r_k} \overline{\omega} J_0\left(\sqrt{n_x^2 + n_y^2}\right) d\overline{\omega}$$

$$= \frac{r_k J_1\left(r_k \sqrt{n_x^2 + n_y^2}\right)}{2\pi\sqrt{n_x^2 + n_y^2}} \tag{5.24}$$

where $J_0(.)$ and $J_1(.)$ is the Bessel function of first kind of order-0 and order-1 respectively. The Bessel function and $\sqrt{n_x^2 + n_y^2}$ in (5.24) makes the filter coefficients to be real and symmetric as,

$$i_{C,k}^{N_2}(n_x, n_y) = i_{C,k}^{N_2}(-n_x, -n_y) \tag{5.25}$$

resulting in the corresponding $I_{C,k}^{N_2}(e^{j\omega_x}, e^{j\omega_y})$ being purely real and zero-phase. The 3D transfer function in (5.16) is therefore linear phase due to the cascade of linear phase 1-D and zero-phase 2D filters. A simulated illustration using -3dB surface plot of the ROS of the magnitude spectrum of the proposed cone filter approximation with a stopband angle of 80° and 16 bands, each band consisting of a 1D FIR filter of order 40 and a 2D FIR circular symmetric filter of order 40 is shown in Fig.5-13.

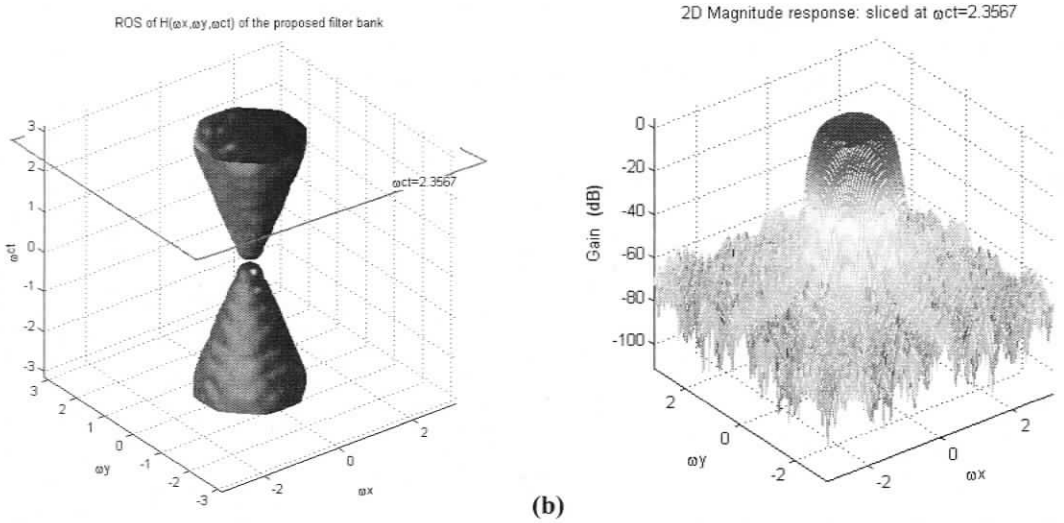

(a) (b)

Figure 5-13. The cone filter approximation with a stopband angle of 80° and 16 bands, each band consisting of a 1D FIR filter of order 40 and a 2D FIR circular symmetric filter of order 40 (a) -3dB surface plot of 3D ROS of the magnitude spectrum (b) 2D, magnitude response sliced at ωct=2.3562.

5.6 A Comparison Amongst the Three Analytical 3D ST Cone Filter Designs

In this section the three analytical 3D ST filter designs, the IIR cone filter bank $H_{IIR\_S\_3D}$, the FIR cone approximation using wedge shaped filters $H_{FIR\_w\_3D}$ and the proposed FIR cone filter bank $H_{FIR\_C\_3D}$ are compared, with respect to their suitability on the filtering of synthesised AAs/FPAs signals involved in radio astronomical applications.

As mentioned in Section 5.1, the requirements are for linear phase cone filters with passbands having circularly symmetric cross-section. First, the magnitude distribution of the passband on the plane $(\omega_x, \omega_y) \in \mathbf{R}^2$ as illustrated in Fig.5-14, is compared. The IIR cone filter bank $H_{IIR\_S\_3D}$ has the weakest cross section among the three filters where the unity gain is maintained only at the center of the cone whereas the circular boundary of the cone is approximated by a square cross section with -3dB gain. The FIR cone approximation using wedge filters, $H_{FIR\_w\_3D}$, however, maintains a unity gain over a region of a square, but does not approximate a circular cross-section. For these reasons both $H_{IIR\_S\_3D}$ and $H_{FIR\_w\_3D}$ contain a region of error (shaded in Fig.5-14), which may lead the ROSs of unwanted signals to fall in to the passband of the filter.

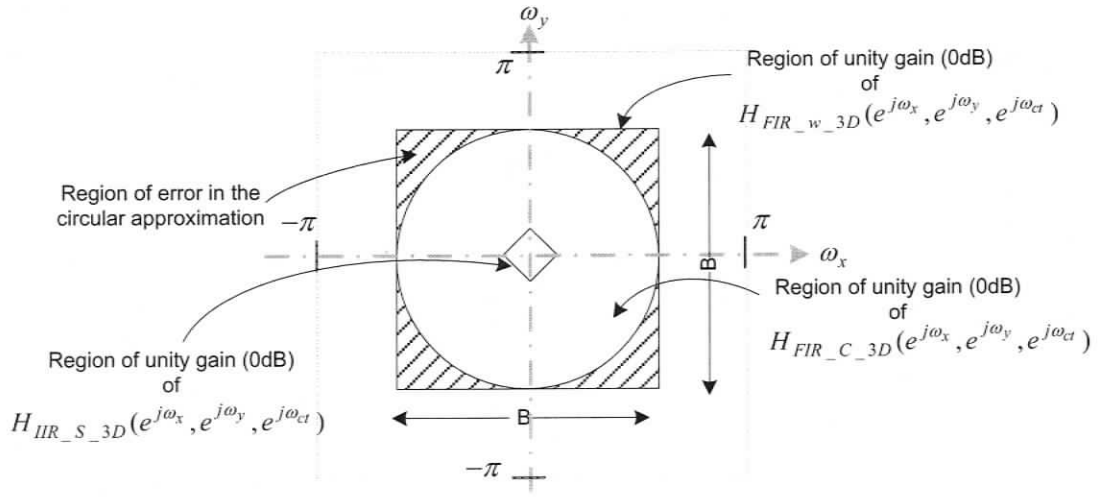

Figure 5-14. An illustration of the regions of magnitude distribution of the designed 3D cone filters in the spatial frequency plane $|\omega_{x,y}| \le \pi$ sliced at a given ω_{ct}

The FIR cone filter bank $H_{FIR\_C\_3D}$ on the other hand is superior in this aspect as it inherently maintains a circular cross section.

Next, in order to examine the cone approximation, the three filters are tested using two synthetic BB ST signals. The two signals are synthesised as a BB SOI on an FPA setup of $D=64$ and $F/D=0.41$ shown in Fig.3.16, (in Chapter-3) and as a BB MC photonically reflected signal propagating at $a=3.14$ ($\sigma=1dB$, $r_0=T_s=0.0366m$) discussed in Chapter-4. In the spatio-temporal frequency domain, the BB SOI has a ROS which is similar to a solid cone with an angle of approximately 43^0 whereas the BB ST MC signal has ROS which is similar to a spectral light cone with a small thickness. They are synthesised such a way that if an ideal cone filter with a passband angle of $\varepsilon=43^0$ would completely enclose the BB SOI in its passband whereas BB ST MC signal would lie in the stopband. The two test signals are filtered using the three analytic cone filters of passband angle of $\varepsilon=43$ and the results are summarised in Table 5-2.

Table 5-2. A comparison of the passband and stopband performance of the designed 3D cone filters using test signals synthesised using BB broadside SOI on an FPA and BB MC signal

Cone Filter Type (passband angle $\varepsilon=43$)	Energy of the BB SOI on an FPA Setup: $D=64$ and $\frac{F}{D}=0.41$		Energy of BB ST MC signal with $a=3.14$ ($\sigma=1dB$, $r_0=T_s=0.0366m$)	
	input	filtered output	input	filtered output
$L=16$ sub-band filter bank structure of first order 2D-IIR beam filters and 1D FIR bandpass filters of order 40 $H_{IIR\_S\_3D}$	1	0.0725	1	0.0431
Cone filter approximated by cascading two FIR wedged shaped filters of order $40\times40\times40$ $H_{FIR\_w\_3D}$	1	0.8393	1	0.4615
$L=16$ sub-band filter bank structure of 2D zero-phase circular symmetric FIR filters of order 40×40 and 1D FIR bandpass filters of order 40 $H_{FIR\_C\_3D}$	1	0.9821	1	0.3676

The performance of $H_{FIR\_C\_3D}$ indicates fairly good passband and stopband approximation whereas $H_{IIR\_S\_3D}$ indicates the best stopband performance but a weak passband performance. The $H_{FIR\_w\_3D}$ shows moderate performance compared to $H_{FIR\_C\_3D}$. In addition to the weak passband performance of the IIR cone filter bank $H_{IIR\_S\_3D}$ due to the non-flat non-circular symmetric cross-section; it also suffers from non-linear phase response which makes it unsuitable for radio astronomical applications without any additional processing. Therefore, linear phase FIR cone filter approximations $H_{FIR\_w\_3D}$ and $H_{FIR\_C\_3D}$ are best suited.

Table 5-3. A comparison of the passband and stopband performance of the FIR 3D cone filter approximations with respect to ST-PWs of different DOAs

Cone Filter Type (passband angle $\varepsilon = 43$)	Energy of the BB PW-1 ($\theta = 0, \phi = 45$)		Energy of the BB PW-2 ($\theta = 30, \phi = 10$)		Energy of the BB PW-3 ($\theta = 90, \phi = 45$)	
	input	filtered output	Input	filtered output	input	filtered output
Cone filter approximated by cascading two FIR wedged shaped filters of order $40 \times 40 \times 40$ $H_{FIR\_w\_3D}$	1	0.7847	1	0.6352	1	0.3923
$L = 16$ sub-band filter bank structure of 2D zero-phase circular symmetric FIR filters of order 40×40 and 1D Bandpass Filters of order 40 $H_{FIR\_C\_3D}$	1	0.9812	1	0.8799	1	0.1086

Finally, the two FIR cone filter designs are further compared based on their performance on the filtering of BB ST-PWs. Three synthetic BB ST PW signals with DOAs of PW-1 ($\theta = 0, \phi = 45$), PW-2 ($\theta = 30, \phi = 10$) and PW-3 ($\theta = 90, \phi = 45$) are used for the filtering analysis. The DOAs are chosen such that, ROSs in the 3D spatio-temporal frequency domain of PW-1 and PW-2 are in the passband, whereas PW-3 it is in the

stopband of $H_{FIR\_C\_3D}$. The DOA of PW-3 is carefully selected such that its ROS in the 3D spatio-temporal frequency domain resides in the 'approximation error region' of $H_{FIR\_w\_3D}$ (the shaded region in Fig. 5-14). The filtering results are summarised in Table 5-3. As expected, compared to $H_{FIR\_w\_3D}$, $H_{FIR\_C\_3D}$ indicated better passband and stopband performances.

The computational complexity of the $H_{FIR\_C\_3D}$ can be further reduced by employing a polyphase structure [6] and can easily be reconfigured to approximate partial-cone or non-cone circularly symmetric passband shapes. The partial cone shape approximation may be required for temporally downconverted intermediate-frequency (IF) ST signal filtering whereas non-cone approximations may be required for filtering/suppression of signals that has a ROS approximated by non-conic shapes but with circular cross-sections. Based on the performance, $H_{FIR\_C\_3D}$ is preferred over the other two methods and will be used on the filtering of synthesised BB radio astronomical signals in the next chapter.

5.7 Summary

Two previously reported analytic FIR and IIR 3D ST cone filters are discussed and simulated to understand their cone shaped passband approximation. From the simulation results it is observed that both filters have poor approximation to the required circular cross-section of the cone shaped passband. To address this deficiency, a novel ST cone filter bank structure comprised of 2D FIR circularly symmetric filters and 1D FIR bandpass filters is introduced to better approximate the cone shaped passband.

The proposed filter has linear phase property and a circularly symmetric cross-section in comparison to the other two analytical designs. These are essential requirements of a potential ST filter for the use of radio astronomical applications, especially on the filtering of signals analysed in Chapters 3 and 4. Several synthetic BB signals relevant for radio astronomical applications are filtered by employing the three filters to analyse and compare their performance. As expected, the proposed ST FIR filter demonstrated superior performance over the other two analytical designs.

Furthermore, the proposed filter is capable of approximating partial cone shapes and circularly symmetric non-cone shapes. These may be useful for filtering of temporally down-converted IF ST signals and filtering/suppression of signals that have ROSs approximated by non-conic shapes with a circular cross-section, respectively. It is also possible to employ a polyphase structure to the proposed filter bank to maintain a reasonable computational complexity.

Chapter 6

Numerical Simulation Analysis of 3D Space-Time Digital Filtering Applied on FPA/AA Signals

In this Chapter, the cone filter bank proposed in Chapter-5 is used to process synthesised BB radio frequency interference (RFI), BB signal of interest (SOI), and BB mutually coupled (MC) signals discussed in Chapters 3 and 4. First, the mitigation of BB RFI and suppression of BB MC signals are numerically analysed by employing the proposed ST cone filter. Next, the performance of the proposed cone filter for filtering of BB SOI in the presence of BB RFI and BB MC signals is addressed. Finally, the proposed cone filter is employed on simulated (synthesised) composite signals received by AAs and FPAs to investigate the performance of the proposed approach.

6.1 Introduction

The application of a 3D ST digital filter on the mitigation of BB RFI and suppression of BB ST MC signals exploit the ROS in the 3D frequency domain. The over-the-horizon ST BB RFI signals under considerations have their ROSs in the spatio-temporal frequency domain, on or close to the surface of the spectral light cone. The ROS of ST BB MC signals may confine to and around the spectral light cone with a spatial smearing which depends on the spatial attenuation constant. Therefore these signals can be attenuated by a suitable 3D ST filter encompassing ROS of the BB SOI in its passband and the spectral light cone in its stopband. A 3D ST filter bank structure proposed in Chapter-5 is employed to approximate the required ST filter. The main advantage of the proposed ST filtering approach is its inherent capability of broadband processing. Previously reported methods on the mitigation of RFI based on temporal blanking techniques (which are mostly suitable for intermittent RFI [12]), spatial filtering techniques (which use subspace-projection methods [13] [14] [15]), cancellation techniques [54] (which use a reference signal approach [16]) and post-correlation cancellation and anti-coincidence techniques [17] are mostly being investigated in the

context of narrowband applications. For broadband applications sub-band processing mechanisms comprised of such narrowband techniques are required. Therefore, finding a universal technique addressing broadband RFI mitigation for radio astronomical applications is challenging. For the suppression of mutually coupled signals, previously reported methods are mostly based on, principles of radiation pattern multiplication [18], active element reflection coefficient and scattering parameter analysis [19], sensitivity analysis of large phased arrays using method-of-moments simulations [20] and, network theory framework [21]; they are also mostly suitable for narrowband applications. It is also notable that the previously reported investigations on the suppression of MC signals have not been attempted in a spatio-temporal filtering approach.

To analyse the performance of the proposed 3D space-time filtering approach, the proposed filter bank structure, composed of 2D zero-phase circular symmetric FIR filters and 1D FIR bandpass filters, is employed on the synthesised BB ST signals on AAs and FPAs. These signals include BB RFI/BB SOI discussed in Chapter 3 and BB MC signals comprised of photonically reflected and internally generated LNA noise, discussed in Chapter 4. The BB nature of the ST signals is synthesised by superimposing monochromatic equi-amplitude cosine functions in the form,

$$\overline{w}(.) = \sum_{k=1}^{k_{MAX}} \cos[2\pi f_k(.)] \quad ..\mathbf{f} = [f_1, f_2 ....f_{k_{MAX}}] \tag{6.1}$$

Using the expression in (6.1), the discrete domain BB ST PWs $w_{D\_PW}(n_x, n_y, n_{ct})$ are synthesised as,

$$w_{D\_PW}(n_x, n_y, n_{ct}) = \overline{w}(\sin\theta_{PW}\cos\phi_{PW} n_x T_x + \sin\theta_{PW}\sin\phi_{PW} n_y T_y + n_{ct} T_{ct}) \tag{6.2}$$

and the discrete domain BB ST photonically reflected MC signals $w_{D\_MC}(n_x, n_y, n_{ct})$ are synthesised as,

$$w_{D\_MC}(n_x, n_y, n_{ct}) = e^{-a\sqrt{n_x T_x + n_y T_y}}\, \overline{w}(-\sqrt{(n_x T_x)^2 + (n_y T_y)^2} + n_{ct} T_{ct}) \tag{6.3}$$

where a is the attenuation constant, (θ_{PW}, ϕ_{PW}) is the spatial-DOA of the ST PW and $(n_x, n_y, n_{ct}) \in \mathbf{Z}^3$. The DOA (θ_{PW}, ϕ_{PW}) is selected such that they satisfy the condition,

$$90^0 \geq \theta_{PW} > \theta_{AA/FPA\_SOI\_\max}, \forall \phi_{PW} \tag{6.4}$$

for BB RFI signals on AAs/FPAs where $\theta_{AA/FPA\_SOI\_\max}$ is the maximum angle for SOI in both AA/FPA cases. In the case of AAs (θ_{PW},ϕ_{PW}) in (6.2) are chosen such that,

$$\theta_{PW} \le \theta_{AA\_SOI\_\max}, \forall \phi_{PW} \tag{6.5}$$

to synthesise BB SOI on AAs. The BB SOI on the FPA, is synthesised as mentioned in Chapter-3, sub-section 3.6. The BB MC LNA noise signal is synthesised by replacing $\overline{w}(.)$ in (6.3) as,

$$\overline{w}(.) = N_{GWN,\overline{m},\sigma}(.) * h_{FIR,BW}(.) \tag{6.6}$$

where $h_{FIR,BW}(.)$ is an impulse response of the bandpass FIR filter of bandwidth BW and $N_{GWN,\overline{m},\sigma}(.)$ is Gaussian white noise with mean $\overline{m}=0$ and standard deviation $\sigma=0.5$ generated by a stochastic process.

The BB antenna array under consideration here (either as a dense AA or a FPA mounted on a parabolic reflector), is assumed to be a $(2N_x+1)\times(2N_y+1)=81\times81$ element rectangularly-distributed uniformly-weighted broadband antenna array that has an operational bandwidth of 1-4GHz. Assuming that the speed of light is $c=0.3Gm/s$ the corresponding slightly over-sampled spatio-temporal sampling distances are chosen, $T_{x,y,ct}=T_s=1/f_s=0.0366m$ such that $f_s/2=4.1GHz/3Gm/s$ which implies that they satisfy the Nyquist sampling condition in space-time. An 81×81 array is chosen to reduce the finite aperture effect to better emphasise the ST filtering concept. The operational bandwidth of the array is selected to emphasise on the BB processing, however, it can be of an arbitrary range (given that Nyquist sampling conditions are satisfied).

6.2 The Mitigation of BB RFI by Employing the Proposed 3D FIR Cone-Shaped Passband ST Digital Filter

Consider two over-the-horizon low-azimuth BB (1GHz-4GHz) RFI signals synthesised as in (6.2) for $\mathbf{f}=[1,1.05,1.1...4]GHz$, having spatial DOAs given by (θ_1,ϕ_1)=(85,80) (PW-1) and (θ_2,ϕ_2)=(90,10) (PW-2), respectively (corresponding space-time DOAs are (α_1,ϕ_1) =(44.8,80) (PW-1) and (α_2,ϕ_2)=(45,10) (PW-2)). The ROSs of the spectra of these two RFI signals are shown in Fig.6-1. The contour plot of a slice at $\omega_{ct}=2.1677$ as shown in Fig.6-1(b) clearly indicate that the two RFI signals have their ROS on or very close to the

surface of the spectral light cone, as expected. Clearly, it is possible to select a suitable passband angle ε of the 3D ST cone filter such that it encloses RFI signals in its stopband. The selection of ε must consider the ROS of the SOI, which will be discussed in sub-section 6.5. Table 6-1 summarizes the filtering results on the BB RFI signals by employing the proposed $L=16$ band filter bank structure composed of 2D zero-phase circular symmetric FIR filters of order 40×40 and 1D FIR bandpass filters of order 40 with different passband cone angles ε = [30 35 40 43]. The suppression efficiency is calculated as a percentage of the filtered energy to the input energy of the BB RFI signals and is used as the metric to evaluate performance of the ST filtering approach on the mitigation of RFI.

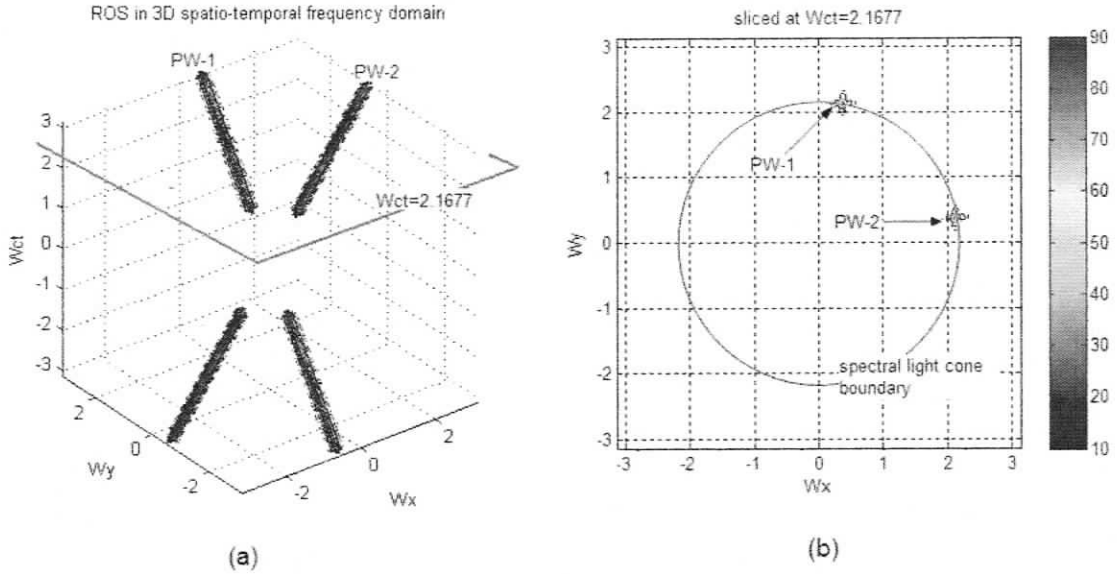

Figure 6-1. (a) 3D ROS of the magnitude spectrum of low azimuth RFI signals (θ_1,ϕ_1)=(85,80) (PW-1) and $(\theta_2,\ \phi_2)$=(90,10) (PW-2), containing 94% of energy (b) a slice at $\omega_{ct}=2.1677$ indicating the relative position with respect to the light cone boundary

The results presented in Table 6-1 confirm significant attenuation of BB RFI at lower cone passband angles ε = [30 35 40]. A reduction in the suppression efficiency (down to 81%) at cone angle ε =43 is due to the spatial smearing of BB RFI signal PW-1 caused by the finite aperture effect of the antenna array. This effect caused spectral leakage of

the BB RFI signal PW-1, (α_1, ϕ_1)=(44.8,80) in to the cone filter passband and this effect is dominant at low frequencies.

Table 6-1. The RFI suppression efficiency of the 3D space-time filtering employed on FPA/AA

RFI signals: PW-1 and PW-2				
3D cone filter angle (ε)	30	35	40	43
Energy of the input	2	2	2	2
Energy of the output	0.0039	0.0069	0.0252	0.37
Supp. efficiency (%)	99.81	99.65	98.74	81.19

6.3 The Suppression of BB MC ST Signals by Employing the Proposed 3D FIR Cone-Shaped Passband ST Digital Filter

ST BB MC signals may contain both photonically reflected (from incident RFI and/or SOI signals) and internally generated LNA noise. The proposed filtering approach is investigated by employing the proposed 3D ST cone filter bank structure for the suppression of ST BB MC signals. Based on the analysis in Chapter-4, sub-sections 4.6 and 4.8, it was observed that the spatial attenuation of the ST MC signals depends on the attenuation constant a and an increase in a leads to increased spatial smearing of the ROS of ST MC in the spatial frequency plane $(\omega_x, \omega_y) \in \mathbf{R}^2$ that spread the ROS to both outside and inside of the spectral light cone $\omega_x^2 + \omega_y^2 = \omega_{ct}^2$. Therefore, the proposed ST cone filter of various cone angles ε, is being employed on BB MC signals to analyse the suppression performance for various values of the attenuation constant a.

6.3.1 The Suppression of MC BB Photonically Reflected Signals

BB (1-4GHz) MC photonically reflected signals synthesised as in (6.3) propagating with spatial attenuation constants of a = [6.29 15.73 31.47 47.20 62.94 78.67 94.41 110.14 125.88] (σ =[2 5 10 15 20 25 30 35 40] dB, $r_0 = T_s = 0.0366m$) are filtered using a $L = 16$ band filter bank structure composed of 2D zero-phase circular symmetric FIR

filters of order 40×40 and 1D FIR bandpass filters of order 40 at cone angles of ε = [20 25 30 35 40].

A summary of the numerical filtering results pertaining to 3D ST cone angles ε = [20 30 40] are shown in Table 6-2. The suppression efficiency is calculated as a percentage ratio of the filtered energy to the input energy and is used as the metric to evaluate the performance of the ST filtering approach on the suppression of mutual coupling. It can be seen from Table 6-2 that the best performance can be obtained for small values of a and ε. At very high attenuation levels, the ST MC signal on the spatial space $(n_x, n_y) \in \mathbf{Z}^2$ would be close to approximating spatial impulse $\delta(n_x, n_y)$, and the corresponding ROS of the spectrum would spread along spatial frequency plane $(\omega_x, \omega_y) \in \mathbf{R}^2$. For this reason, signals emanating from an antenna with a high attenuation constant may have a higher maximum value in 3D space-time than signals with the same energy but emanating from an antenna with lower attenuation constant. These latter signals will have a higher maximum values in 3D frequency domain than the former ones. This behaviour is clearly visible in Table 6-2.

As the inter-antenna attenuation increases, the suppression efficiency tends to decrease and it is significantly lower at higher filter angles. It is also observed that as the inter-antenna attenuation is increased, the suppression efficiency reaches a minimum (at σ =15dB suppression ratio is 44.5975% for cone angle ε=40), however, as the inter-antenna attenuation σ is further increased the suppression efficiency increases. A possible reason for this phenomina, is that the MC signals become close to a spatial impulse at higher inter-antenna attenuations resulting in a uniformly smeared ROS in the Nyquist box $|\omega_{x,y,ct}| \leq \pi$ in spatio-temporal frequency domain.

Table 6-2. A numerical analysis on the suppression of BB (1-4GHz) MC photonically reflected signals on a broadband antenna array propagating at different spatial attenuations

inter-antenna attenuation (σ dB)	attenuation constant (a)	Total energy of the temporal signal	Maximum value of the signal in:		Filtered using 16 band 40th order FIR Cone filter bank with passband angles (ε);					
					20		30		40	
			3D space-time	3D frequency	Energy of filtered output	Suppression %	Energy of filtered output	Suppression %	Energy of filtered output	Suppression %
2	6.29	1	0.1281	5.2776	0.0142	**98.5819**	0.0470	**95.3050**	0.2148	**78.5223**
5	15.73	1	0.2432	4.2703	0.0625	**93.7548**	0.1767	**82.3339**	0.4345	**56.5516**
10	31.47	1	0.3366	4.4225	0.1340	**86.6015**	0.3171	**68.2853**	0.5374	**46.2564**
15	47.20	1	0.3787	3.9767	0.1730	**82.7006**	0.3704	**62.9562**	0.5540	**44.5975**
20	62.94	1	0.4004	3.5973	0.1897	**81.0344**	0.3850	**61.5025**	0.5480	**45.2012**
25	78.67	1	0.4127	3.3304	0.1944	**80.5625**	0.3839	**61.6054**	0.5350	**46.4972**
30	94.41	1	0.4201	3.1429	0.1934	**80.6588**	0.3770	**62.2962**	0.5206	**47.9416**
35	110.14	1	0.4247	3.0073	0.1901	**80.9885**	0.3684	**63.1556**	0.5069	**49.3142**
40	125.88	1	0.4275	2.9063	0.1862	**81.3845**	0.3600	**64.0007**	0.4947	**50.5285**

Fig.6-2 illustrates the overlaid suppression ratio graphs of BB (1-4GHz) MC photonically reflected signals on a broadband antenna array propagating at different spatial attenuations a = [6.29 15.73 31.47 47.20 62.94 78.67 94.41 110.14 125.88] (σ = [2 5 10 15 20 25 30 35 40] dB, $r_0 = T_s = 0.0366m$), simulated at passband angles ε = [20 25 30 35 40].

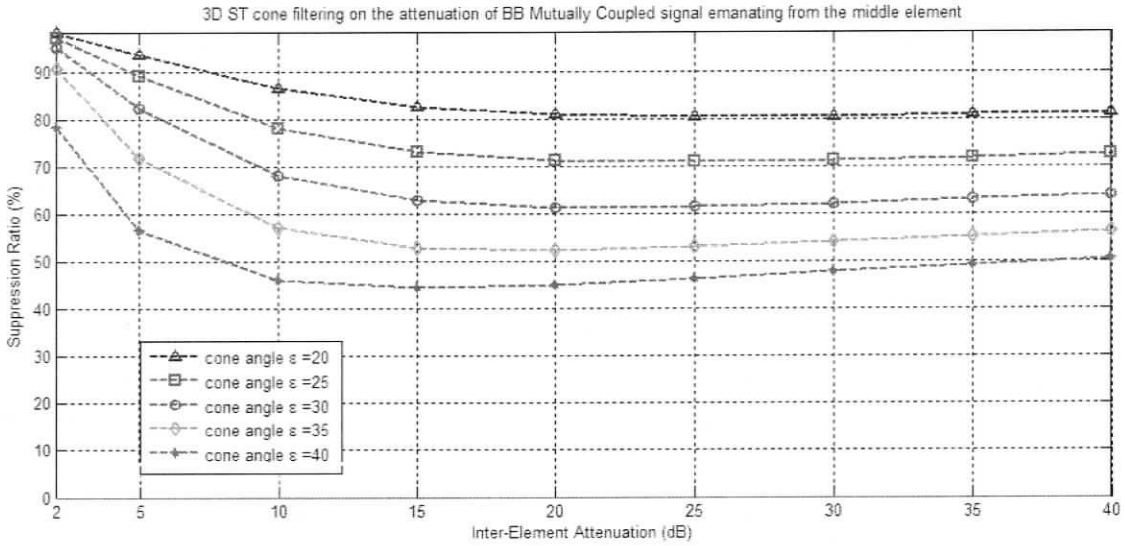

Figure 6-2. The suppression ratio of BB (1-4GHz) MC photonically reflected signals on a broadband antenna array propagating at different spatial attenuations a = [6.29 15.73 31.47 47.20 62.94 78.67 94.41 110.14 125.88] (σ = [2 5 10 15 20 25 30 35 40] dB, $r_0 = T_s = 0.0366m$), graphed at passband angles ε = [20 25 30 35 40]

The results observed in Table 6-2 and Fig.6-2 clearly indicate that high suppression efficiency can be achieved at lower cone angles and at lower inter-antenna attenuation values. This is due to the fact that at lower inter-antenna attenuations (σ <10dB), the ROS of the spectrum of MC signals confine to and around the spectral light cone, and therefore, they can be substantially attenuated by a cone filter that fully encloses the BB MC spectrum in its stopband. Although this is not possible to the same extend at higher inter-antenna attenuations (σ >10dB), a certain level of suppression (>45%) is still observed.

6.3.2 The Suppression of MC LNA Noise Signals

BB(1-4GHz) MC LNA noise signals synthesised as in (6.6) propagating with spatial attenuation constants of a = [6.29 15.73.....125.88] (σ = [2 5 7...36 38] dB, $r_0 = T_s = 0.0366m$) are filtered using $L = 16$ band filter bank structure composed of 2D zero-phase circular symmetric FIR filters of order 40×40 and 1D FIR bandpass filters of order 40 at cone angles of ε = [20 25 30 35 40 41 41.5 42 43].

A numerical summary of the filtering results pertaining to 3D ST cone angles ε = [20 30 40] are illustrated in Table 6-3 and an overlaid graph of suppression ratios at filter passband angles ε = [20 25 30 35 40 41 41.5 42 43] is illustrated in Fig.6-3.

The suppression results of BB MC LNA noise are approximately similar to that observed under the synthetic deterministic BB MC photonically reflected signal in the analysis in sub-section 6.3.1. However, a slightly reduced suppression performance is observed for LNA noise, due to the non-flatness (see Fig.4-18) of the magnitude spectrum of the noise data. The LNA noise coupling reaches a minimum suppression ratio (at σ =15dB suppression ratio is 34.6438% for cone angle ε =40) and increases to higher suppression ratios as σ increases similar to photonically reflected MC signals.

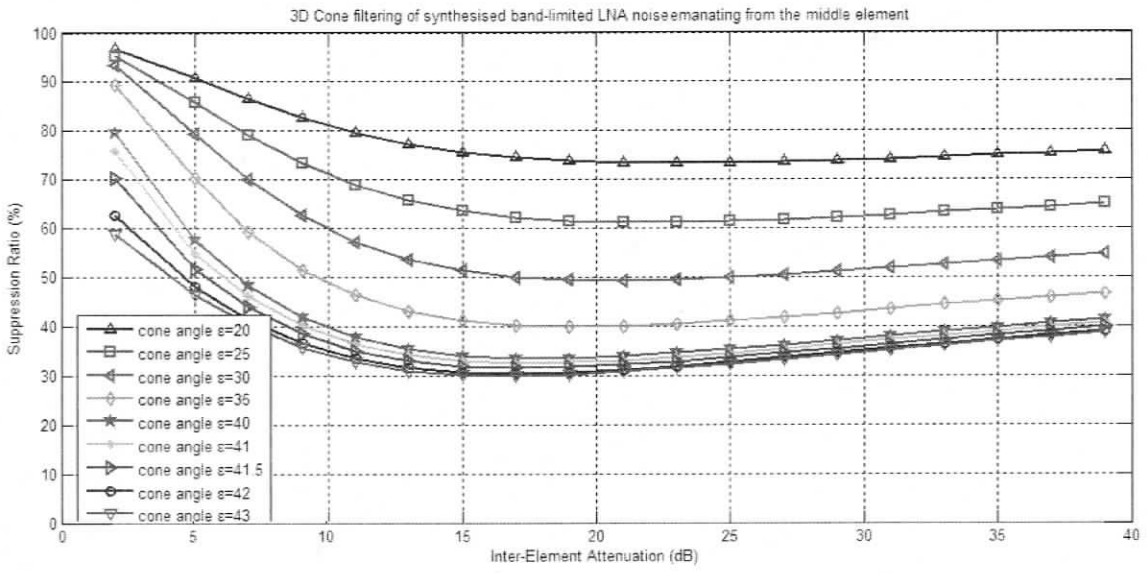

Figure 6-3. The suppression ratio of MC LNA noise on a broadband(1-4GHz) antenna array propagating at different spatial attenuations a = [6.29 15.73.....125.88] (σ = [2 5 7...36 38] dB, $r_0 = T_s = 0.0366m$), graphed at passband angles ε = [20 25 30 35 40 41 41.5 42 43]

Table 6-3. A numerical analysis on the suppression of BB LNA Noise signals propagating at different spatial attenuations on a broadband (1-4GHz) antenna array

inter-antenna attenuation (σ dB)	attenuation constant (a)	Total energy of the temporal signal	Value of the maximum component		Filtered using 16 band 40th order FIR Cone filter bank with passband angles (ε);					
					20		30		40	
			3D space-time	3D frequency	Energy of filtered output	Suppression %	Energy of filtered output	Suppression %	Energy of filtered output	Suppression %
2	6.29	1	0.0915	5.3122	0.0067	**99.3306**	0.0195	**98.0539**	0.0563	**94.3665**
5	15.73	1	0.1683	3.9806	0.0324	**96.7556**	0.0888	**91.1191**	0.2135	**78.6493**
10	31.47	1	0.2329	4.4578	0.0783	**92.1679**	0.1952	**80.4792**	0.3807	**61.9284**
15	47.20	1	0.2620	4.4595	0.1072	**89.2804**	0.2514	**74.8578**	0.4422	**55.7831**
20	62.94	1	0.2770	4.2448	0.1210	**87.8973**	0.2740	**72.5987**	0.4585	**54.1477**
25	78.67	1	0.2856	4.0324	0.1259	**87.4094**	0.2797	**72.0319**	0.4571	**54.2916**
30	94.41	1	0.2907	3.8583	0.1262	**87.3785**	0.2777	**72.2304**	0.4490	**55.1030**
35	110.14	1	0.2938	3.7206	0.1245	**87.5506**	0.2727	**72.7287**	0.4390	**56.1041**
40	125.88	1	0.2958	3.6121	0.1221	**87.7923**	0.2670	**73.3027**	0.4291	**57.0866**

The numerical results in sub-section 6.2 indicate successful mitigation of BB RFI using the ST filtering approach whereas for BB MC signals analysed in sub-section 6.3, the suppression is observed to be dependent on the inter-antenna attenuation σ and cone passband angle ε. For both signal types BB RFI and BB MC however, the suppression ratio improves at lower cone passband angles. Therefore, it can be concluded that the proposed ST filtering method can be successfully employed on the suppression of both BB RFI and BB MC signals, provided that the ST cone angles can be chosen appropriately.

However, it is important to investigate the suppression performance of BB RFI and ST MC signals in the presence of SOIs, since it is essential that the SOIs undergo minimal distortion by the employed 3D ST cone filter. This requirement implies that the filter passband angle ε must be chosen to enclose the ROS of the BB SOI spectrum within the ST filter passband and thus lead to a lower limit for the selection of a suitable cone angle ε.

6.4 A Simulation Illustration on the Filtering of BB SOI in the Presence of BB RFI and BB MC Signals

In order to illustrate the ST filtering operation of BB SOI in the presence of interference (such as BB RFI and BB MC signals), consider a simplistic signal composition scenario on an AA, comprised of BB SOI, BB RFI and photonically reflected MC signals as illustrated in Fig.6-4. The BB(1-4GHz) MC signal w_{MC} is assumed to propagate with inter-antenna attenuation of σ = 2dB. Such a scenario is selected only for the purpose of visual illustration of the filtering operation, since σ is higher in most practical BB antenna arrays. BB (1GHz-4GHz) RFI w_{RFI} is synthesised as in (6.2) by ST-PWs having spatial DOAs given by (θ_1,ϕ_1)=(85,80) (PW-1) and (θ_2,ϕ_2) =(90,110) (PW-2). The BB SOI w_{SOI} is assumed to be a broadside ST-PW $(\theta=0)$ and, therefore, the ROS of its spectrum would form a line spectrum along the temporal frequency axis ω_{ct}. Consequently, a cone filter of cone passband angle ε=20 is chosen such that it completely encompass the BB SOI in its passband.

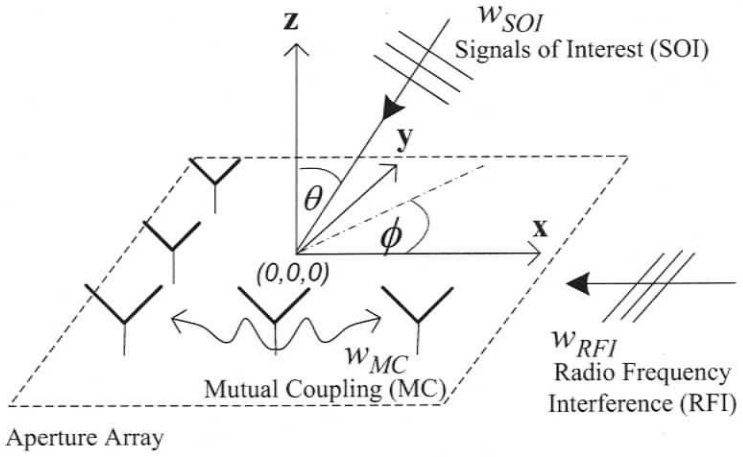

Figure 6-4 Illustration of broadband (BB) signal of interest (SOI), BB radio frequency interference (RFI) and photonically reflected MC signals on a dense aperture array (AA)

The ST filter with the chosen passband angle is employed on the synthesised signals and the illustration of the filtering approach with the aid of 3D and 2D figures in space-time and spatio-temporal frequency domains is illustrated here.

The ROS of all three types of signals in the 3D space-time within $|n_{x,y,ct}| \leq 40$ are illustrated in Fig.6-5. A surface plot shown in Fig.6-5(a) clearly indicates how the ST-PWs are being incident on the AA over time and the emanation of mutual coupling from the middle element. A contour plot sliced at $n_{ct} = 26$ shown in Fig.6-5(b) is a birds-eye view of the AA to illustrate the incidence of over-the-horizon low azimuth RFI signals and the propagation of mutual coupling from the middle element at time $n_{ct} = 26$.

The ROS of these signals in the spatio-temporal frequency domain is illustrated in Fig.6-6. In the surface plot shown in Fig.6-6(a), the line spectra of the two BB RFI signals (PW-1 and PW-2) are not clearly visible as they are overlapped with the ROS of the mutual coupling spectrum. The line spectrum of the BB SOI however, is clearly visible as it lies along ω_{ct} axis.

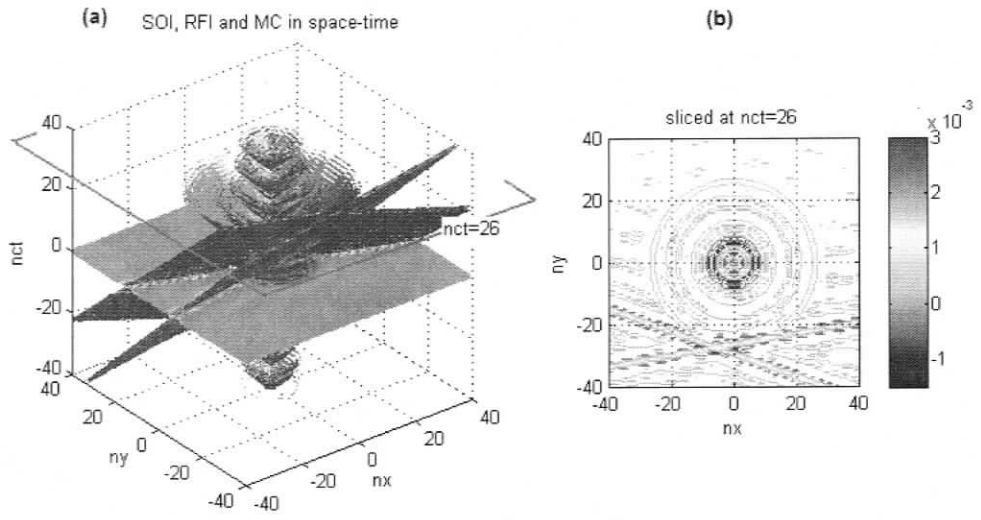

Figure 6-5. ROS in space-time domain, of MC, SOI, PW1 and PW2 (a) 3D, containing 82% of energy (b) 2D contour plot sliced at $n_{ct} = 26$

It is evident that, by employing a suitable ST filter that encloses the line spectrum of the BB SOI in its passband, it is possible to recover the BB SOI while suppressing the BB RFI and BB mutual coupling. A contour plot, sliced at $\omega_{ct} = 2.0813$ shown in Fig.6-6(b) further verifies the relative locations of the ROSs of the signals implying that they are separable. At lower ω_{ct} the seperability of these signals is reduced.

A ST filter with a cone passband angle of ε=20 is designed using the proposed filter bank structure in Chapter-5 with $L = 16$ bands comprised of 2D zero-phase circular symmetric FIR filters of order 40×40 and 1D FIR bandpass filters of order 40. A 3D surface plot of the of the magnitude response of the cone filter is illustrated in Fig.6-7(a) along with a contour plot sliced at $\omega_{ct} = 2.0813$ in Fig.6-7(b) and another contour plot sliced at $\omega_y = 0$ in Fig.6-7(c). A comparison of Fig.6-7(b) and Fig.6-6(b) indicates that the designed cone filter is capable of filtering the BB SOI while suppressing the BB RFI and BB MC signals.

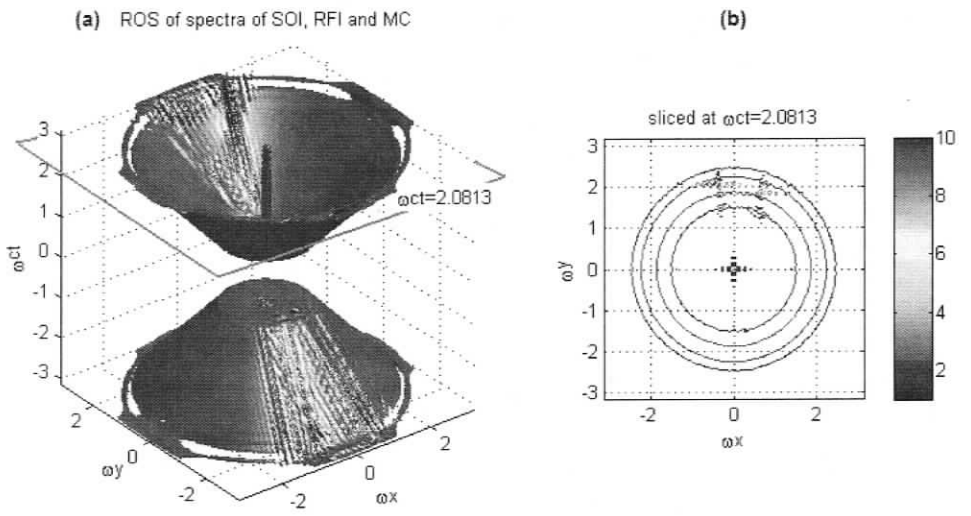

Figure 6-6. ROS in the 3D spatio-temporal frequency domain of SOI, mutual coupling, PW1 and PW2 (a) 3D, containing 68% of energy (b) 2D contour plot, sliced at $\omega_{ct} = 2.0813$.

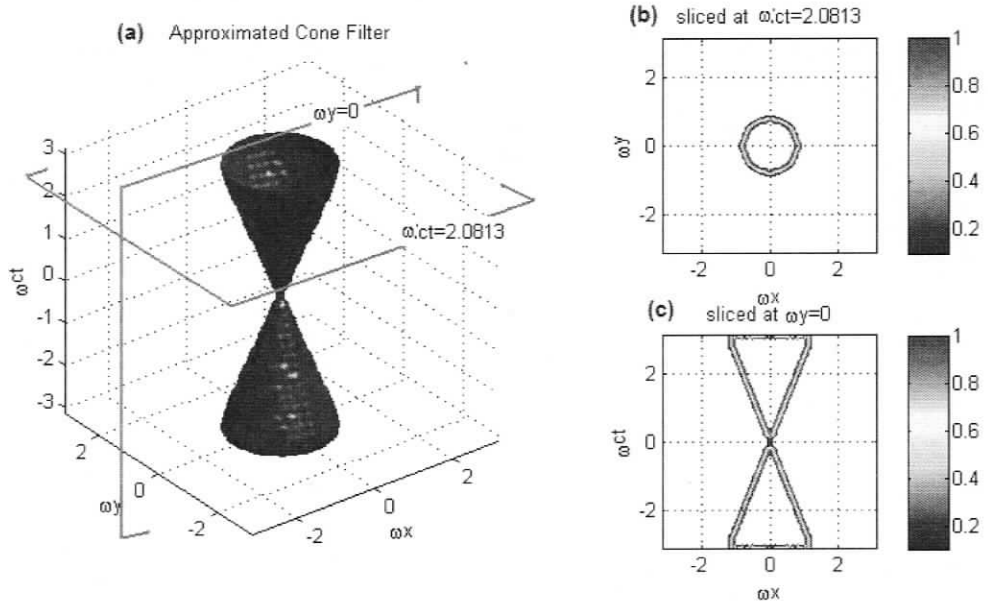

Figure 6-7 Cone passband approximation by $L = 16$ band filter bank structure composed of 2D zero-phase circular symmetric FIR filters of order 40×40 and 1D FIR bandpass filters of order 40 (a) Surface plot of -3dB (b) contour plot sliced at $\omega_{ct} = 2.0813$ (c) contour plot sliced at $\omega_y = 0$

The SOI contaminated with BB RFI and BB MC signals as shown in Fig.6-6 is filtered using the proposed 3D ST filter shown in Fig.6-7. The successful recovery of the SOI is clearly illustrated in Fig.6-8(b) which is the ROS of the filtered output in 3D space-time. The filtered output in the 3D spatio-temporal frequency domain is shown Fig.6-8(a). The

spectral components observed at low frequencies are the leakages of spectral components of BB RFI and BB MC signal due to the lower separability of the signals at low frequencies. A ST filter with a high selectivity at lower frequencies can be employed to minimise such effects.

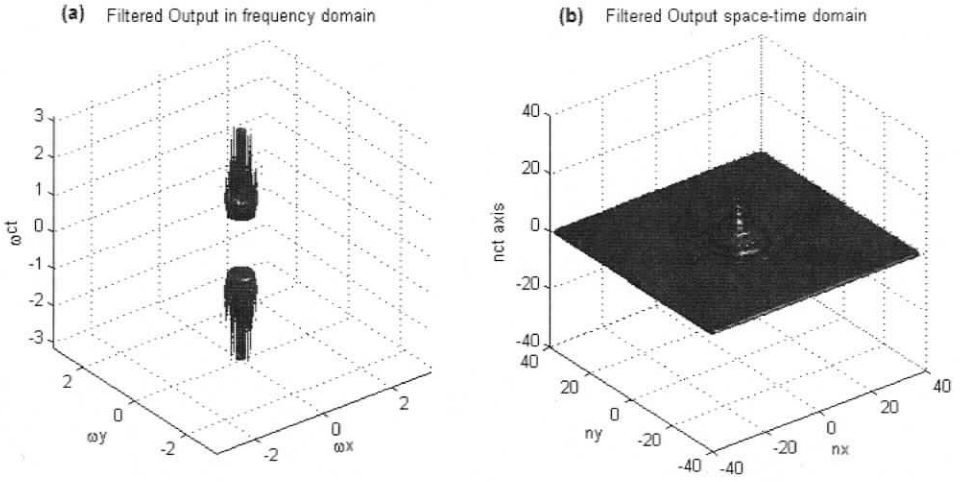

Figure 6-8. Filtering of SOI contaminated with BB RFI and BB MC signals (a) ROS of the output in 3D frequency domain, containing 78% of energy (b) ROS of the output in space-time, containing 83% of energy

6.5 A Numerical Analysis of the 3D ST Performance on the Filtering of BB SOI in the Presence of BB RFI, BB MC signals

In practical applications of AAs the BB SOIs may arrive at the array from a span of sky angles, while BB RFIs may arrive from directions that do not fall in to the range of SOI. For these reasons the ROS of all SOIs and RFIs in the 3D requency domain would fill up the spectral light cone. Furthermore, the BB MC signals encompassing photonically reflected signals as well as internally generated LNA noise propagating at higher inter-antenna attenuations levels would result in a smeared ROS inside and outside of the spectral light cone in the 3D frequency domain. The combination of all these BB ST signals on AAs would result in a ROS in the 3D frequency domain spread in the complete Nyquist box $|\omega_{x,y,ct}| \leq \pi/2$ in contrast to clearly separable ROSs as observed in Fig.6-6. The BB SOIs on the FPAs are not PWs, but the final ROS of the composite BB ST signals on FPAs would also be spread in the complete Nyquist box, similarly to the

AA case. It is, therefore, difficult to illustrate the 3D ST filtering operation of a practical application of AA/FPA using simulation figures as shown in sub-section 6.4. Instead, we define a numerical metric, *signal to interference ratio (SIR)* to evaluate the proposed filtering performance. The SIR is calculated as,

$$Input/Output\ SIR = 10\log_{10}\left[\frac{\sum_k\sum_j\sum_i \left|SOI_{input/output}(i,j,k)\right|^2}{\sum_k\sum_j\sum_i \left|IFR_{input/output}(i,j,k)\right|^2}\right] \tag{6.7}$$

where $IFR_{input/output} = BB\ RFI + BB\ MC\ photonic + BB\ MC\ LNA\ Noise$. One of the implied requirements for employing digital filtering approaches on to radio astronomical signals is that the filter passband should be selected such that it would not degrade the SOI. Thus, the SOI is always assumed to be well inside the passband of the cone filter in the following experiments.

6.5.1 A Numerical Analysis on the Performance of 3D ST Filtering on AAs

The composition of the ST signals is chosen as in Table 6-4. Two BB RFI signals are included to represent the energy of all external interferences arriving at over-the-horizon DOA $(\theta = 90, \phi = 10)$ as well as from low-azimuth DOA $(\theta = 85, \phi = 80)$. In order to represent BB SOIs of all sky obervations, a single broadside BB SOI $(\theta = 0)$ containing normalised energy of 0.01, is included to guarantee that the ROS of the BB SOI is well inside the passband of the ST filter (maintaining initial SIR of the system to be -26dB approximately).

Table 6-4. Signal composition scenario-1 *(Strong RFI Conditions)* of BB ST signals incident on AAs for the analysis of the Signal to Interference Ratio (SIR)

Signal Composition		
Signal Type		Energy
BB SOI (a ST PW) $(\theta = 0)$		0.01
BB RFI	$(\theta = 85, \phi = 80)$	1
	$(\theta = 90, \phi = 10)$	1
BB ST MC	Photonically Reflected	1
	LNA Noise	1

The BB MC photonically reflected signals are assumed to have been induced from these BB RFI and/or BB SOI signals. The energy of BB ST MC signals, (photonically reflected as well as internally generated LNA noise), represents the total mutual coupling energy emanating from all array elements.

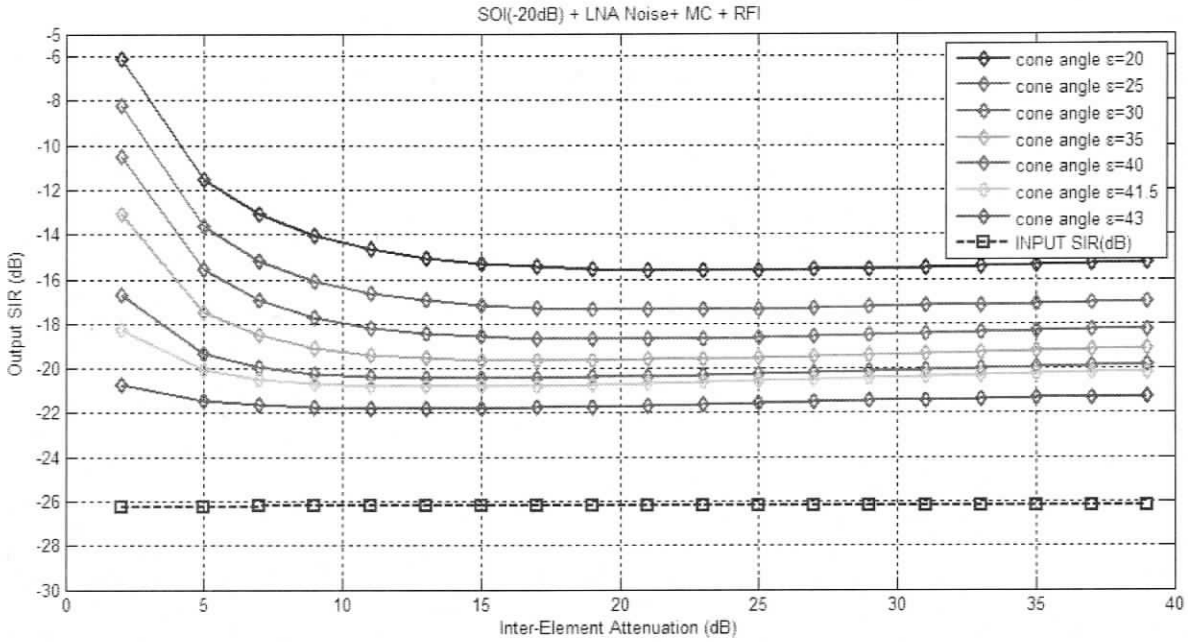

Figure 6-9. Output SIR of the signals in Table 6-4 against inter-antenna attenuation σ dB, after employing a $L=16$ band filter bank structure composed of 2D zero-phase circular symmetric FIR filters of order 40×40 and 1D FIR bandpass filters of order 40, overlaid for cone angles of $\varepsilon=$ [20 25 30 35 40 41.5 43]

The BB ST signals with a composition as in Table 6-4 are filtered using a $L=16$ band filter bank structure composed of 2D zero-phase circular symmetric FIR filters of order 40×40, and 1D FIR bandpass filters of order 40 with cone angles of $\varepsilon=$ [20 25 30 35 40 41.5 43]. In Fig.6-9 the SIR of the output for different spatial attenuations a = [6.29 15.73.....125.88] ($\sigma=$ [2 5 7...36 38] dB, $r_0 = T_s = 0.0366m$) is shown. The results show approximately 4dB improvement of SIR at the highest cone angle $\varepsilon=$ 43 for σ>10dB and, as the cone angle reduces, the SIR improves at lower inter-antenna attenuations as expected. For example, with inter-antenna attenuation σ=2dB and cone-angle $\varepsilon=20$, the improvement of SIR is approximately 20dB.

Table 6-5. Signal composition scenario-2 *(Dominant LNA Noise Conditions)* of BB ST signals incident on AAs for the analysis of the Signal to Interference Ratio (SIR)

Signal Composition		
Signal Type		Energy
BB SOI (a ST PW) $(\theta = 0)$		0.01
BB RFI	$(\theta = 85, \phi = 80)$	0.1
	$(\theta = 90, \phi = 10)$	0.1
BB ST MC	Photonically Reflected	0.1
	LNA Noise	1

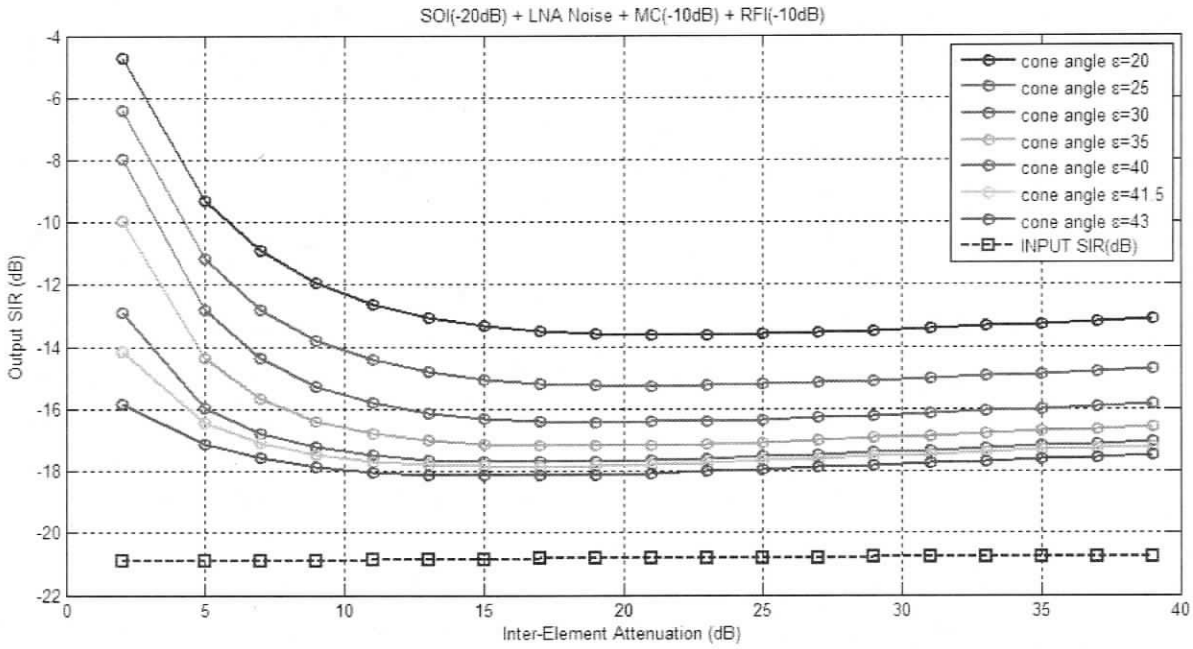

Figure 6-10. Output SIR of the signals in Table 6-5 against inter-antenna attenuation σ dB, after employing a $L = 16$ band filter bank structure composed of 2D zero-phase circular symmetric FIR filters of order 40×40 and 1D FIR bandpass filters of order 40, overlaid for cone angles of $\varepsilon =$ [20 25 30 35 40 41.5 43]

A different signal composition scenario is chosen to emphasise the LNA noise coupling effect by reducing the energy of BB RFI, and BB MC photonically reflected signals down to -10dB as shown in Table 6-5. Fig.6-10 illustrates the output SIR of the signals for different spatial attenuations a = [6.29 15.73.....125.88] (σ = [2 5 7...36 38]

dB, $r_0 = T_s = 0.0366m$) after employing a $L = 16$ band filter bank structure composed of 2D zero-phase circular symmetric FIR filters of order 40×40, and 1D FIR bandpass filters of order 40 with cone angles of ε = [20 25 30 35 40 41.5 43]. It is evident from the results, that an approximately 3dB improvement of SIR can be achieved at a cone filter angle of ε = 43 and inter-antenna attenuation levels of σ>15dB. As the cone angle reduces the SIR improves at lower inter-antenna attenuations as expected. For example, the SIR is improved up to approximately 12dB by employing a narrow angle cone filter of ε = 20 and for σ=5dB.

6.5.2 A Numerical Analysis on the Performance of 3D ST Filtering on FPAs

Signal composition scenarios discussed under AAs in sub-section 6.5.1 are also investigated for FPAs. The BB SOI, however, is no longer considered as a ST-PW that has a ROS of the spectrum along the temporal frequency axis. In order to synthesise the BB SOI on the FPAs, a synthesised broadside BB (1-4GHz) SOI (as in (6.1)) incident on the parabolic reflector of diameter D=64m, and focal ratio F/D=0.41 focusing on to a FPA of size $(2N_x + 1) \times (2N_y + 1) = 81 \times 81$ elements with inter-element distance of 0.036m ($\lambda/2$ corresponding to 4.1GHz), is considered. The physical spill-over angle of the parabolic antenna set-up is calculated to be θ_{spill}=62.75 (corresponding space-time angle of 41.63). The field distribution on the FPA is simulated using UC-FPFC as discussed in Chapter-3, sub-section 3.6. In contrast to BB SOI on AAs, the BB SOI incident on the FPA forms a cone shaped solid region as its ROS in the 3D spatio-temporal frequency domain. Hence, the BB SOI employed in the following simulations has a ROS equivalent to a solid cone with an angle approximated in the range 41.95^0-43^0 as illustrated in Fig.3.15 in Chapter-3. For this reason, in the following simulations we analyse SIR performance for ST cone filter passband angles of ε = [40 40.5 41 41.5 42 42.5 43 43.5 44 44.5 45]. Cone filters with narrower passband angle would distort the SOI, and thus are not of interest.

The output SIR of the signals in Table 6-6 for different spatial attenuations a = [6.29 15.73.....125.88] (σ = [2 5 7...36 38] dB, $r_0 = T_s = 0.0366m$), after employing the proposed cone filter bank with cone angles of ε = [40 40.5 41 41.5 42 42.5 43 43.5 44 44.5 45] is

illustrated in Fig.6-11. As the employed ST cone filter angle is reduced, the SOI tends to leak in to the stopband of the filter while the BB RFI and BB MC signals suppression tends to improve. Due to this trade-off at cone filter angles of ε = [40 40.5 41 41.5] the output SIR remains approximately similar, as can be observed in Fig.6-11. An increase of the ST cone passband angle above $\varepsilon > 41.5$ allows more BB RFI and BB MC signals to come through, leading to reduced SIR as evident in Fig.6-11.

Table 6-6. Signal composition scenario-1 *(Strong RFI Conditions)* of BB ST signals incident on FPAs for the analysis of the Signal to Interference Ratio (SIR)

Signal Composition		
Signal Type		Energy
BB SOI (Not a PW) $(D = 64, F/D = 0.41)$		0.01
BB RFI	$(\theta = 85, \phi = 80)$	1
	$(\theta = 90, \phi = 10)$	1
BB ST MC	Photonically Reflected	1
	LNA Noise	1

At a ST filter cone angle of ε=45 (where the passband to stopband transition boundary is on the spectral light cone), the improvement of the SIR is observed to be approximately 2dB for all σ. By employing a ST cone filter with a passband angle of ε = 40, an approximately 5dB improvement of SIR can be achieved for inter-antenna attenuation levels of σ>15dB.

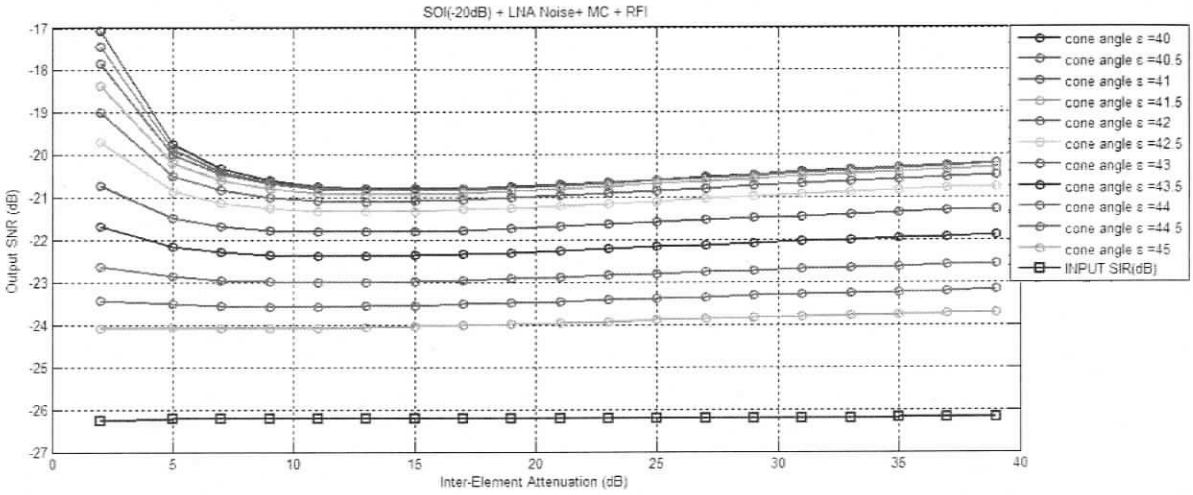

Figure 6-11. Output SIR of the signals in Table 6-6 against inter-antenna attenuation σ dB, after employing $L=16$ band filter bank structure composed of 2D zero-phase circular symmetric FIR filters of order 40×40 and 1D FIR bandpass filters of order 40 , overlaid for cone angles of ε = [40 40.5 41 41.5 42 42.5 43 43.5 44 44.5 45]

Table 6-7. Signal composition scenario-2 *(Dominant LNA Noise Conditions)* of BB ST signals incident on FPAs for the analysis of the Signal to Interference Ratio (SIR)

Signal Composition		
Signal Type		Energy
BB SOI (Not a PW) $(D=64, F/D=0.41)$		0.01
BB RFI	$(\theta=85, \phi=80)$	0.1
	$(\theta=90, \phi=10)$	0.1
BB ST MC	Photonically Reflected	0.1
	LNA Noise	1

A different signal composition scenario as shown in Table 6-7 is incorporated to emphasise on the LNA noise coupling whereas the effect of BB RFI and BB MC photonically reflected signals is degraded by reducing their energy contribution down to -10dB. Fig. 6-12 illustrate the overlaid output SIR of the signals against different spatial attenuations a = [6.29 15.73.....125.88] (σ = [2 5 7...36 38] dB, $r_0 = T_s = 0.0366m$) by employing a $L=16$ band filter bank structure composed of 2D zero-phase circular symmetric FIR filters of order 40×40 and 1D FIR bandpass filters of order 40 with cone

angles of ε = [40 40.5 41 41.5 42 42.5 43 43.5 44 44.5 45]. It is evident from the results, that at least a 2dB improvement in the SIR can be achieved. As the cone angle is reduced the behaviour of output SIR at a given σ is similar to that of Fig.6-11. Due to the dominant contribution of LNA noise coupling in the input signal, the output SIR illustrated in Fig.6-12 tends to show the behaviour of LNA noise coupling suppression illustrated in Fig.6-3.

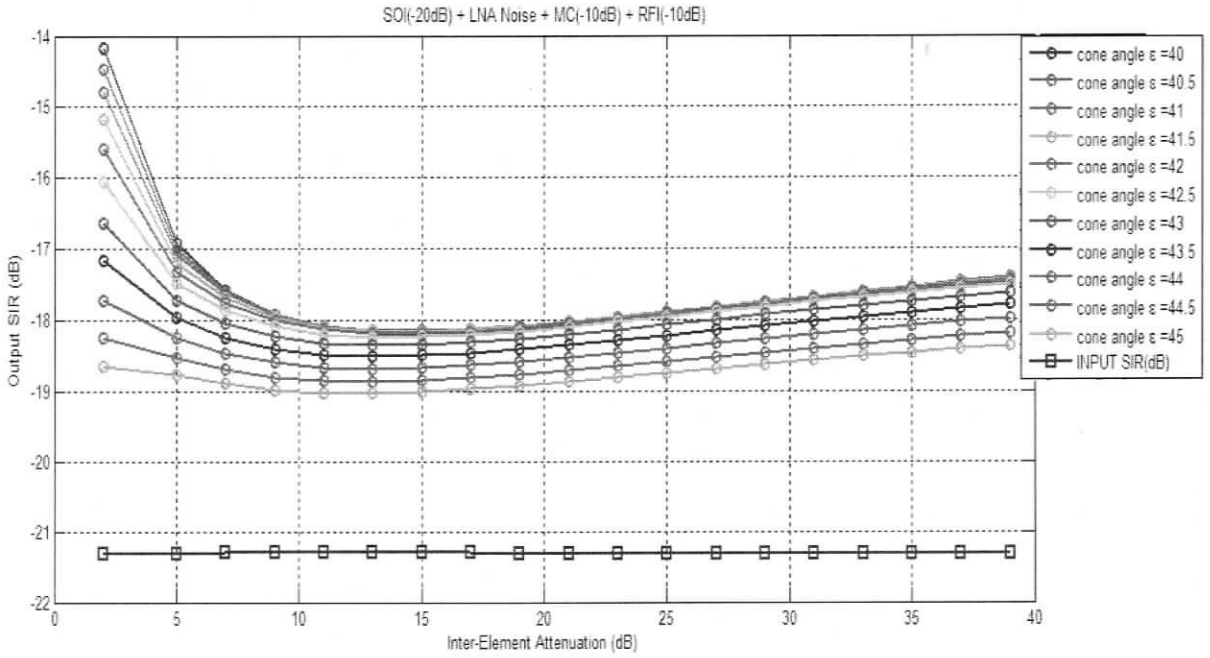

Figure 6-12. Output SIR of the signals in Table 6-7 against inter-antenna attenuation σ dB, after employing a $L = 16$ band filter bank structure composed of 2D zero-phase circular symmetric FIR filters of order 40×40 and 1D FIR bandpass filters of order 40, overlaid for cone angles of ε = [40 40.5 41 41.5 42 42.5 43 43.5 44 44.5 45]

6.6 Additional Simulation Results

In the above simulations the MC signals are synthesised for an operational band of 1-4GHz with a propagation speed of the speed of light c. In this sub-section we investigate the suppression performance of MC signals for two distinct bands i.e. 0.7-2GHz (broadband) and 1.25-1.55GHz (narrowband), that propagate at lower propagation speeds such as $3c/4$ and $c/2$.

6.6.1 The Effect of the Inter-Antenna Intra-Plane Propagation Speed of BB MC Signals on the Suppression Performance

Consider a $(2N_x+1)\times(2N_y+1)=81\times81$ element rectangularly-distributed uniformly-weighted BB antenna array which has an operational bandwidth of 0.7-2GHz. The temporal variation $\overline{w}(.)$ of the band-limited BB MC signal, is synthesised as in (6.1) where $f_{k_{MAX}}=2GHz$ is the maximum frequency with $\mathbf{f}=[0.7,0.722,0.743...2]GHz$. Assuming that the speed of light is $c=0.3Gm/s$, the corresponding slightly over-sampled $f_{k_{MAX}}=4.2GHz$ spatio-temporal sampling distances are chosen to be, $T_{x,y,ct}=T_s=\frac{1}{f_s}==0.0714m$. The 3D spatio-temporal frequency domain representation of the emulated BB (0.7-2GHz) MC ST signal emanating from the middle element propagating at the speed of light c with an attenuation constant of $a=3.22$ ($\sigma=2dB$, $r_0=T_s=0.0714m$) is illustrated in Fig.6-13.

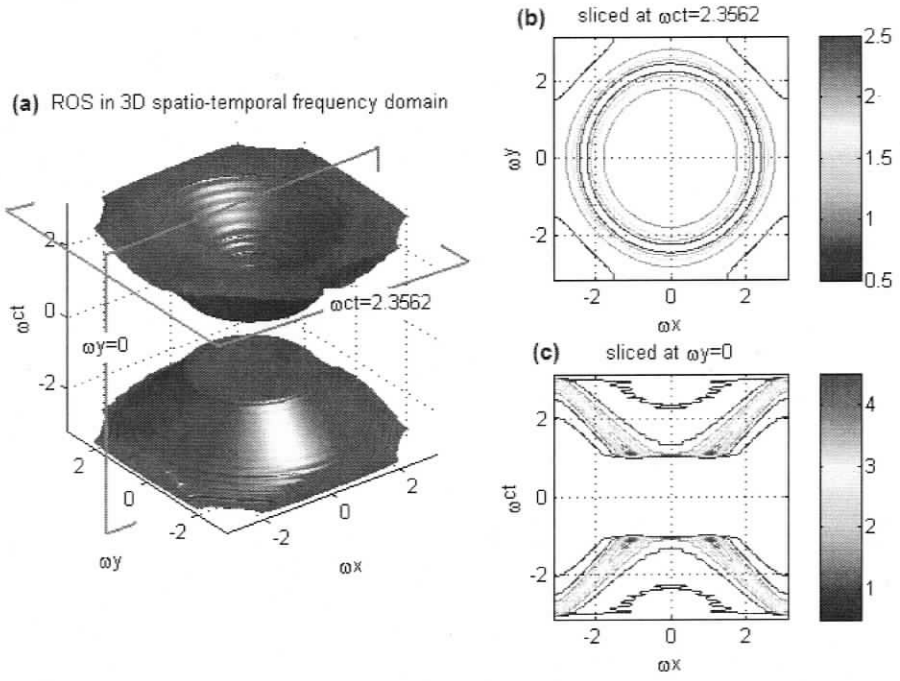

Figure 6-13. 3D spatio-temporal frequency domain representation of emulated BB (0.7-2GHz) MC ST signal emanating from the middle element propagating at the speed of light c with an attenuation constant of $a = 3.22$ ($\sigma = 2dB$, $r_0 = T_s = 0.0714m$) (a) the 3D ROS that contains 89% of the signal energy (b) a 2D contour plot sliced at $\omega_{ct} = 2.3562$ (c) a 2D contour plot sliced at $\omega_y = 0$

The emulated BB MC signals propagating at the speed of light c with spatial attenuation constants of a = [3.22 8.06 16.12 24.18 32.24 40.29 48.35 56.41 64.47] (σ = [2 5 10 15 20 25 30 35 40] dB, $r_0 = T_s = 0.0366m$) are then filtered using a $L = 16$ band filter bank structure composed of 2D zero-phase circular symmetric FIR filters of order 40×40 and 1D FIR bandpass filters of order 40 at cone angles of ε = [20 25 30 35 40 41 41.5 42 43]. The overlaid suppression ratio graphs simulated at passband angles ε = [20 25 30 35 40 41 41.5 42 43] is shown in Fig.6-14.

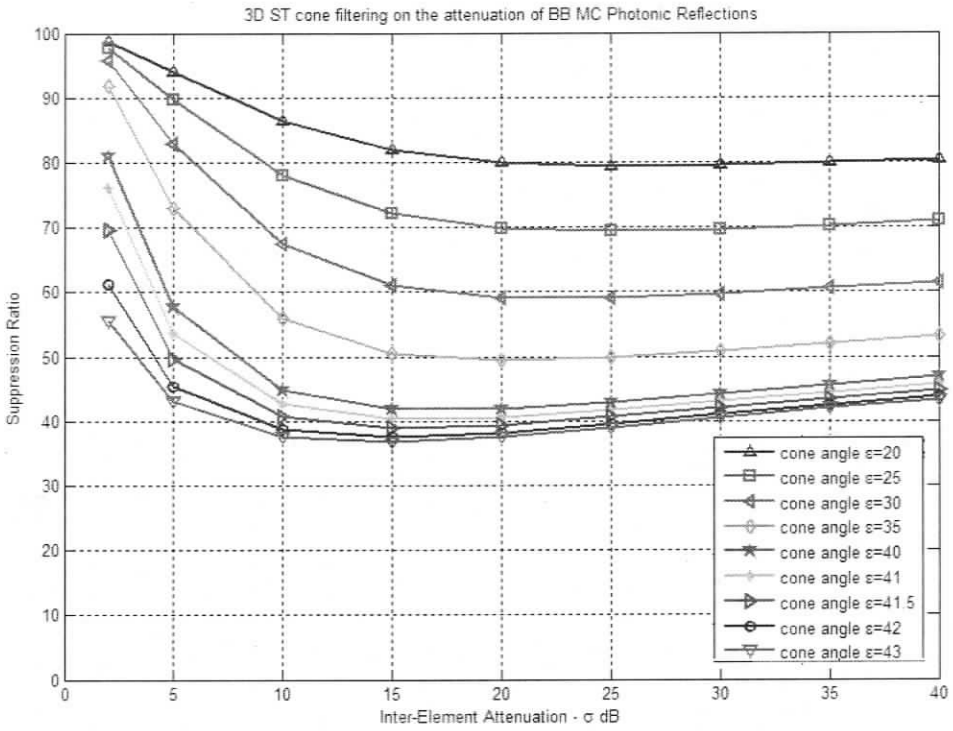

Figure 6-14. The suppression ratio of BB (0.7-2GHz) MC photonically reflected signals on a broadband antenna array propagating at the speed of light c with spatial attenuations a = [3.22 8.06 16.12 24.18 32.24 40.29 48.35 56.41 64.47] (σ = [2 5 10 15 20 25 30 35 40] dB, $r_0 = T_s = 0.0714m$), filtered by 3D ST cone filters of passband angles ε = [20 25 30 35 40 41 41.5 42 43]

The 3D spatio-temporal frequency domain representation of the emulated BB (0.7-2GHz) MC ST signal emanating from the middle element propagating at a speed of $3c/4$ and $c/2$ with an attenuation constant of $a = 3.22$ ($\sigma = 2dB$, $r_0 = T_s = 0.0714m$) is illustrated in Fig.6-15. As it is evident from the figure lowering the propagation speed will scale the ROS along the temporal frequency axis resulting to a drift of the ROS towards the exterior of the spectral light cone. For this reason, better suppression ratios can be expected for lower speed of propagation in comparison to the results presented in Fig.6-14.

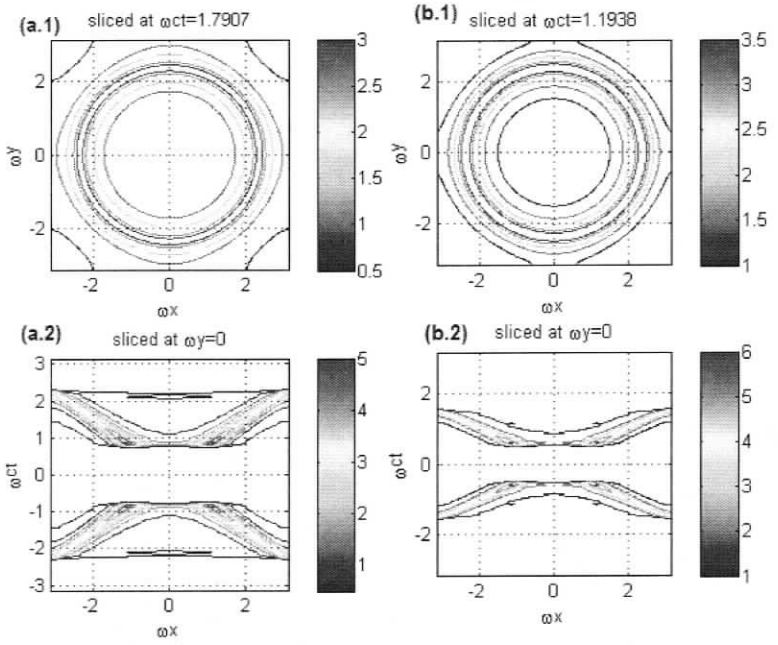

Figure 6-15. 3D spatio-temporal frequency domain representation of emulated BB (0.7-2GHz) MC ST signal emanating from the middle element with an attenuation constant of $a = 3.22$ ($\sigma = 2dB$, $r_0 = T_s = 0.0714m$): propagating at a speed of $3c/4$ (a.1) a 2D contour plot sliced at $\omega_{ct} = 1.7907$ (a.2) a 2D contour plot sliced at $\omega_y = 0$: and propagating at a speed of $c/2$ (b.1) a 2D contour plot sliced at $\omega_{ct} = 1.1938$ (b.2) a 2D contour plot sliced at $\omega_y = 0$

The emulated BB (0.7-2GHz) MC signals propagating at a speed of $3c/4$ and $c/2$, with spatial attenuation constants of a = [3.22 8.06 16.12 24.18 32.24 40.29 48.35 56.41 64.47] (σ = [2 5 10 15 20 25 30 35 40] dB, $r_0 = T_s = 0.0366m$) are then filtered using a $L = 16$ band filter bank structure composed of 2D zero-phase circular symmetric FIR filters of order 40×40 and 1D FIR bandpass filters of order 40 at cone angles of ε = [20 25 30 35 40 41 41.5 42 43]. Fig.6-16 illustrates the overlaid suppression ratio graphs simulated at passband angles ε = [20 25 30 35 40 41 41.5 42 43] for emulated BB MC signals propagation at speeds $3c/4$ and $c/2$. As expected, it is evident from the figures that the suppression performance will improve at lower propagations speeds.

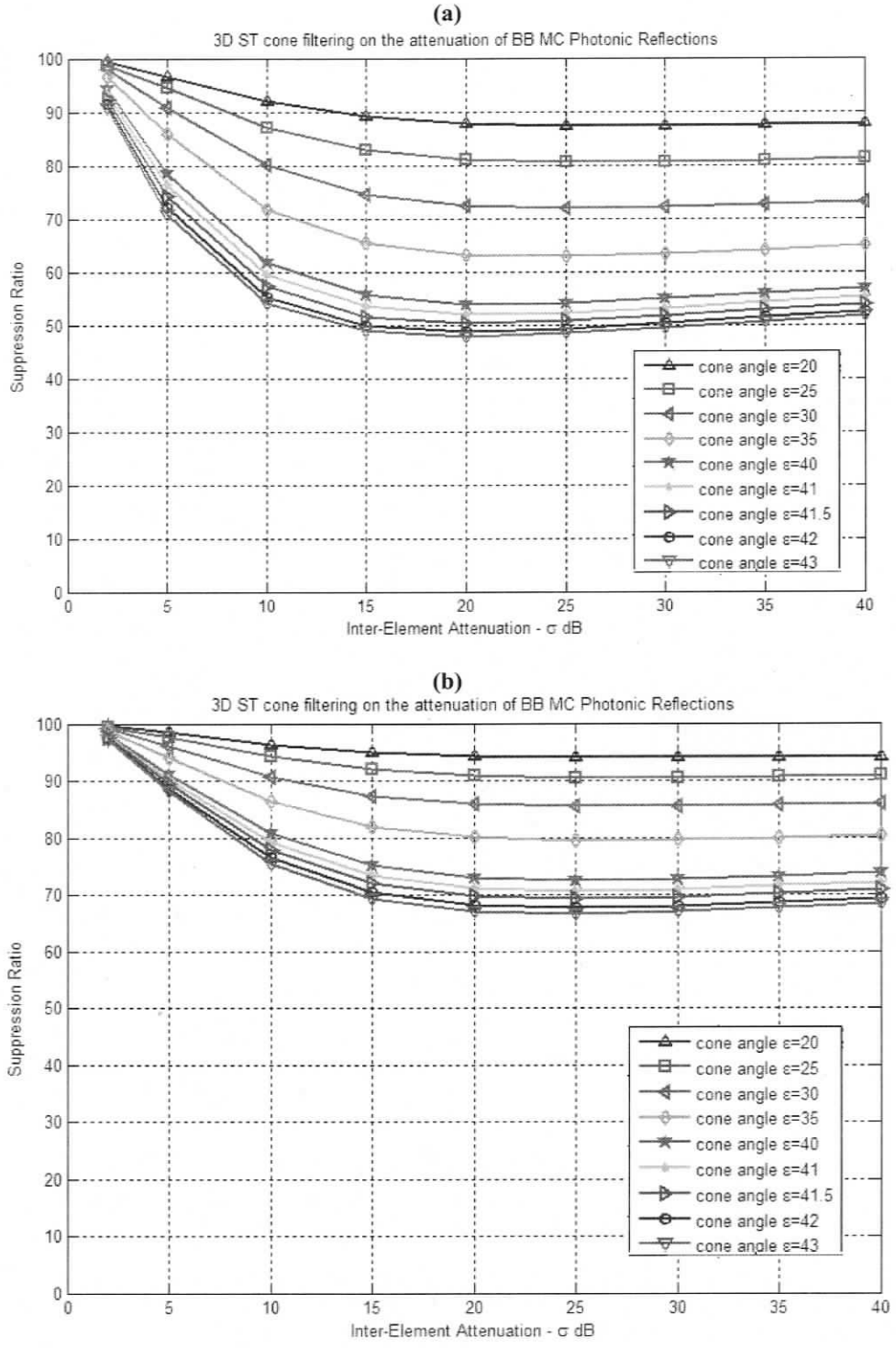

Figure 6-16. The suppression ratio of BB (0.7-2GHz) MC photonically reflected signals on a broadband antenna array propagating at a speed of (a) $3c/4$ and (b) $c/2$:- for attenuations a = [3.22 8.06 16.12 24.18 32.24 40.29 48.35 56.41 64.47] (σ = [2 5 10 15 20 25 30 35 40]dB, $r_0 = T_s = 0.0714m$), filtered by 3D ST cone filters of passband angles ε = [20 25 30 35 40 41 41.5 42 43]

6.6.2 The Suppression of Narrow-Band (NB) MC Signals

In the following simulations a narrow-band (NB) MC signal of bandwidth 300MHz is synthesised with a maximum frequency of $f_{k_{MAX}} = 1.55GHz$ and $\mathbf{f} = [1.25,1.265,1.28....1.55]GHz$ as in (6.1). The antenna array under consideration is a $(2N_x+1)\times(2N_y+1) = 81\times 81$ element rectangularly-distributed uniformly-weighted array that has an operational bandwidth of 1.25-1.55GHz Assuming that the speed of light is $c = 0.3Gm/s$, the corresponding slightly over-sampled $(3.3GHz)$ spatio-temporal sampling distances are chosen to be, $T_{x,y,ct} = T_s = \frac{1}{f_s} == 0.0909m$. The 3D spatio-temporal frequency domain representation of the emulated NB (1.25-1.55GHz) MC ST signal emanating from the middle element propagating at speeds of c, $3c/4$ and $c/2$, with an attenuation constant of $a = 3.22$ ($\sigma = 2dB$, $r_0 = T_s = 0.0909m$) are illustrated in Figs.6-17, and 6-19 respectively.

The emulated BB MC signals propagating at speeds c, $3c/4$ and $c/2$, for spatial attenuation constants of a = [2.53 6.33 12.66 18.99 25.33 31.66 37.99 44.32 50.66] (σ =[2 5 10 15 20 25 30 35 40] dB, $r_0 = T_s = 0.0909m$) are then filtered using tri-band, dual-band and single-band filter bank structures respectively. Each sub-band is composed of 2D zero-phase circular symmetric FIR filters of order 40×40 and 1D FIR bandpass filters of order 40. The overlaid suppression ratio graphs simulated at passband angles ε = [20 25 30 35 40 41 41.5 42 43] at propagation speeds of c, $3c/4$ and $c/2$, are illustrated in Figs.6-18, and 6-20 respectively. From the graphs, it is clearly evident that at lower speeds of propagation, the suppression performance of NB MC signals improved due to the scaling of the ROS of the spectrum.

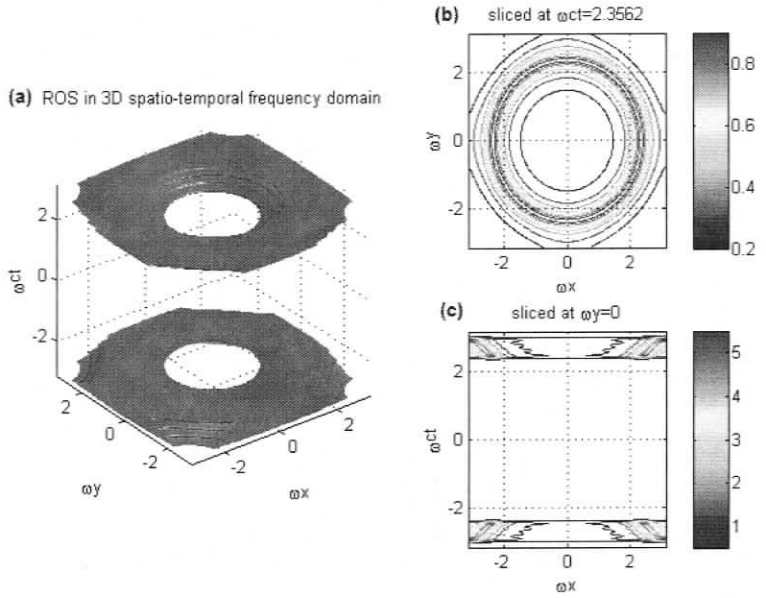

Figure 6-17. 3D spatio-temporal frequency domain representation of emulated NB (1.25-1.55GHz) MC ST signal emanating from the middle element propagating at the speed of light c with an attenuation constant of $a = 2.53$ ($\sigma = 2dB$, $r_0 = T_s = 0.0909m$) (a) the 3D ROS that contains 90% of the signal energy (b) a 2D contour plot sliced at $\omega_{ct} = 2.3562$ (c) a 2D contour plot sliced at $\omega_y = 0$

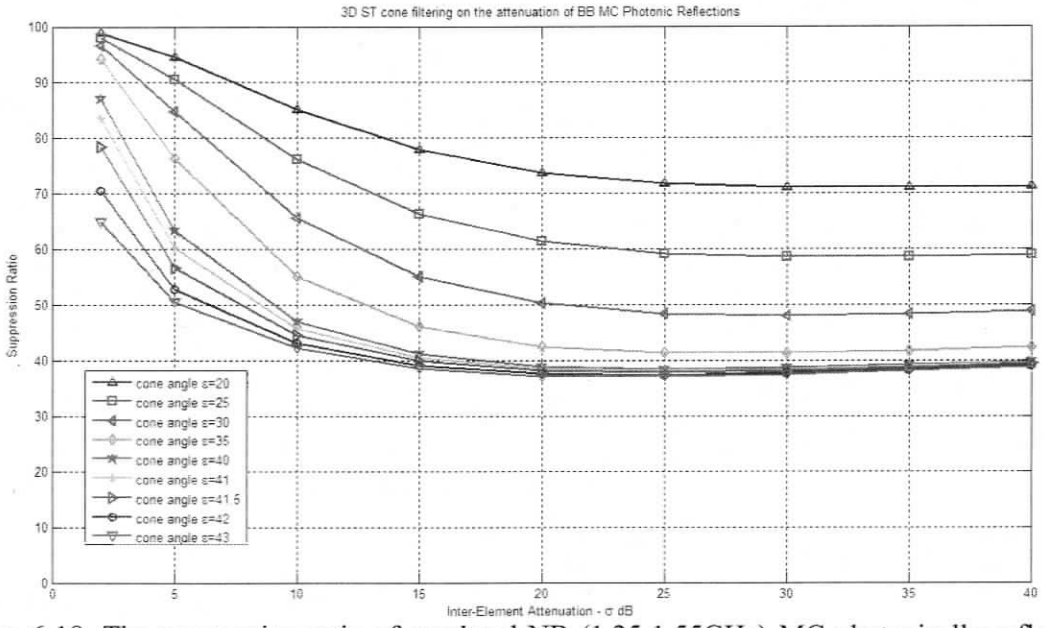

Figure 6-18. The suppression ratio of emulated NB (1.25-1.55GHz) MC photonically reflected signals propagating at a speed of c with spatial attenuations a = [2.53 6.33 12.66 18.99 25.33 31.66 37.99 44.32 50.66] (σ = [2 5 10 15 20 25 30 35 40]dB, $r_0 = T_s = 0.0909m$), filtered by 3D ST cone filters of passband angles ε = [20 25 30 35 40 41 41.5 42 43]

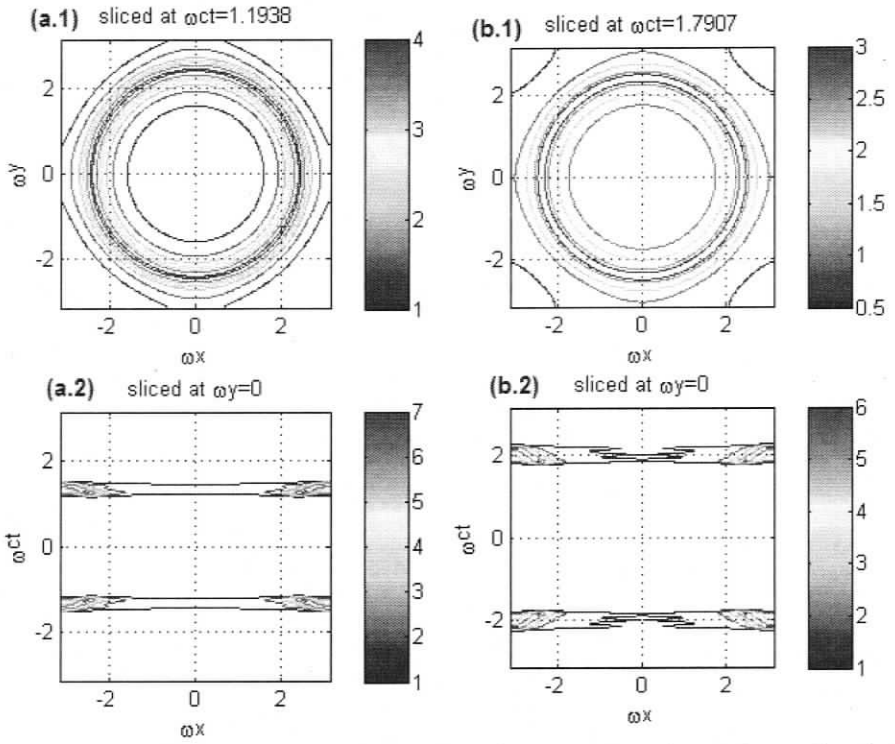

Figure 6-19. 3D spatio-temporal frequency domain representation of emulated NB (1.25-1.55GHz) MC ST signal emanating from the middle element propagating at a speed of $3c/4$ with an attenuation constant of $a = 2.53$ ($\sigma = 2dB$, $r_0 = T_s = 0.0909m$) (b) a 2D contour plot sliced at $\omega_{ct} = 1.7907$ (c) a 2D contour plot sliced at $\omega_y = 0$

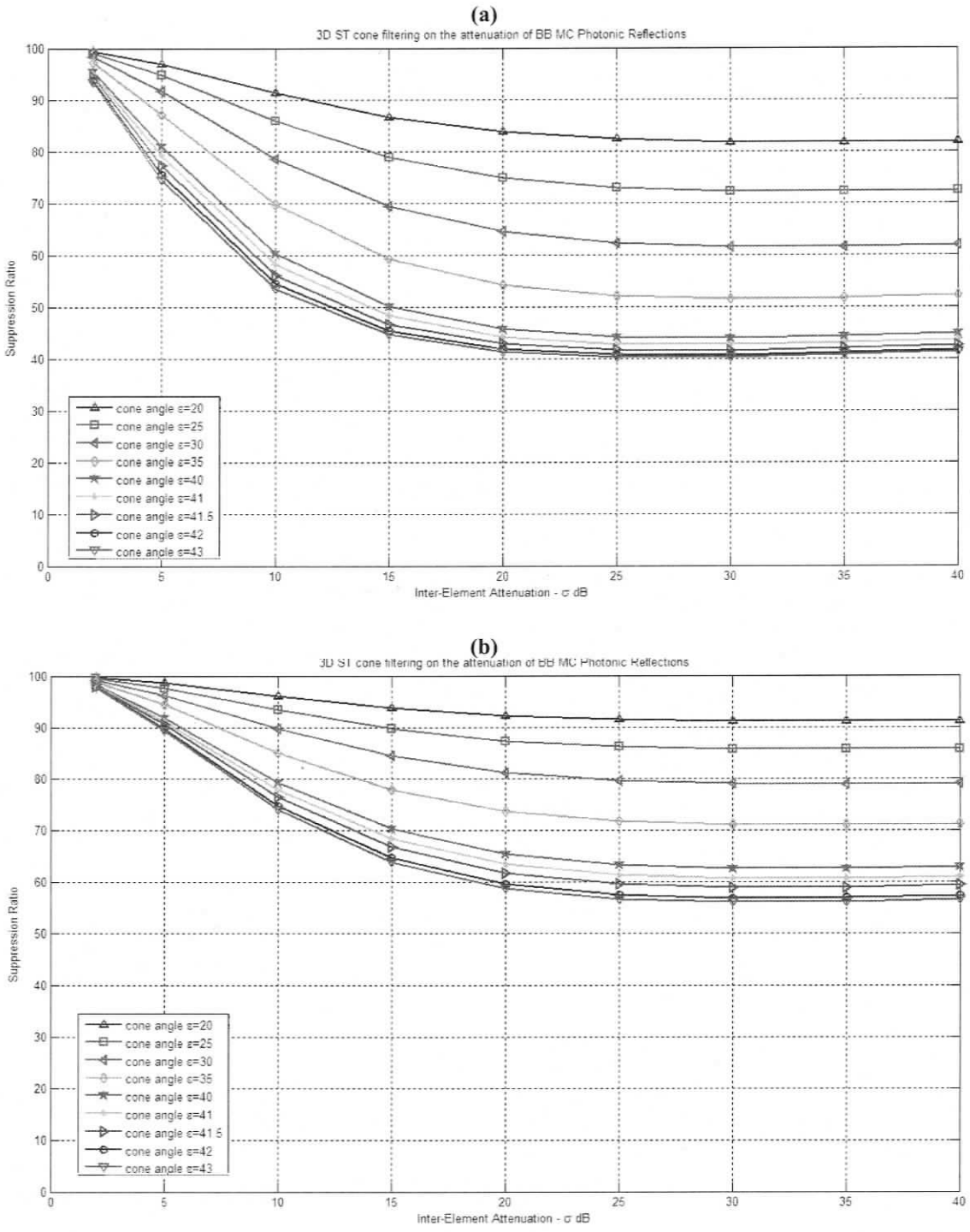

Figure 6-20. The suppression ratio of emulated NB (1.25-1.55GHz) MC photonically reflected signals propagating at a speed of (a) $3c/4$ and (b) $c/2$:- for spatial attenuations a = [2.53 6.33 12.66 18.99 25.33 31.66 37.99 44.32 50.66] (σ = [2 5 10 15 20 25 30 35 40]dB, $r_0 = T_s = 0.0909m$), filtered by 3D ST cone filters of passband angles ε = [20 25 30 35 40 41 41.5 42 43]

6.7 Summary

In this Chapter, the cone filter bank proposed in Chapter-5 is used to process synthesised BB RFI, BB SOI and BB MC signals. First, the mitigation of over-the-horizon BB RFI signals are numerically analysed by employing the proposed ST cone filter. The results confirmed significant attenuation of BB RFI at lower cone passband angles. At higher passband angles the respective suppression efficiency is decreased due to the spatial smearing of the BB RFI signal caused by the finite aperture effect of the antenna array.

Secondly, the mitigation of BB MC signals are analysed at various passband cone-angles. For both photonically reflected signals and LNA noise, suppression ratio is observed to be high at lower cone-angles and lower inter-antenna attenuations. At higher attenuations the spatial smearing resulted in a decrease in the suppression efficiency.

Next, the performance of the proposed cone filter for filtering of BB SOI in the presence of BB RFI and BB MC signals is illustrated using 3D and 2D space-time and spatio-temporal simulation figures. The figures illustrated the capability of the ST approach to successfully filter BB SOI by suppressing BB RFI and BB MC signals.

Then, the performance of the proposed cone filter in filtering out the BB SOI and suppressing BB RFIs and BB MC signals is evaluated using simulated BB ST signals. This is done for both AA and FPA cases. When the energy of the BB RFIs and BB MC signals are equal, the results showed higher SIR improvement in comparison to the case where MC LNA signal energy is dominant. When the MC LNA noise energy is dominant a minimum of 2dB improvement of SIR was observed.

Finally, some additional results are presented for emulated MC coupled signals to investigate the suppression performance at lower propagation speeds. The analysis is performed for two operational bands i.e for broadband and narrow band, and the results indicate an improvement in the suppression performance at lower propagation speeds due to the scaling of the ROS of the MC spectrum along the temporal frequency axis.

Chapter 7

Conclusions and Future work

7.1 Conclusions

A 3D ST filtering approach is proposed to enhance BB SOIs by attenuating over-the-horizon BB RFI and BB MC signals for use in the next generation radio astronomical applications. For this purpose, a novel 3D linear phase filter bank structure consisting of 1D FIR filters and 2D circularly symmetric FIR filters is introduced.

In Chapter-3 it is shown that for AA and FPA applications there exist over-the-horizon BB RFI signals that have ROSs outside the ROS of the SOIs in the 3D frequency domain. These BB RFIs have a DOA which is on or close to the horizon and their ROSs in the 3D frequency domain lie mostly on or within the spectral light cone. The ST PW model used for the RFI signals which are incident on FPAs is similar to that of AAs, however, the modeling of SOIs on the FPAs is not straightforward. It requires the calculation of the field distribution on the FPA. The functional form of the field distribution on the FPA is derived using the far-field distribution of the parabolic antenna. To accurately approximate the field distribution on the FPA, the far-field functional form is adjusted using field distribution data obtained from UC-FPFC [40]. Based on their analysis it is reviewed that the ROS of BB SOI on FPAs in the 3D frequency domain may form a solid cone in contrast to a line spectrum in the case of AAs. The separability of these signals may be affected due to the violation of the Nyquist sampling condition, and/or the finite aperture effect of the array. Assuming that the Nyquist condition is satisfied and a sufficiently large aperture size is chosen, an ST filter that completely encloses the ROS of the SOI in its passband and the spectral light cone in its stopband can be successfully employed to mitigate over-the-horizon BB RFI signals.

In Chapter-4, the ST propagation of MC signals on a BB array is modeled using a circularly symmetric function that decays exponentially in the spatial domain. It is shown, that there is convincing evidence to use such a simple model to approximate MC

signal propagation on a BB Vivaldi array, based on the analysis of scattering parameter data measured from the 180-element Vivaldi antenna array of DRAO, Canada. For this array, a spatial inter-antenna attenuation of approximately between 15-20dB is observed. Two possible MC signal categories, namely photonically reflected incident waves and internally generated LNA noise waves are considered. The analysis is carried out on the emanation from the middle element without loss of generality. The analysis indicates that, at lower spatial attenuations, BB MC signals have their ROS of the spectrum confined to and around the spectral light cone in the 3D spatio-temporal frequency domain. At higher spatial attenuations (such as inter-antenna attenuation of 15dB corresponding to the analysed Vivaldi array) the ROS of BB MC signals are smeared along the spatial frequency plane, in the complete Nyquist cube.

In Chapter-5, a novel cone filter bank structure consisting of 1-D FIR filters and 2-D circularly symmetric FIR filters is introduced. In radio astronomy applications it is required that the ST filtering preserve the phase information of the SOIs due to the subsequent beamforming/correlation operations. Further, it is required that SOIs undergo minimal distortion by the cone filter while providing maximum immunity RFI and MC signals. Thus, the 3D cone filter must have a linear phase transfer function and a circular cross section to enclose the ROSs of the SOIs in FPAs/AAs. Previously reported analytic cone filters [4][5][7][22] fall short in these aspects and, therefore, a novel analytic 3D linear phase filter bank structure is proposed.

The mitigation of over-the-horizon BB RFI signals are numerically analysed by employing the proposed ST cone filter bank on synthesised BB RFI signals, in Chapter-6. The results confirmed significant attenuation of BB RFI at lower cone passband angles. At higher passband angles, the spatial smearing of the BB RFI signal caused by the finite aperture effect of the antenna array reduces the suppression efficiency. The suppression of BB MC signals is analysed at various passband cone angles. For both photonically reflected signals and LNA noise, the suppression ratio is observed to be high at lower cone-angles, lower propagation speeds and lower inter-antenna attenuations. At higher attenuations the spatial smearing resulted in a decrease in the suppression efficiency.

The performance of the proposed cone filter in filtering out the BB SOI by attenuating BB RFIs and BB MC signals, is evaluated using simulated (synthesised) BB ST signals.

This is done for both the AA and FPA cases at two possible scenarios; one with strong BB RFI conditions, and the other with dominant LNA noise conditions where BB RFI is weaker. When the energy of BB RFI signals is considerable, the results show higher SIR improvement in comparison to the scenario with dominant MC LNA noise energy. When MC LNA noise energy is dominant, a minimum of 2dB improvement of SIR is observed.

7.2 Future Work

Satisfactory evidence is shown in Chapter-4, sub-section 4.3, that the simplistic circularly symmetric propagation model is adequate to approximate the propagation of MC signals of certain frequency bands on the 180-element Vivaldi array, DRAO. However, further experimental data obtained from several dense arrays are required in order to accurately approximate the general ST behaviour of MC signals on dense arrays. A possible extension of the modeling is to analyse time series data obtained from a dense Vivaldi array when the middle Vivaldi is in the transmission mode. Such analysis may lead to a close approximation of the actual ST behaviour of MC signals.

Further, it has been assumed that the synthesised BB signal models (such as the SOIs, RFIs and MC signals) undergo A/D (temporal sampling) at the RF level, whereas in actual implementation of AAs/FPAs the A/D operation occurs after the temporal downconversion process (at an intermediate frequency - IF). As a result, the representation of the temporally downconverted signals in the 3D frequency domain is subjected to a downshift along the temporal frequency axis towards the origin. Consequently, the required passband shape of the 3D ST filter may no longer be a cone, but instead may become a truncated cone (frustum) [55]. Furthermore, due to spatial limitations, in certain AAs/FPAs implementations the spatial Nyquist condition may not be satisfied at or close to the maximum frequency. Therefore, under the above mentioned circumstances, a thorough analysis of the signals in the 3D frequency domain is required. Based on the analysis it is possible to find a suitable passband shape of the 3D ST filter corresponding to a given AA/FPA configuration.

The proposed analytic 3D filter bank structure can be used to approximate any passband shapes consisting of circularly symmetric cross-sections. Further, the width of

the sub-bands on the temporal-frequency axis can also be adjusted such that the filter passband achieves higher selectivity close to the origin. It is also possible to introduce a polyphase structure to the proposed filter bank in order to considerably reduce the computation complexity.

Bibliography

[1] D. E. Dudgeon and R. M. Mersereau., *Multideimensional Signal Processing.* N.J : Prentice-Hall Inc, 1984.

[2] L. T. Bruton., Enel 699 Course Notes. [Online] University of Calgary, 2001. URL: http://www-mddsp.enel.ucalgary.ca/People/bruton/Enel699Main.html

[3] L. T. Bruton and N. R. Bartley., "Three-dimensional image processing using the concept of network resonance." IEEE Transactions, Circuit and Systems, July 1985, Issue no-7 pp.664-672, Vols. CAS-32.

[4] L. T. Bruton., "Selective filtering of spatio-temporal plane waves using 3D cone filter banks." Communications, Computers and signal Processing, IEEE Pacific Rim Conference, 26-28 Aug. 2001, Vol. 1. Pages 67-70.

[5] L. T. Bruton., "Three-dimensional cone filter banks." Circuits and Systems I: Fundamental Theory and Applications, IEEE Transactions, Feb. 2003, Issue 2, Vol. 50. pp 208-216.

[6] L.T. Bruton., "A 3D polyphase-DFT cone filter bank for broad band plane wave filtering." Circuits and Systems, ISCAS 2004, 23-26 May 2004. Page(s):III - 181-4 Vol.3.

[7] L.T. Bruton and S. Singh., "Plane wave filtering using a novel 3D cone-stop filter bank." The 45th Midwest Symposium on, Vol. 3 : Circuits and Systems, 2002. MWSCAS-2002, Aug. 4-7, 2002. pp676–679.

[8] B. Kuenzle and L.T. Bruton., "3-D IIR filtering using decimated DFT-polyphase filter bank structures." Circuits and Systems I: Fundamental Theory and Applications, IEEE Transactions, Feb. 2006, Issue 2, Vol. 53. pp 394 - 408.

[9] Sneezana Stanimirovic (Editor),., *Single-Dish Radio Astronomy: Techniques and Applications.* Arecibo Observatory, Astronomical Society of the Pacific : NAIC-NRAO Summer School Held at National Astronomy and Ionosphere Center, December 2002.

[10] Peter J. Hall, (Ed.)., *The Square Kilometre Array An Engineering Perspective.* Springer, 2004. Vol. 17/1-3.

[11] [et al..]., "SKA Documents." *Memos.* [Online] [Cited: May 20, 2009.] http://www.skatelescope.org/pages/documents_3.htm.

[12] S. W. Ellingson and G. A. Hampson., "Mitigation of radar interference in L-band radio astronomy." Astrophy.J.Suppl., 2003. Vol.147, 167-176

[13] J. Raza, A.J. Boonstra, & A.J.van der Veen., "Spatial filtering of RF interference in radio astronomy." IEEE Signal Processing Letter, 2002, Issue 2, Vol. 9. 64--67.

[14] A. Leshem, A.-J. van der Veen, and A. Boonstra., "Multichannel interference mitigation techniques in radio astronomy." Astrophys. J. Suppl, 2000, Issue 1, Vol. 131. pp. 355–374.

[15] B. D. Van Veen & K. M. Buckley., "Beamforming: A versatile approach to spatial filtering." IEEE Acoust., Speech, & Signal Processing Magazine, April 1988.

[16] B. D.Jeffs, L. Li & K. F.Warnick., "auxilliary antenna-assisted interference mitigation for radio astronomy arrays." IEEE Trans. Signal Processing, Issue 2, Vol. 53. 439.

[17] F. Briggs, J. Bell, and J. Kesteven., "Removing radio interference from contaminated astronomical spectra using an independent reference signal and closure relations." Astronom. J., Aug. 2000., Vol. 120. pp.3351–3361.

[18] D. F. Kelley and W. L. Stutzman., "Array antenna pattern modeling methods that include mutual coupling effects." IEEE Trans. Antennas Propag, Dec 1993, Issue 12, Vol. 41. pp. 1625–1632.

[19] J. P Weem, and Z Popovic., "A method for determining noise coupling in a phased array antenna." IEEE MTT-S International Microwave Symposium Digest, 2001. 271-274.

[20] C. Craeye., B. Parvais, and X. Dardenne., "MoM simulation of signal-to-noise patterns in infinite and finite receiving antenna arrays." IEEE Trans. Antennas and Propag, 2004, Issue 12, Vol. 52. pp 3245-3256.

[21] J. W. Wallace and M. A. Jensen., "Mutual coupling in MIMO wireless systems: A rigorous network theory analysis." IEEE Trans. Wireless Commun, Jul 2004, Issue 4, Vol. 3. pp. 1317–1325.

[22] L. Khademi., *Reducing the computational complexicities of FIR 2D fan and 3D cone filters.* University of Calgary : M.S.Thesis, Department of Electrical and Computer Engineering, 2004.

[23] J. R. Fisher and R. F. Bradley., "Full sampling array feeds for radio telescopes." SPIE, Radio Telescopes, 2000, pp. V-4015.

[24] S. G. Hay, J. D. O'Sullivan, J. S. Kot, C. Granet, A. Grancea, A. R. Forsyth, and D. H. Hayman., "Focal plane array development for ASKAP (Australian SKA pathfinder)." European conference on antennas and propagation, Eu-CAP, Edinburgh, UK, Nov-2007.

[25] Brian D. Jeffs, Karl F. Warnick, Jonathan Landon, Michael Elmer, J. Richard Fisher and Roger Norrod., "Recent progress with the BYU/NRAO." Socorro New Mexico : CALIM 2009, March 30 – April 3, 2009 .

[26] R. Maaskant, M. V. Ivashina, R. Mittra, W. Yu, and N.-T. Huang., "Parallel FDTD modeling of a focal plane array with vivaldi elements on the highly parallel LOFAR BlueGene/L supercomputer." IEEE Antennas Propag. Society International Symposium, June 2006, pp. pp. 3861–3864. 2.

[27] B. Veidt and P. Dewdney., "A phased-array feed demonstrator for radio telescopes." URSI General Assembly, URSI-GA, 2005.

[28] Tony Willis., "Simulations of Synthesis Telescope Antennas Equipped with Focal Plane Arrays." CALIM 09, Socorro, New Mexico, March 30 – April 3, 2009.

[29] P.D. Patel, D.W. Kant, E. Wal and A. van Ardene., "Phased array antennas demonstrator as a radio telescope - EMBRACE." Antennas and Propagation Society International Symposium, 2008. AP-S 2008. IEEE, 5-11 July 2008. Page(s):1 - 4.

[30] G. H. Hampson and J. G..Bij de Vaate., "Verification of THEA tile calibration and beamforming results using a near field scanner." London, UK : IEEE European Microwave Conference, Sept. 2001, Vol. Vol. 3. pp 141-144.

[31] Bunton J.D., *FX Correlators for the SKA.* The SKA: Defining the Future, Berkerly Workshop, July 2001.

[32] Peter J Hall., *SKA – The Australian Perspective.* Jodrell Bank : Technology Pathways to the Square Kilometer Array: SKA Workshop Presentations, 3rd -5th August 2000.

[33] Bruce MacA Thomas., *The strategy for establishing one or more radio-quiet reserves in Western Australia.* Jodrell Bank : SKA Workshop Presentations, 3rd -5th August 2000.

[34] C. A. Balanis., *Antenna Theory: Analysis and Design.* John Wiley and sons, 2005. 3rd Edition.

[35] Karl F. Warnick and Brian D. Jeffs., "Efficiencies and system temperature for a beamforming array." IEEE Antennas and Wireless Propagation Letters, 2008, Vol. 7. pp 565 - 568.

[36] Jacob W.M. Baars., *The Paraboloidal Reflector Antenna in Radio Astronomy and Communication.* Springer New York, 2007.

[37] Craig Scott., *Modern Methods of Reflector Antenna Analysis and Design.* Boston-London : Artech House, 1990.

[38] Walter Brisken and Christophe Craeye., *Focal Plane Array Beam-Forming and Spill-Over Cancellation Using Vivaldi Antennas.* EVLA, January 29, 2004. MEMO 69.

[39] A. W. RUDGE., "Focal-plane field distribution of parabolic reflectors." Electronics Letters, IEEE, 16 Oct 1965, Issue 21, Vol. 5.

[40] T.K.Gunaratne and L.T. Bruton., *UC-FPFC: A MATLAB Program to Evaluate the Electric Field on the Observation Plane of a Prime Focus Paraboloidal Reflector.* University of Calgary : Internal Report, 2008.

[41] K. F. Warnick and M. A. Jensen., "Effect of mutual coupling on interference mitigation with a focal plane array." IEEE Trans. Antennas Propag, Aug 2005, Issue 8, Vol. 53. pp. 2490–2498.

[42] S.Stein., "On cross Coupling in Multiple-Beam Antennas." IRE, Trans. Antennas Propag, Sep 1962, Issue 5, Vol. 10. pp 548-557.

[43] G. Bekefi and A. H. Barrett., *Electromagnetic Vibrations, Waves, and Radiation.* Cambridge : MA:- MIT Press, 1987.

[44] K.Rohlfs, T.L. Wilson., *Tools of Radio Astronomy.* New York : Springer, 1999.

[45] Henrik Holter, Tan-Huat Chio, and Daniel H. Schaubert., "Experimental results of 144-element dual-polarized endfire tapered-slot phased arrays." IEEE Trans. Antennas and Propag, Nov-2000, Issue 11, Vol. 48. pp 1707-1718.

[46] Rick Smegal., *DRAO Test Report: PHAD 180 Element Array: Terminal Port Scattering Observations.* Victoria, BC Canada : Aardvark Resources, March 27, 2008. Document No. HIAAMR05D01, Chapters 1,2 and 3, Rev. 0.0.

[47] —. *DRAO PHAD 180 Element Array Test Data File: a180Spara_v100.mat.* Victoria, BC, Canada : Aardvark Resources, 2008. S-Parameter Data: CD-2.

[48] L. Bruton and N. Bartly., "Highly selective three-dimensional recursive beam filters using intersecting resonant planes." Circuit and Systems, IEEE Transactions, Mar 1983, Issue 3, Vol. 30. pp 190-193.

[49] V. Rajaravivarma, P. K. Rajan and H. C. Reddy., "Application of symmetry results in 3-D digital filter design." Proc. of the 21st Southeastern Symposium on System Theory, 1989. pp. 277–281.

[50] G. Runze and P. Steffen., "A contribution to the design of three-dimensional digital FIR and IIR cone-filters." Proc. of 3D Image Analysis and Synthesis`96, 1996. pp. 179-182,.

[51] M. Bolle., "A closed form design method for recursive 3-d cone filters." IEEE ICASSP-94 : Acoustics, Speech, and Signal Processing, 19-22 Apr 1994. VI/141-VI/144.

[52] P. Agathoklis and L. T. Bruton., "Practical-BIBO stability of n-dimensional." Proc. IEE, 1983. vol. 130, no. 6 pp. 1404-1414.

[53] L. Khademi and L.T. Bruton., "Reducing the computational complexity of narrowband 2D fan filters using shaped 2D window functions." Circuits and Systems, ISCAS 2003, 25-28 May 2003. Vol. 3. 702-705.

[54] A. Leshem, A.-J. van der Veen, and E. Deprettere., "Detection and blanking of GSM interference in radio-astronomical observations." Second IEEE Workshop Signal Process. Adv. Wireless Commun, 1999. pp. 374–377.

[55] Gunaratne, T.K. and Bruton, L.T., "Beamforming of broad-band bandpass plane waves using polyphase 2-D FIR trapezoidal filters." Circuits and Systems I: Regular Papers, IEEE Transactions on, April 2008, Issue 3, Vol. 55. PP 838-850.

[56] Bruce Veidt., *Data files and reference documents circulated through e-mails.* Penticton : DRAO, Canada, 2009. Private Communications.

Appendix A

a) A Brief Overview of the Classical Beamforming Method [16][25][56]

The classical beamforming method is a spatial beamforming technique which is used for narrowband beamforming applications. In the beamforming operation on a phased array of N-elements, the received signal voltage vector v is phase shifted and/or scaled and the resulting voltages are summed to produce the single beamformed output voltage y represented as,

$$y = w^H v \tag{A.1}$$

where w^H represents complex transpose-conjugate beamformer coefficient vector. The voltage vector v is typically composed of various signal components as,

$$v = v_{SOI} + v_{sky} + v_{RFI} + v_{MC} + v_{rec} \tag{A.2}$$

where v_{SOI} is the voltage due to the signal of interest (SOI), v_{RFI} is the voltage due to radio frequency interference (RFIs) , v_{rec} is the voltage due to additive LNA noise and thermal noise caused by the ohmic resistance of the antennas/propagation path, and v_{MC} is the noise voltage caused by the mutual coupling of LNA noise and photonically reflected incident waves. A typical figure of merit of a beamforming operation is the signal to interference ratio (SNR) of the phased array defined as,

$$SNR = \frac{available\ signal\ power}{available\ noise\ power} = \frac{P_{SOI,av}}{P_{INT,av}} \tag{A.3}$$

where $P_{(.),av}$ denote available power from the signal/s $(.)$. As opposed to a single antenna, the calculation of available power P_{av} using beamformer coefficients is not straight forward since multiple output voltages may exist across a single load. Hence, the available power, P_{av} is approximated using thn the form of ,

$$P_{av} = \alpha . P_{actual} = \frac{E[yy^*]}{2R_L}$$

$$= \frac{w^H \mathbf{R}_v w}{2R_L} \tag{A.4}$$

where E[·] denotes expectation, $\mathbf{R}_v$ is the correlation matrix (or covariance matrix) of voltage vector v and the proportionality constant α can be determined by setting the available power due to a spatially isotropic noise environment when the antenna is in equilibrium with its environment. Using (A.4) and (A.3) the SNR can be re-written as,

$$SNR = \frac{available\ \ signal\ \ power}{available\ \ noise\ \ power} = \frac{P_{SOI,av}}{P_{INT,av}} = \frac{w^H \mathbf{R}_{SOI} w}{w^H \mathbf{R}_{noise} w} \tag{A.5}$$

where $\mathbf{R}_{SOI}$ is the signal-of-interest correlation matrix and $\mathbf{R}_{INT}$ is the total interference correlation matrix, which are derived as,

$$\begin{aligned} \mathbf{R}_v &= E[vv^H] \\ &= E[v_{SOI} {v_{SOI}}^H] + E[v_{sky} {v_{sky}}^H] + E[v_{RFI} {v_{RFI}}^H] + E[v_{rec} {v_{rec}}^H] + E[v_{MC} {v_{MC}}^H] \\ &= \mathbf{R}_{SOI} + \mathbf{R}_{sky} + \mathbf{R}_{RFI} + \mathbf{R}_{rec} + \mathbf{R}_{MC} \\ &= \mathbf{R}_{SOI} + \mathbf{R}_{noise} \end{aligned} \tag{A.6}$$

Therefore, the optimum beamformer coefficients w_{opt} that maximises SIR in can be represented as,

$$w_{opt} = \arg\max_{w} \frac{w^H \mathbf{R}_{SOI} w}{w^H \mathbf{R}_{noise} w} \tag{A.7}$$

which then can be transformed in to the form of a generalised eigenvalue problem given by,

$$\mathbf{R}_{SOI} w_{opt} = \lambda_{\max} \mathbf{R}_{noise} w_{opt} \tag{A.8}$$

where w_{opt} is the dominant eigenvector and $\lambda_{\max}$ is the largest eigenvalue of $\mathbf{R}_{SOI}$. In practical applications, the signal correlation matrix $\mathbf{R}_{SOI}$ is not available; therefore a pre-calibration process is required. Using the calibration data, the $\mathbf{R}_{SOI}$ can be approximated as $\mathbf{R}_{on}$ is the signal correlation when the array is pointed towards the calibration source of a desired direction and $\mathbf{R}_{off}$ is calculated when the array is pointing off the source (to the blank sky) assuming that $\mathbf{R}_{off} \approx \mathbf{R}_{noise}$. Experimental results of the classical beamforming operation applied on PHAD, DRAO, Canada is discussed next.

b) Experimental Results of Classical Beamforming on PHAD (Phased Array Demonstrator) DRAO, Canada

The setup of the PHAD environment is summarised in Table A-1 [56]. The calibration source is capable of transmitting horizontally or vertically polarized carrier in the L-band. The trajectory of the calibration source is placed above the array in the direction of x-axis (along horizontal Vivaldis). The resulting time-series data extracted from calibration processes have been recorded to binary files by the PHAD receiver system. Octave[7], Matlab and Python[8] are used to reformat these data files to apply the classical bemaformer method.

Table A-1 : Parameters of the experimental PHAD setup

Signal of interest	Unmodulated L band carrier
Polarization	H and V
(1.2GHz, H) , (1.2GHz, V), (1.4GHz, V), (1.8GHz, H) , (1.8GHz, V)	
Antenna Array	6x7x2 = 84 elements
Antenna Type	Viva-45° to +45° resolution of 5°
Scan trajectory	Along the plane through the centre horizontal-array (x axis)
Baseband	4MHz
Sampling rate	10Msamples/s

[7] Octave is a high-level language for numerical computations; an open-source alternative for Matlab

[8] Python is a dynamic object-oriented programming language which offers strong support for integration among languages.

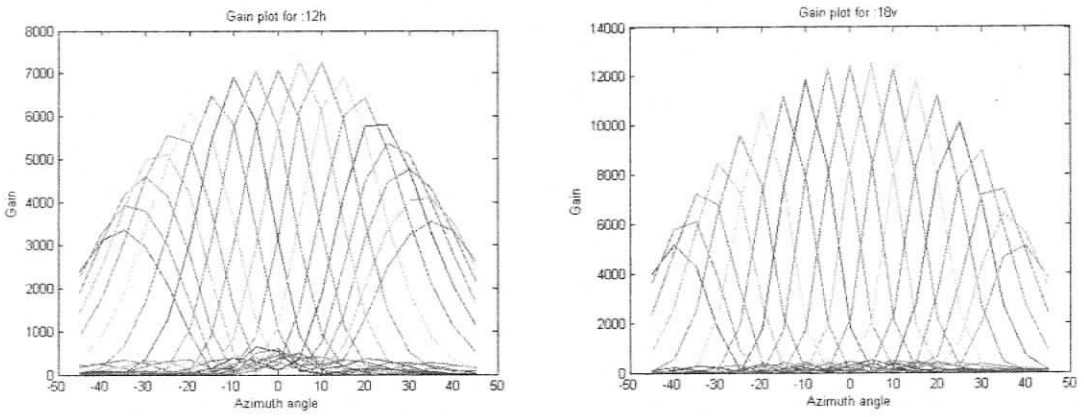

Figure A-1. Overlaid beam plots corresponding to beamformer coefficients derived at (a) horizontal polarised 1.2GHz data (b) vertically polarised 1.8GHz data

The overlaid beam plots corresponding to horizontally polarised 1.2GHz and vertically polarised 1.8GHz, of the classical beamforming method is shown in Fig.A-1.